

## INFORMATION TO USERS

This manuscript has been reproduced from the microfilm master. UMI films the text directly from the original or copy submitted. Thus, some thesis and dissertation copies are in typewriter face, while others may be from any type of computer printer.

**The quality of this reproduction is dependent upon the quality of the copy submitted.** Broken or indistinct print, colored or poor quality illustrations and photographs, print bleedthrough, substandard margins, and improper alignment can adversely affect reproduction.

In the unlikely event that the author did not send UMI a complete manuscript and there are missing pages, these will be noted. Also, if unauthorized copyright material had to be removed, a note will indicate the deletion.

Oversize materials (e.g., maps, drawings, charts) are reproduced by sectioning the original, beginning at the upper left-hand corner and continuing from left to right in equal sections with small overlaps. Each original is also photographed in one exposure and is included in reduced form at the back of the book.

Photographs included in the original manuscript have been reproduced xerographically in this copy. Higher quality 6" x 9" black and white photographic prints are available for any photographs or illustrations appearing in this copy for an additional charge. Contact UMI directly to order.

# UMI

A Bell & Howell Information Company  
300 North Zeeb Road, Ann Arbor MI 48106-1346 USA  
313/761-4700 800/521-0600



**A STUDY OF ITERATIVE METHODS  
ON FORWARD AND INVERSE SCATTERING PROBLEMS**

**BY**

**JIUN-HWA LIN**

**B.S.Eng., National Taiwan University, 1985**

**M.S., National Taiwan University, 1989**

**THESIS**

**Submitted in partial fulfillment of the requirements  
for the degree of Doctor of Philosophy in Electrical Engineering  
in the Graduate College of the  
University of Illinois at Urbana-Champaign, 1995**

**Urbana, Illinois**

**UMI Number: 9624418**

---

**UMI Microform 9624418**  
**Copyright 1996, by UMI Company. All rights reserved.**

**This microform edition is protected against unauthorized  
copying under Title 17, United States Code.**

---

**UMI**  
**300 North Zeeb Road**  
**Ann Arbor, MI 48103**

UNIVERSITY OF ILLINOIS AT URBANA-CHAMPAIGN

THE GRADUATE COLLEGE

SEPTEMBER 1995

WE HEREBY RECOMMEND THAT THE THESIS BY

JIUN-HWA LIN

ENTITLED A STUDY OF ITERATIVE METHODS

ON FORWARD AND INVERSE SCATTERING PROBLEMS

BE ACCEPTED IN PARTIAL FULFILLMENT OF THE REQUIREMENTS FOR

THE DEGREE OF DOCTOR OF PHILOSOPHY

*W. c. Chew*

Director of Thesis Research

*P. M. Kong*

Head of Department

Committee on Final Examination†

*W. c. Chew*

Chairperson

*W. O'Brien*

*Jia Jia Jin*

*John B...*

† Required for doctor's degree but not for master's.

# A STUDY OF ITERATIVE METHODS ON FORWARD AND INVERSE SCATTERING PROBLEMS

Jiun-Hwa Lin, Ph.D.  
Department of Electrical and Computer Engineering  
University of Illinois at Urbana-Champaign, 1995  
Weng C. Chew, Advisor

Iterative methods are suitable for solving large-size problems in the electromagnetic and acoustic wave scattering. Both the conjugate gradient and bi-conjugate gradient methods combined with the fast Fourier transform (CGFFT and BiCGFFT) are employed as efficient solvers in forward and inverse scattering problems for penetrable bodies.

In microwave imaging, material permittivity is the parameter to retrieve. The distorted Born iterative method (DBIM), a nonlinear inverse scattering algorithm that accounts for multiple scattering, can retrieve the permittivity of high contrast. The computational cost for each iteration is  $O(N^{1.5} \log N)$  as the number of transmitters is  $O(N^{0.5})$ , where  $N$  is the number of cells. Real experimental data has been processed by the algorithm under a full-view system to obtain images in real and imaginary parts of permittivity. With the aid of the frequency-hopping scheme, large-size objects can be reconstructed with higher fidelity.

The nested equivalence principle algorithm (NEPAL) has been developed to implement the matrix-vector multiply in an  $O(N \log N)$  fashion. NEPAL can also be applied in the cases of nonuniform grids. With the fast multipole method (FMM) incorporated in NEPAL, an  $O(N)$  algorithm can be achieved to perform the matrix-vector multiply often occurring in the iterative methods.

The T-matrix method is used to formulate the three-dimensional electromagnetic scattering problems. Exploiting the Toeplitz structure of the translation matrix, BiCGFFT is invoked as the solver, which requires only  $O(N \log N)$  operations

at each iteration and  $O(N)$  memory storage. Efficiency in computation and storage enables the algorithm to solve large problems in real practice.

Acoustic wave equations possess the same features as the electromagnetic wave equations for  $H_z$  polarization in two dimensions. The local shape function method (LSF) developed for inverse electromagnetic scattering is adapted to reconstructing both the density and compressibility of soft tissues in ultrasonic imaging, which is valuable in clinical diagnosis. CGFFT is utilized as the forward solver as required to implement inverse operators. The capability of the algorithm has been demonstrated in the reconstructions from the experimental data as well as the synthetic data, and its complexity can be  $O(N^{1.5} \log N)$  at each iteration. A multiple-frequency scheme, such as the frequency-hopping method, provides better reconstruction than a single-frequency scheme.

## ACKNOWLEDGEMENTS

I wish to express my deepest gratitude to Professor Weng Cho Chew, my thesis advisor, for his insightful guidance throughout the course of development of this dissertation, for his support and encouragement, and for his resourceful knowledge inspiring my interest in electromagnetics.

I would like to thank the members of my doctoral committee, Professors Y. Bresler, J. M. Jin and W. D. O'Brien, for numerous helpful discussions and suggestions.

During the years of my graduate work, all of my colleagues, past and present, in the Electromagnetics Laboratory have been very helpful in so many aspects that I would like to thank Caicheng Lu, Hong Gan, Rob Wagner, Jiming Song, Yi-Ming Wang and Greg Otto for their valuable technical discussions; Muhammad Nasir, Bill Weedon, Guy Klemens and Yong-Hua Chen for their generous computer assistance; and Fu-Chiang Chen, Kaladhar Radhakrishnan, Jin Seob Kang, Mahta Moghaddam, Levent Gürel, Xuguang Yang, James Bowen and Toshiyuki Tanaka for their wonderful friendship. Thanks are expressed particularly to Greg Otto and ThermoTrex Corporation in San Diego, who generously provided their ultrasonic measurement data. Thanks also go to Yanhua Pan for her administrative assistance.

I am truly grateful to my wife, Shuhua, for her continued support, for her undying patience and love. I deeply thank her for leaving her job in Taiwan and coming to the States to take care of me.

I am deeply indebted to my parents for all they have done for me. It would have been impossible to finish my studies without their unconditional support, their faith in me, and their motivation. I thank them both. My sincere gratitude also goes to my brothers for their encouragement and inspiration.

This work was supported by the Office of Naval Research under contract N00014-89-J-1286, the Army Research Office under contract DAAL03-91-G-0339, the Na-

tional Science Foundation under grant NSF ECS 92-24466, and the Research Board at the University of Illinois, Urbana-Champaign. The computer time for much of this work was provided by the National Center for Supercomputing Applications (NCSA) at the University of Illinois, Urbana-Champaign, and the San Diego Supercomputer Center (SDSC).

## **DEDICATION**

**To my parents and wife**

## TABLE OF CONTENTS

CHAPTER	PAGE
<b>1 INTRODUCTION . . . . .</b>	<b>1</b>
<b>1.1 References . . . . .</b>	<b>5</b>
<b>2 CGFFT AND BiCGFFT METHODS ON FORWARD SCATTERING . . . . .</b>	<b>6</b>
<b>2.1 Introduction . . . . .</b>	<b>6</b>
<b>2.2 Formulation and Algorithms . . . . .</b>	<b>7</b>
2.2.1 Integral equation and its Toeplitz structure . . . . .	7
2.2.2 CG and BiCG algorithms . . . . .	9
2.2.3 Matrix-vector multiply by fast Fourier transform . . . . .	10
<b>2.3 Numerical Results . . . . .</b>	<b>12</b>
2.3.1 Verification . . . . .	12
2.3.2 Comparisons of CGFFT, BiCGFFT and RATMA . . . . .	13
<b>2.4 Conclusions . . . . .</b>	<b>19</b>
<b>2.5 References . . . . .</b>	<b>21</b>
<b>3 INVERSE SCATTERING BY THE DISTORTED BORN ITERATIVE METHOD WITH CGFFT . . . . .</b>	<b>25</b>
<b>3.1 Introduction . . . . .</b>	<b>25</b>
<b>3.2 Conjugate Gradient Minimization Scheme . . . . .</b>	<b>28</b>
<b>3.3 Fréchet Operator and the         Distorted Born Iterative Method . . . . .</b>	<b>30</b>
<b>3.4 Implementation of the Algorithm . . . . .</b>	<b>30</b>

3.5	Numerical Results and Barcelona Experimental Data . . . . .	33
3.6	Frequency-Hopping Scheme . . . . .	39
3.7	Conclusions . . . . .	48
3.8	References . . . . .	48
4	<b>MATRIX-VECTOR MULTIPLY BY NESTED EQUIVALENT PRINCIPLE ALGORITHM</b> . . . . .	52
4.1	Introduction . . . . .	52
4.2	Relationship between Surface Sources and Volume Sources . . . . .	54
4.3	Algorithm Implementation and its Complexity . . . . .	57
4.4	Comparison with FFT . . . . .	67
4.5	$O(N)$ Algorithm by Fast Multipole Method . . . . .	69
4.6	Conclusions . . . . .	74
4.7	References . . . . .	75
5	<b>3D SCATTERING SOLUTIONS BY THE BICG-FFT T-MATRIX METHOD</b> . . . . .	78
5.1	Introduction . . . . .	78
5.2	T-matrix Formulation . . . . .	80
5.2.1	Scattered fields and internal fields . . . . .	80
5.2.2	Explicit expression for matrix and vector elements . . . . .	83
5.3	BiCGFFT Implementation . . . . .	88
5.4	Numerical Results . . . . .	90
5.5	Conclusions . . . . .	95
5.6	References . . . . .	97

<b>6</b>	<b>ULTRASONIC IMAGING BY LOCAL SHAPE FUNCTION WITH CGFFT . . . . .</b>	<b>100</b>
	<b>6.1 Introduction . . . . .</b>	<b>100</b>
	<b>6.2 Forward Model by T-matrix Method . . . . .</b>	<b>102</b>
	<b>6.3 Iterative Minimization Schemes . . . . .</b>	<b>107</b>
	6.3.1 Conjugate gradient minimization . . . . .	107
	6.3.2 Distorted Born iterative method . . . . .	108
	<b>6.4 Algorithm Implementation . . . . .</b>	<b>109</b>
	<b>6.5 Results . . . . .</b>	<b>111</b>
	6.5.1 Synthetic data . . . . .	111
	6.5.2 Experimental data . . . . .	118
	<b>6.6 Conclusions . . . . .</b>	<b>134</b>
	<b>6.7 References . . . . .</b>	<b>134</b>
<b>7</b>	<b>CONCLUSIONS AND FUTURE DIRECTIONS . . . . .</b>	<b>137</b>
	<b>APPENDIX A SUMMARY OF COMPUTER CODES USED . . . . .</b>	<b>140</b>
	<b>A.1 2D TM CGFFT Forward Solver . . . . .</b>	<b>140</b>
	<b>A.2 2D TM DBIM Inverse Scattering Algorithm . . . . .</b>	<b>141</b>
	<b>A.3 NEPAL . . . . .</b>	<b>143</b>
	<b>A.4 3D BiCGFFT T-Matrix Algorithm . . . . .</b>	<b>143</b>
	<b>A.5 Local Shape Function with CGFFT Algorithm . . . . .</b>	<b>145</b>
	<b>VITA . . . . .</b>	<b>148</b>

## CHAPTER 1

### INTRODUCTION

Over a century has elapsed since the inception of Maxwell's equations, and the success of these four equations in describing macroscopic electromagnetic phenomena has been remarkable. However, practical problems typically defy a simple solution due to the complications of real geometries and materials. To solve such problems, a host of analytic techniques and approximate models are available, but these methods can still give unsatisfactory results. In addition to the analysis problem, the synthesis problem also draws attention. As an example, consider the design of an antenna, which can be done by "trial and error" and "rule of thumb" approaches: the designers can repeatedly tune the parameters, measure the radiation pattern and decide whether those settings meet the requirements. This process could be time consuming and expensive. Another example is the design of the stealth bomber. To measure the radar cross section (RCS) of the plane in an anechoic chamber whenever the geometric shape or the patch material are altered would be unfeasible. Instead of the experimental approach, computational methods are becoming more attractive in these respects. High frequency methods such as the physical theory of diffraction (PTD), with the shooting and bouncing ray (SBR) method [1], can calculate the RCS of large objects efficiently. On the other hand, the synthesis problems can be cast into a minimization problem to find the optimal parameters required. Not only do computational methods provide an effective alternative to experimental approaches, they also provide more insight into the models and algorithms on which they are based. It is this motivation that calls for various methodologies to solve electromagnetic problems computationally.

Another important factor that gives rise to the thriving of computational electromagnetics is the rapid progress of computer technology. As computers become more powerful and convenient to use, computational electromagnetics plays a more

important role in many areas, such as forward and inverse scattering, wave propagation, antenna design, high-speed circuit simulation, waveguide and acoustic wave problems. In particular, equipped with computer graphics, computational electromagnetics enables workers to visualize how electromagnetic fields propagate and interact with the medium in a virtual reality fashion. As supercomputers are more accessible and more user-friendly, many computational electromagnetics applications can be implemented in real time.

There are two major formulations in computational electromagnetics: the differential equation (DE) formulation and the integral equation (IE) formulation. The former can be implemented in a more straightforward and computationally efficient way with less memory requirement due to the sparse matrix formed after discretization. But the DE formulation requires special absorbing boundary conditions (ABC) to truncate the simulation region. It is not a trivial task to devise ABCs to simulate the infinite geometry of scattering problems. Recently, the perfectly matched layer [2] (PML) method proposed by Berenger has had success as an ABC. On the other hand, an IE formulation usually gives rise to a dense matrix equation that requires more memory and is computationally intensive. However, in contrast to DE formulation, IE formulation satisfies the radiation conditions automatically. In this work, we concentrate on the IE or IE-like formulation.

There are many methods available to solve EM problems numerically. The method of moments (MoM) with Gaussian elimination is a widely used method. However, it is well known that the complexity of this method is  $O(N^3)$  and the required memory storage is  $O(N^2)$ , where  $N$  is the number of unknowns. This costly procedure imposes a severe limit on the problem size. A goal of computational electromagnetics is to pursue more efficient algorithms in terms of speed and required resources. As the problem sizes become larger and more complicated, the need for such algorithms propels researchers to find different formulations and methodologies to achieve the goals. Propelled by this trend, we place the emphasis on the iterative methods because they have the attractive features of requiring no matrix storage and computational efficiency when a small number of iterations is

needed to converge. Although for each iteration, the iterative methods still require  $O(N^2)$  operations to implement the matrix-vector multiply, we can exploit certain features of the matrix equation to achieve better efficiency.

In this thesis, both forward scattering and inverse scattering problems are explored via iterative methods. We are interested in penetrable inhomogeneous media in two or three dimensions. After acquiring an efficient forward solver, we can apply it to the inverse scattering problems to reconstruct the dielectric constants of each cell. Ultrasonic imaging problems are also considered because the acoustics wave equation has exactly the same form as the electromagnetic wave equation for two-dimensional  $H_z$  polarization.

In Chapter 2, we begin with the conjugate gradient fast Fourier transform (CGFFT) and bi-conjugate gradient fast Fourier transform (BiCGFFT) methods in two-dimensional TM scattering problems. These methods require only  $O(N \log_2 N)$  operations in each iteration. Different convergence rates are observed in lossless and lossy media. We also compare CGFFT and BiCGFFT with the recursive aggregate T-matrix algorithm (RATMA), which is an efficient forward solver for multiple incident fields.

We introduce the nonlinear inverse scattering algorithm in Chapter 3. The goal is to reconstruct the dielectric constant of an inhomogeneous medium in a two-dimensional TM polarization situation. By incorporating CGFFT in the distorted Born iterative method (DBIM), we can reconstruct high-contrast and large inhomogeneous objects. This algorithm is also applied in experimental data. Furthermore, the frequency-hopping scheme is introduced to alleviate nonlinear problems as the object size becomes very large.

The nested equivalence principle algorithm (NEPAL) is introduced in Chapter 4. It is an  $O(N \log N)$  algorithm to perform the matrix-vector multiply. This method is based on Huygens' equivalence principle and, in a nested fashion, calculates the interaction among all subscatterers. It is shown that this algorithm can be further

improved to achieve  $O(N)$  complexity by incorporating the fast multipole method (FMM).

Chapter 5 describes the BiCGFFT T-matrix method for three-dimensional scattering problems involving inhomogeneous bodies. The T-matrix method acts as an alternative to the integral equation formulation. The block Toeplitz property of the translation matrix is suitable for FFT implementation. Therefore, each iteration requires  $O(N \log_2 N)$  operations to effect the matrix-vector multiply. In addition to the scattered fields, the fields can also be calculated inside the inhomogeneous objects. As large as a 90,000-unknown matrix equation can be solved on a workstation.

Ultrasonic waves are also useful imaging tools, and are well-suited for examining biological bodies. The governing equation has the same form as the electromagnetic wave equation for  $H_z$  polarization. Based on this similarity, we introduce the local shape function (LSF) with CGFFT in Chapter 6 to reconstruct both the density and modulus, or compressibility, of inhomogeneous bodies. The LSF inverse scattering algorithm uses the T-matrix formulation combined with the DBIM. The synthetic and experimental data have been processed by this algorithm without a priori knowledge. The reconstruction images show where the objects are located and the details inside the objects.

In Chapter 7, we summarize the conclusions of the algorithms presented in this dissertation. Future research directions of iterative methods and inverse scattering algorithms are also discussed.

Relevant computer code files, as well as input and output files, are listed in the Appendix. Also the use of these computer programs is described.

## 1.1 References

- [1] H. Ling, R. C. Chou, and S. W. Lee, "Shooting and bouncing rays: Calculating the RCS of an arbitrary shaped conductor," *IEEE Trans. Antennas Propag.*, vol. 37, no. 2, pp. 194-205, February 1989.
- [2] J.-P. Berenger, "A perfectly matched layer for the absorption of electromagnetic waves," *J. Computational Physics*, vol. 114, pp. 185-200, 1994.

## CHAPTER 2

### CGFFT AND BICGFFT METHODS ON FORWARD SCATTERING

#### 2.1 Introduction

The conjugate gradient (CG) method was first proposed by Hestenes and Steifel [1] to solve linear systems. It did not gain immediate attention at that time because, for small matrix equations, Gaussian elimination was faster. Recently, as the problem sizes increase, the conjugate gradient method is becoming more popular. The CG method is an iterative method, which requires no matrix storage and one or two matrix-vector multiplies for each iteration. The exact solution can be obtained in at most  $N$  steps [1]-[3] if roundoff errors incurred by computers are absent, where  $N$  is the number of unknowns. For most problems, the CG method converges to the required error tolerance in much fewer than  $N$  steps. In particular, when the eigenvalues of the matrix are clustered, the convergence can be achieved in a few steps. It is this feature that makes the CG method attractive [4]-[6].

The bi-conjugate gradient (BiCG) method for solving linear systems was developed by Lanczos [7], [8] and further discussed by Fletcher [4] and Jacobs [9]. This algorithm has been applied to electromagnetic scattering problems [10], [11]. The BiCG method generally converges faster than the CG method because the latter essentially solves the normal matrix equation, in which the original condition number is squared. However, because the BiCG does not minimize the residual error as the iteration proceeds, the residual error does not decrease monotonically as in the CG method. Moreover, the BiCG method may never converge when it breaks down, although this rarely happens due to the computer roundoff.

Directly implementing the matrix-vector multiply requires  $O(N^2)$  operations. The Green's function in the integral equation assumes the convolution form due to the translational invariance. This nice property enables the use of the fast Fourier

transform (FFT) to perform matrix-vector multiply efficiently. Therefore, the combination of CG or BiCG with FFT is an efficient solver for this particular matrix equation. There has been work applying CGFFT or BiCGFFT to electromagnetics and other areas [12]-[20].

As a prelude to the following chapters, CGFFT and BiCGFFT are applied in this chapter to solve two-dimensional TM polarization scattering problem from inhomogeneous bodies. Both lossless and lossy objects are considered. The convergence rate is faster for lossy media, which indicates that the distribution of the eigenvalues are more clustered for lossy objects.

The CG or BiCG methods provide solutions that are only valid for one incident angle; the solver has to be invoked again whenever the incident angle changes. The recursive aggregate T-matrix algorithm (RATMA) [21]-[24], on the other hand, is a full solver: once the scattering coefficients for the object are found, they are good for any incident angle. RATMA is an  $O(N^2)$  algorithm. Comparisons of CGFFT, BiCGFFT and RATMA are provided. In lossless media, RATMA is the best method; in the lossy media, BiCGFFT is the better one.

## 2.2 Formulation and Algorithms

### 2.2.1 Integral equation and its Toeplitz structure

We consider a two-dimensional TM problem for an inhomogeneous object as shown in Figure 2.1. The field values inside the object can always be represented by the integral equation

$$\phi(\mathbf{r}) = \phi^{inc}(\mathbf{r}) + \int d\mathbf{r}' g_b(\mathbf{r} - \mathbf{r}') O(\mathbf{r}') \phi(\mathbf{r}'), \quad (2.1)$$

where  $\mathbf{r}$  and  $\mathbf{r}'$  are the position vectors,  $g_b(\mathbf{r} - \mathbf{r}')$  is the Green's function of the background medium,  $\phi(\mathbf{r})$  and  $\phi^{inc}(\mathbf{r})$  are the total field and the incident field, respectively, and  $O(\mathbf{r}') = k^2(\mathbf{r}') - k_b^2(\mathbf{r}')$  is the object function. The explicit form of  $g_b(\mathbf{r} - \mathbf{r}')$  for a homogeneous background is  $\frac{i}{4} H_0^{(1)}(k_b |\mathbf{r} - \mathbf{r}'|)$ , in which  $|\mathbf{r} - \mathbf{r}'|$  represents the length of  $\mathbf{r} - \mathbf{r}'$ , and  $H_0^{(1)}(x)$  is a 0th order Hankel Function of the

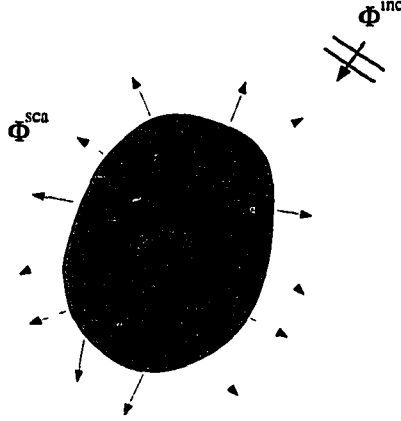


**Figure 2.1.** A two-dimensional scattering problem from an inhomogeneous body for TM polarization.

first kind [38]. After discretization, the above integral equation can be written as

$$(\bar{\mathbf{I}} - \bar{\mathbf{G}} \cdot \bar{\mathbf{O}}) \cdot \mathbf{x} = \mathbf{b}, \quad (2.2)$$

where  $\bar{\mathbf{I}}$  is the identity matrix,  $\bar{\mathbf{O}}$  is a diagonal matrix with the diagonal terms  $k_0^2(\epsilon_r(\mathbf{r}_{ij}) - \epsilon_r^b(\mathbf{r}_{ij}))$ , in which  $\mathbf{r}_{ij}$  is the position vector of the cell center and subscripts  $i$  and  $j$  denote the cell centered at  $i\Delta x$  and  $j\Delta y$ . Because each cell is assumed square,  $\Delta x = \Delta y = \Delta$ , which is the incremental length of each cell. Similarly,  $\mathbf{b}$  is the known incident field containing  $\phi^{inc}(\mathbf{r}_{mn})$ , and  $\mathbf{x}$  is the unknown total field,  $\phi(\mathbf{r}_{mn})$  inside the object. The explicit form of  $g_b(\mathbf{r} - \mathbf{r}')$  shows that the interaction between any two points depends only on their relative position. Because the discretized grid is a regular grid and  $g_b(\mathbf{r} - \mathbf{r}')$  assumes the convolution form,  $\bar{\mathbf{G}}$  is a Toeplitz matrix whose elements can be explicitly expressed as

$$\begin{aligned} [\bar{\mathbf{G}}]_{mn,ij} &= [\bar{\mathbf{G}}]_{m-i,n-j} = \frac{ik_0^2}{4} \int_{D_{ij}} d\mathbf{r}' H_0^{(1)}(k_b|\mathbf{r}_{mn} - \mathbf{r}'|) \\ &= \begin{cases} \frac{ik_0^2}{2k_b^2} \left[ \pi k_b a_e H_1^{(1)}(k_b a_e) + i2 \right], & \text{for } m = i \text{ and } n = j \\ \frac{ik_0^2 \pi a_e}{2k_b^2} H_0^{(1)}(k_b r_{m-i,n-j}) J_1(k_b a_e), & \text{otherwise,} \end{cases} \end{aligned} \quad (2.3)$$

where  $D_{ij}$  denotes the cell whose center is at  $\mathbf{r}_{ij}$ ,  $a_e = \frac{\Delta}{\sqrt{\pi}}$  and  $r_{m-i,n-j} = |\mathbf{r}_{mn} - \mathbf{r}_{ij}|$ . In the above formulas, each square cell is approximated by a circle with the same area [25].

### 2.2.2 CG and BiCG algorithms

For the matrix equation  $\bar{\mathbf{A}} \cdot \mathbf{x} = \mathbf{b}$ , the CG algorithm is as follows:

$$\begin{aligned}
\mathbf{r}_0 &= \mathbf{b} - \bar{\mathbf{A}} \cdot \mathbf{x}_0, & \mathbf{p}_0 &= \frac{\bar{\mathbf{A}}^a \cdot \mathbf{r}_0}{\|\bar{\mathbf{A}}^a \cdot \mathbf{r}_0\|^2}, \\
\alpha_n &= \frac{1}{\|\bar{\mathbf{A}} \cdot \mathbf{p}_n\|^2}, & \mathbf{x}_{n+1} &= \mathbf{x}_n + \alpha_n \mathbf{p}_n, & \mathbf{r}_{n+1} &= \mathbf{r}_n - \alpha_n \bar{\mathbf{A}} \cdot \mathbf{p}_n, \\
\beta_n &= \frac{1}{\|\bar{\mathbf{A}}^a \cdot \mathbf{r}_{n+1}\|^2}, & \mathbf{p}_{n+1} &= \mathbf{p}_n + \beta_n \bar{\mathbf{A}}^a \cdot \mathbf{r}_{n+1},
\end{aligned} \tag{2.4}$$

where the  $\mathbf{x}_0$  is the initial guess,  $\|\cdot\|$  is the Euclidean norm of the complex vector, and  $\mathbf{A}^a$  is the complex conjugate transpose of  $\mathbf{A}$ . This algorithm is valid for any matrix and minimizes the residual error  $\mathbf{r}_n$  as the iteration proceeds. Note that there are two matrix-vector multiplies involved in each iteration:  $\bar{\mathbf{A}} \cdot \mathbf{p}_n$  and  $\bar{\mathbf{A}}^a \cdot \mathbf{r}_{n+1}$ .

The BiCG algorithm for a symmetric  $\bar{\mathbf{A}}$ :

$$\begin{aligned}
\mathbf{r}_0 &= \mathbf{b} - \bar{\mathbf{A}} \cdot \mathbf{x}_0, & \mathbf{p}_0 &= \mathbf{r}_0, \\
\alpha_n &= \frac{\langle \mathbf{r}_n, \mathbf{r}_n \rangle}{\langle \bar{\mathbf{A}} \cdot \mathbf{p}_n, \mathbf{p}_n \rangle}, & \mathbf{x}_{n+1} &= \mathbf{x}_n + \alpha_n \mathbf{p}_n, & \mathbf{r}_{n+1} &= \mathbf{r}_n - \alpha_n \bar{\mathbf{A}} \cdot \mathbf{p}_n, \\
\beta_n &= \frac{\langle \mathbf{r}_{n+1}, \mathbf{r}_{n+1} \rangle}{\langle \mathbf{r}_n, \mathbf{r}_n \rangle}, & \mathbf{p}_{n+1} &= \mathbf{r}_{n+1} + \beta_n \mathbf{p}_n,
\end{aligned} \tag{2.5}$$

where  $\langle \mathbf{v}, \mathbf{w} \rangle = \mathbf{v}^t \cdot \mathbf{w}$ . Unlike the CG algorithm, there is only one matrix-vector multiply in each iteration.

The BiCG algorithm for an arbitrary  $\bar{\mathbf{A}}$  is as follows:

$$\begin{aligned}
\mathbf{p}_0 &= \mathbf{r}_0 = \mathbf{b} - \bar{\mathbf{A}} \cdot \mathbf{x}_0, \\
\mathbf{q}_0 &= \mathbf{s}_0 = \mathbf{r}_0^* \quad (\text{Jacobs}) \quad \text{or} \quad \bar{\mathbf{A}} \cdot \mathbf{r}_0 \quad (\text{Fletcher}), \\
\mathbf{x}_{n+1} &= \mathbf{x}_n + \alpha_n \mathbf{p}_n, \\
\mathbf{r}_{n+1} &= \mathbf{r}_n - \alpha_n \bar{\mathbf{A}} \cdot \mathbf{p}_n, \quad \mathbf{s}_{n+1} = \mathbf{s}_n - \alpha_n \bar{\mathbf{A}}^T \cdot \mathbf{q}_n, \quad \alpha_n = \frac{\langle \mathbf{r}_n, \mathbf{s}_n \rangle}{\langle \bar{\mathbf{A}} \cdot \mathbf{p}_n, \mathbf{q}_n \rangle}, \\
\mathbf{p}_{n+1} &= \mathbf{r}_{n+1} + \beta_n \mathbf{p}_n, \quad \mathbf{q}_{n+1} = \mathbf{s}_{n+1} + \beta_n \mathbf{q}_n, \quad \beta_n = \frac{\langle \mathbf{r}_{n+1}, \mathbf{s}_{n+1} \rangle}{\langle \mathbf{r}_n, \mathbf{s}_n \rangle},
\end{aligned} \tag{2.6}$$

where  $*$  denotes the complex conjugate and  $\bar{\mathbf{A}}^T$  is the transpose of  $\bar{\mathbf{A}}$ . Each iteration requires two matrix-vector multiplies:  $\bar{\mathbf{A}} \cdot \mathbf{p}_n$  and  $\bar{\mathbf{A}}^T \cdot \mathbf{q}_n$ .

We apply the CG algorithm to solve Equation (2.1). However, we can convert Equation (2.1) into a symmetric equation by left-multiplying Equation (2.1) by  $\bar{\mathbf{O}}$ :

$$(\bar{\mathbf{O}} - \bar{\mathbf{O}} \cdot \bar{\mathbf{G}} \cdot \bar{\mathbf{O}}) \cdot \mathbf{x} = \bar{\mathbf{O}} \cdot \mathbf{b}. \tag{2.7}$$

Therefore, we can use the symmetric matrix version of the BiCG algorithm (2.5) so that each iteration saves a matrix-vector multiply. Note that in Equations (2.5) and (2.6), the denominator of  $\beta_n$  could be zero under exact arithmetic, which renders the BiCG method unusable. But this situation is unlikely to happen in most cases.

### 2.2.3 Matrix-vector multiply by fast Fourier transform

In the previous section, we described three iterative algorithms to solve the matrix equation. The bottleneck is the matrix-vector multiply in each iteration. In implementing the matrix-vector multiply directly, the computational cost is proportional to  $N^2$ , where  $N$  is the number of unknowns. As mentioned in Section 2.2.1, because the matrix  $\bar{\mathbf{G}}$  is a Toeplitz matrix, we can extend  $\bar{\mathbf{G}}$  into a circulant matrix,  $\bar{\mathbf{G}}'$  and append the to-be-multiplied vector  $\mathbf{v}$  by zeros in the end to obtain  $\mathbf{v}'$ . Then, we use the FFT routine to perform the forward transform on any column of  $\bar{\mathbf{G}}'$  and denote it as  $\tilde{\mathbf{G}}$ , and apply FFT on  $\mathbf{v}'$  as well to produce  $\tilde{\mathbf{v}}$ . Following the transformations, we multiply both transformed vectors elements-wise. Finally, the

inverse Fourier transform is performed on the resultant vector and the second half of elements are discarded to obtain the convolution results.

The following one-dimensional example demonstrates the procedure as described above. A matrix  $\bar{\mathbf{T}}$  and vector  $\mathbf{w}$  are given by

$$\bar{\mathbf{T}} = \underbrace{\begin{pmatrix} a & b & c & d & e \\ f & a & b & c & d \\ g & f & a & b & c \\ h & g & f & a & b \\ i & h & g & f & a \end{pmatrix}}_{\text{Toeplitz matrix}} \quad (2.8)$$

and

$$\mathbf{w}^t = [w_1 \ w_2 \ w_3 \ w_4 \ w_5]. \quad (2.9)$$

Extending  $\bar{\mathbf{T}}$  into a circulant matrix,  $\bar{\mathbf{T}}'$  and padding zeros to  $\mathbf{w}$ , we have

$$\bar{\mathbf{T}}' = \underbrace{\begin{pmatrix} a & b & c & d & e & i & h & g & f \\ f & a & b & c & d & e & i & h & g \\ g & f & a & b & c & d & e & i & h \\ h & g & f & a & b & c & d & e & i \\ i & h & g & f & a & b & c & d & e \\ e & i & h & g & f & a & b & c & d \\ d & e & i & h & g & f & a & b & c \\ c & d & e & i & h & g & f & a & b \\ b & c & d & e & i & h & g & f & a \end{pmatrix}}_{\text{Circulant matrix}} \quad (2.10)$$

and

$$\mathbf{w}'^t = [w_1 \ w_2 \ w_3 \ w_4 \ w_5 \ 0 \ 0 \ 0 \ 0 \ 0]. \quad (2.11)$$

It can be easily seen that the first five entities of  $\bar{\mathbf{T}}' \cdot \mathbf{w}'$  are exactly the same as  $\bar{\mathbf{T}} \cdot \mathbf{w}$ . Because  $\bar{\mathbf{T}}'$  is a circulant matrix, which is characterized by any column or row, the FFT of the first row of  $\bar{\mathbf{T}}'$  and the FFT of  $\{\mathbf{w}'\}$  give rise to  $\tilde{\mathbf{T}}$  and  $\tilde{\mathbf{w}}$ , respectively. Then we perform  $\text{FFT}^{-1}\{\tilde{\mathbf{T}}\tilde{\mathbf{w}}\}$  to obtain  $\bar{\mathbf{T}}' \cdot \mathbf{w}'$ .

The flowchart in Figure 2.2 shows the matrix-vector multiply by FFT. Note that  $\tilde{\mathbf{G}}$  has been calculated once and stored for use in each iteration. Therefore, there

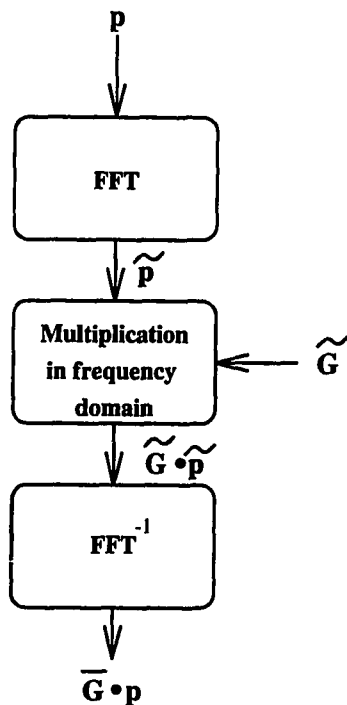


**Figure 2.2.** The flowchart of a matrix-vector multiply by FFT.

is no need of matrix storage by using FFT to perform the matrix-vector multiply, reducing the memory requirement to  $O(N)$ .

## 2.3 Numerical Results

### 2.3.1 Verification

Figures 2.3(a) and 2.3(b) show the comparison of the exact solution and the solution by CGFFT for the far field from a homogeneous circular dielectric object with  $\epsilon_r = 2.0$  and radius  $r = 1.0\lambda_0$ , where  $\lambda_0$  is the free space wavelength. The agreement is very good. The next example is for a two-layered dielectric circle. The inner layer has  $\epsilon_{r1} = 2.0 + i0.4$  and  $r_1 = 0.5\lambda_0$ ; the outer layer has  $\epsilon_{r2} = 1.5 + i0.2$  and  $r_2 = 1.0\lambda_0$ . Again, the two lines for the far fields in Figures 2.4(a) and 2.4(b) are indistinguishable.

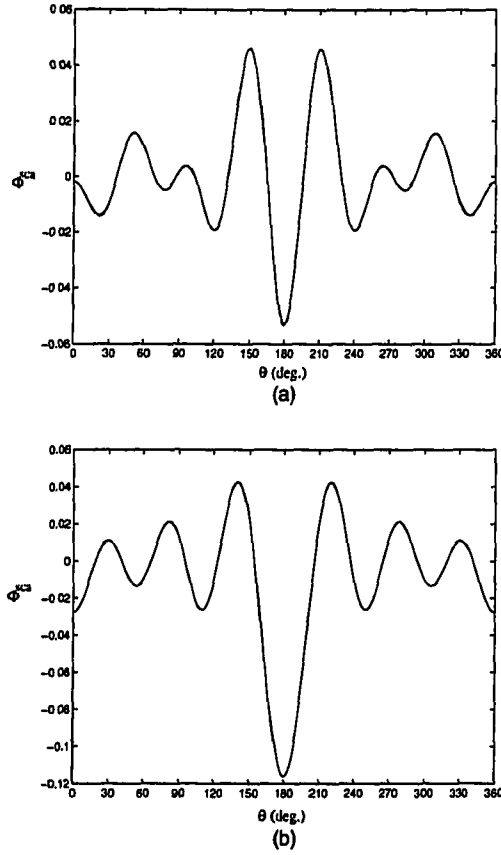


**Figure 2.3.** Comparison of the exact far field solution (solid line) and the solution by CGFFT algorithm (dashed line) from a homogeneous dielectric circle with  $\epsilon_r = 2.0$  and radius  $r = 1.0\lambda_0$ : (a) real component (b) imaginary component.

### 2.3.2 Comparisons of CGFFT, BiCGFFT and RATMA

Figure 2.5 shows the number of iterations versus the number of unknowns for a lossless square of  $\epsilon_r = 2.0$  by CGFFT and BiCGFFT. The square is divided into a regular grid with 12 points per  $\lambda_0$ . BiCGFFT converges faster than CGFFT because the BiCG algorithm deals with the original matrix equation directly. According to

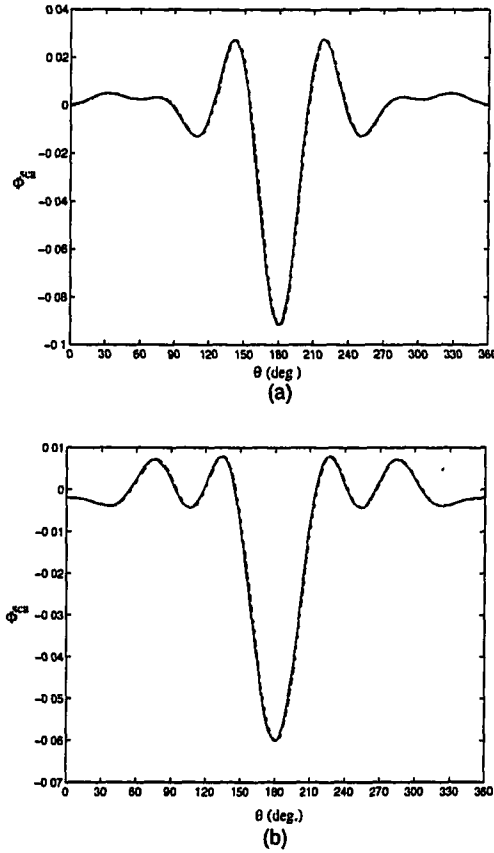


**Figure 2.4.** Comparison of the exact far field solution (solid line) and the solution by CGFFT algorithm (dashed line) from a two-layered dielectric circle with  $\epsilon_{r1} = 2.0 + i0.4$  and  $r_1 = 0.5\lambda_0$  for the inner layer;  $\epsilon_{r2} = 1.5 + i0.2$  and  $r_2 = 1.0\lambda_0$  for the outer layer: (a) real component (b) imaginary component.

the theorem in [2], the iteration number of CGM grows linearly as the square root of the condition number of the matrix. But since CGM actually solves the normal equation, the condition number is squared and the number of iterations has a linear growth with  $N$ . This point is demonstrated in Figure 2.5. Although when the BiCG

algorithm is used, the original equation is solved, the non-monotonically decreasing residual error implies more iterations to converge than we expect. Also, as noted at the end of the Section 2.2.2, the BiCG algorithm is more sensitive to the accuracy of numerics, especially when the problem size or the contrast of the medium is large. Nonetheless, BiCGM converges faster than CGM in general. We consider the lossy media with  $\epsilon_r = 2.0 + i0.5$  in Figure 2.6. It shows that the number of iterations to converge is much less than that for the lossless case with the same problem size. It is observed that the iteration number of CGM changes with the unknowns in  $\sqrt{N}$  fashion, and that BiCGM exhibits even better convergence behavior. This implies that in the lossy medium, the eigenvalues of the matrix are more clustered than those in the lossless medium. Therefore, when the distribution of eigenvalues is reasonably well confined, a superlinear convergence rate can be expected.

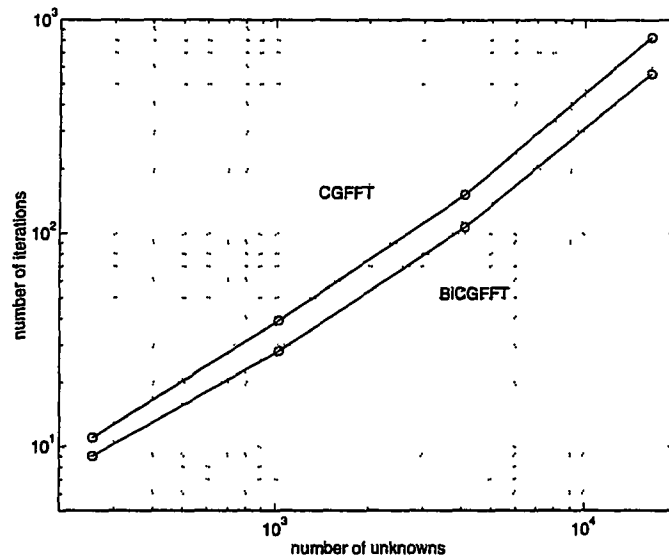


**Figure 2.5.** The number of iterations vs. the number of unknowns for lossless dielectric squares of  $\epsilon_r = 2.0$  by CGFFT and BiCGFFT with  $10^{-3}$  residual error.

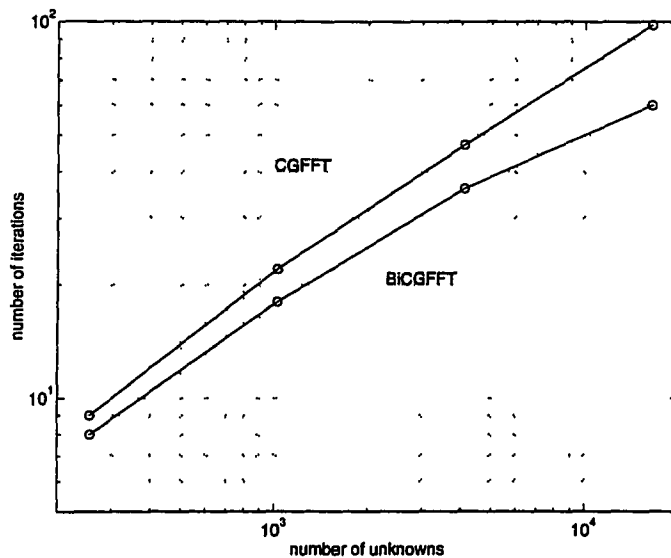
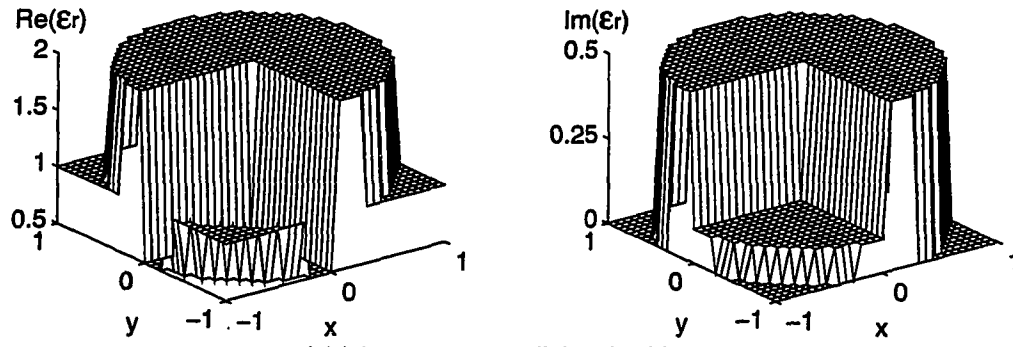
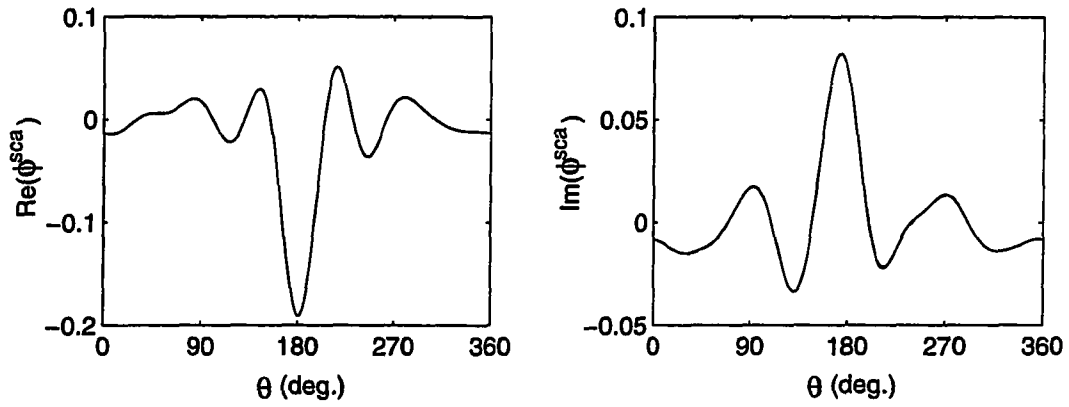


**Figure 2.6.** The number of iterations vs. the number of unknowns for lossy dielectric squares of  $\epsilon_r = 2.0 + i0.5$  by CGFFT and BiCGFFT with  $10^{-3}$  residual error.

Figure 2.7 shows an inhomogeneous dielectric object and its scattered field calculated by CGFFT (solid line) and RATMA (dashed line); two lines agree with each other very well. Because there is no analytic solution to this problem, we compare the results by CGFFT and RATMA, which are differently formulated, to examine the validity of both algorithms. RATMA had been developed in our research group and details of the algorithm can be found in [21]-[24], [26]. In the following, only a brief description of RATMA is provided. RATMA is a recursive algorithm. An inhomogeneous scatterer is first divided into  $N$  subscatterers. The scattering by each subscatterer is then expressed in terms of a T matrix. The scattering solution from these  $N$  subscatterers is sought recursively so that the  $(n + 1)$ -subscatterer solution is obtained from the  $n$ -subscatterer solution. When the scattering solution is found for  $(n + 1)$  subscatterers, then an aggregate T matrix is again defined for



(a) inhomogeneous dielectric object



(b) scattered field calculated by CGFFT (solid line) and RATMA (dashed line)

**Figure 2.7.** An inhomogeneous dielectric object and its scattered field by CGFFT and RATMA.

these scatterers. This procedure is repeated until all of the  $N$  subscatterers are exhausted.

When  $n$  subscatterers are present, the total field outside the scatterers can be expressed as [22], [26]

$$\phi(\mathbf{r}) = \Re g \psi^t(k_b, \mathbf{r}_0) \cdot \mathbf{a} + \psi^t(k_b, \mathbf{r}_0) \cdot \bar{\tau}_{(n)} \cdot \mathbf{a}, \quad (2.12)$$

where  $\psi^t(k_b, \mathbf{r}_0)$  is a row vector containing all of the wave harmonics,  $\mathbf{a}$  is a column vector containing the amplitudes of the incident field, and  $\bar{\tau}_{(n)}$  is the aggregate T matrix for  $n$  subscatterers. “ $\Re g$ ” here stands for “regular part.” Recursive formulas for  $\bar{\tau}_{(n)}$  can be found in [22] and [26]. RATMA is an  $O(N^2)$  algorithm for all incident angles, and the required memory storage is of  $O(N)$ .

In Figures 2.8 and 2.9, we compare the CPU time on a SPARC 10 for CGFFT, BiCGFFT and RATMA. For lossless media as shown in Figure 2.8, RATMA is the most efficient as the problem size becomes larger, because both CGFFT and BiCGFFT are  $O(N^2 \log_2 N)$  algorithms in this case. In the comparison, not only is the scattered field calculated, but the internal field is also found by CGFFT, BiCGFFT and RATMA [22]. BiCGFFT is more efficient than CGFFT in that the former converges faster than the latter and BiCG requires only one matrix-vector multiply, because the symmetric matrix formulation (Equation (2.7)) is used.

In the lossy cases of Figure 2.9, we observed the opposite phenomenon: the other two iterative methods are more computationally efficient than RATMA. As explained above, the convergence rate is superlinear for lossy media due to the more compact distribution of eigenvalues. Yet the CPU time of RATMA does not depend on the property of the media. However, it is emphasized that RATMA is a full solver that is valid for different incident fields; CGFFT or BiCGFFT have to be invoked whenever the incident field changes.

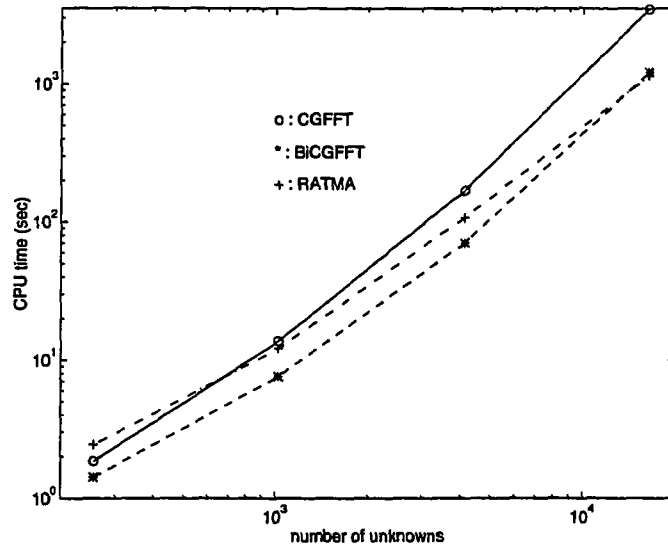


**Figure 2.8.** The CPU time comparison of RATMA, CGFFT and BiCGFFT for a lossless dielectric square of  $\epsilon_r = 2.0$  and with  $10^{-3}$  residual error.

## 2.4 Conclusions

CGFFT and BiCGFFT are  $O(N_i N \log_2 N)$  algorithms with  $O(N)$  required memory storage, where  $N_i$  is the number of iterations to converge. In our simulation cases, for integral equations for electromagnetic scattering problems from inhomogeneous bodies,  $N_i$  is proportional to  $N$  for lossless media and to  $\sqrt{N}$  for lossy media (even better than  $\sqrt{N}$  for BiCGFFT). The BiCG algorithm usually converges faster than the CG algorithm. Both iterative algorithms have to be restarted whenever the right-hand side changes. But the  $O(N^2)$  algorithm RATMA can be reused for different incident fields without solving the problem again. Therefore, when solutions for many incident angles are required, such as for monostatic RCS calculation, RATMA is the better choice. If only a few incident fields are consid-

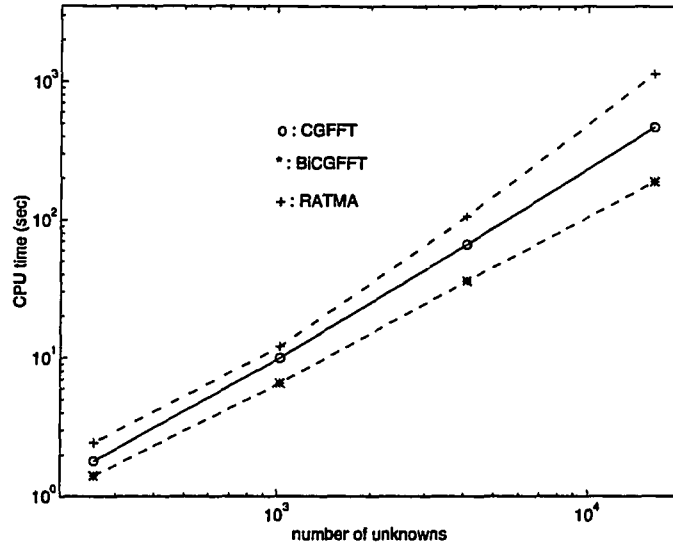


**Figure 2.9.** The CPU time comparison of RATMA, CGFFT and BiCGFFT for a lossy dielectric square of  $\epsilon_r = 2.0 + i0.5$  and with  $10^{-3}$  residual error.

ered, CGFFT or BiCGFFT is more efficient when the convergence rate is better than  $O(N)$ . Another case which may favor CGFFT or BiCGFFT is when a good initial guess is available and the algorithm converges within only several iterations. An example will be introduced in Chapter 3.

As we have seen, the convergence rate of iterative methods depends on spectral properties of the coefficient matrix. Hence, one may attempt to transform the original linear system into a new system with the same solution but with more favorable eigenvalue distribution. A preconditioner is a matrix that effects such transformation. An ideal preconditioner is very close to the original matrix and easy to implement without incurring too much extra cost. For example, if a matrix

$\bar{\mathbf{M}}$  approximates  $\bar{\mathbf{A}}$  in some way, the transformed system

$$\bar{\mathbf{M}}^{-1} \cdot \bar{\mathbf{A}} \cdot \mathbf{x} = \bar{\mathbf{M}}^{-1} \cdot \mathbf{b} \quad (2.13)$$

has the same solution as  $\bar{\mathbf{A}} \cdot \mathbf{x} = \mathbf{b}$  but the eigenvalues of  $\bar{\mathbf{M}}^{-1} \cdot \bar{\mathbf{A}}$  may be more clustered. Unfortunately, no universal routine exists that finds an optimal preconditioner. It is usually problem dependent. There are many research works on the preconditioners [27]-[30], most of which are operated on sparse matrix systems. Preconditioners for dense matrices exist only for some systems with special structures [31]-[37]. Suitable preconditioners for the matrix equation in this chapter are not available yet and are worthy of more effort and study in order to make iterative methods more appealing and feasible.

## 2.5 References

- [1] M. R. Hestenes and E. Stiefel, "Methods of conjugate gradient for solving linear systems," *J. Res. Natl. Bur. Stand.*, vol. 49, pp. 409-435, 1952.
- [2] O. Axelsson and V. A. Barker, *Finite Element Solution of Boundary Value Problems: Theory and Computation*. New York: Academic Press, 1984.
- [3] G. H. Golub and C. F. Van Loan, *Matrix Computations*, 2nd ed. Baltimore: John Hopkins University Press, 1989.
- [4] R. Fletcher, "Conjugate gradient methods for indefinite systems," in *Numerical Analysis Dundee 1975*, G. A. Watson, Ed. New York: Springer-Verlag, 1976, pp. 73-89.
- [5] C. C. Paige and M. A. Saunders, "Solution of sparse indefinite systems of linear equations," *SIAM J. Numer. Anal.*, vol. 12, no. 4, pp. 617-629, 1975.
- [6] M. R. Hestenes, *Conjugate Direction Methods in Optimization*. New York: Springer-Verlag, 1980.
- [7] C. Lanczos, "An iteration method for the solution of the eigenvalue problem of linear differential and integral operators," *J. Res. Nat. Bur. Stand.*, vol. 45, pp. 255-282, 1950.
- [8] C. Lanczos, "Solution of systems of linear equations by minimized iterations," *J. Res. Nat. Bur. Stand.*, vol. 49, pp. 33-53, 1952.
- [9] D. A. H. Jacobs, "The exploitation of sparsity by iterative methods," *Sparse Matrices and Their Uses*, I. S. Duff, Ed. Berlin: Springer-Verlag, 1981, pp. 191-222.

- [10] T. K. Sarkar, "On the application of the generalized bi-conjugate gradient method," *J. Electromagn. Waves Appl.*, vol. 1, no. 3, pp. 223-242, 1987.
- [11] C. F. Smith, A. F. Peterson, and R. Mittra, "The biconjugate gradient method for electromagnetic scattering," *IEEE Trans. Antennas Propag.*, vol. 38, no. 6, pp. 938-940, 1990.
- [12] D. T. Borup and O. P. Gandhi, "Calculation of high-resolution SAR distributions in biological bodies using the FFT algorithm and conjugate gradient method," *IEEE Trans. Microwave Theory Tech.*, vol. 33, no. 5, pp. 417-419, 1985.
- [13] D. T. Borup, D. M. Sullivan, and O. P. Gandhi, "Comparison of the FFT conjugate gradient method and the finite-difference time-domain method for the 2-D absorption problem," *IEEE Trans. Microwave Theory Tech.*, vol. 35, no. 4, pp. 383-395, 1987.
- [14] T. K. Sarkar, "Application of FFT and the conjugate gradient method for the solution of electromagnetic radiation from electrically large and small conducting bodies," *IEEE Trans. Antennas Propag.*, vol. 34, no. 5, pp. 635-640, 1986.
- [15] M. F. Cátedra, "Solution to some electromagnetic problems using fast Fourier transform with conjugate gradient method," *Electron. Lett.*, vol. 22, no. 20, pp. 1049-1051, 1986.
- [16] T. J. Peters and J. L. Volakis, "On the formulation and implementation of a conjugate gradient FFT method," *J. Electromag. Waves Appl.*, vol. 3, no. 8, pp. 675-696, 1989.
- [17] C. Y. Shen, K. J. Glover, M. I. Sancer, and A. D. Varvatsis, "The discrete Fourier transform method of solving differential-integral equations in scattering theory," *IEEE Trans. Antennas Propag.*, vol. 37, no. 8, pp. 1032-1041, 1989.
- [18] K. Barkeshli and J. L. Volakis, "On the implementation of the conjugate gradient Fourier transform method for scattering by planar plates," *IEEE Antennas Propag. Soc. Mag.*, pp. 19-26, April 1990.
- [19] A. P. M. Zwamborn and P. M. van den Berg, "A weak form of the conjugate gradient FFT method for plate problems," *IEEE Trans. Antennas Propag.*, vol. 39, no. 2, pp. 224-228, 1991.
- [20] J.-H. Lin and W. C. Chew, "A comparison of the CG-FFT method and the recursive aggregate T-matrix algorithm," in *IEEE Antennas and Propagation Society International Symposium Digest*, pp. 1591-1594, 1992.
- [21] W. C. Chew, "An  $N^2$  algorithm for the multiple scattering solution of  $N$  scatterers," *Microw. Opt. Tech. Lett.*, vol. 2, no. 11, pp. 380-383, November 1989.

- [22] W. C. Chew and Y. M. Wang, "A fast algorithm for solution of a scattering problem using a recursive aggregate tau matrix method," *Microw. Opt. Tech. Lett.*, vol. 3, no. 5, pp. 164-169, May 1990.
- [23] W. C. Chew, *Waves and Fields in Inhomogeneous Media*. New York: Van Nostrand Reinhold, 1990.
- [24] J.-H. Lin and W. C. Chew, "Solution of oblong, dielectric coated, metallic scatterer by the recursive algorithm," *Electron. Lett.*, vol. 28, no. 2, pp. 185-186, Jan. 1992.
- [25] J. H. Richmond, "Scattering by a dielectric cylinder of arbitrary cross section shape," *IEEE Trans. Antennas Propag.*, vol. 13, no. 5, pp. 334-341, May 1965.
- [26] Y. M. Wang and W. C. Chew, "An efficient algorithm for solution of a scattering problem," *Microw. Opt. Tech. Lett.*, vol. 3, no. 3, pp. 102-106, March 1990.
- [27] O. Axelsson, "A class of iterative methods for finite element equations," *Computer Methods in Applied Mechanics and Engineering*, vol. 9, pp. 123-137, 1976.
- [28] O. Axelsson, "A survey of preconditioned iterative methods for linear systems of algebraic equations," *BIT*, vol. 25, pp. 166-187, 1985.
- [29] Y. Saad, "Krylov subspace methods on supercomputers," *SIAM J. Sci. Stat. Comput.*, vol. 10, no. 6, pp. 1200-1232, 1989.
- [30] A. Meyer, "A parallel preconditioned conjugate gradient method using domain decomposition and inexact solvers on each subdomain," *Computing*, vol. 45, pp. 217-234, 1990.
- [31] G. Strang, "A proposal for Toeplitz matrix calculations," *Studies in Applied Mathematics*, vol. 74, pp. 171-176, 1986.
- [32] A. Kas and E. L. Yip, "Preconditioned conjugate gradient methods for solving electromagnetic problems," *IEEE Trans. Antennas Propag.*, vol. 35, no. 2, pp. 147-152, 1987.
- [33] R. H. Chan and G. Strang, "Toeplitz equations by conjugate gradients with circulant preconditioner," *SIAM J. Sci. Stat. Comput.*, vol. 10, no. 1, pp. 104-119, 1989.
- [34] E. E. Tyrtysnikov, "Optimal and superoptimal circulant preconditioners," *SIAM J. Matrix Anal. Appl.*, vol. 13, no. 2, pp. 459-473, 1992.
- [35] R. H. Chan and M. C. Yeung, "Circulant preconditioners for complex Toeplitz matrices," *SIAM J. Numer. Anal.*, vol. 30, no. 4, pp. 1193-1207, 1993.

- [36] Y. Yan, "Sparse preconditioned iterative methods for dense linear systems," *SIAM J. Sci. Comput.*, vol. 15, no. 5, pp. 1190-1200, 1994.
- [37] T. F. Cahn and J. A. Olkin, "Circulant preconditioners for Toeplitz-block matrices," *Numerical Algorithms*, vol. 6, pp. 89-101, 1994.
- [38] M. Abramowitz and I. A. Stegun, *Handbook of Mathematical Functions*. New York: Dover Publications, 1965.

# CHAPTER 3

## INVERSE SCATTERING BY THE DISTORTED BORN ITERATIVE METHOD WITH CGFFT

### 3.1 Introduction

In inverse scattering, one finds parameters of an object from the measured scattered fields. These parameters could be the location, shape and size of a conducting cylinder [1]-[8]; the dielectric constants of an inhomogeneous object [9]-[16]; the conductivity of underground for well-logging [17]-[19]; or the soil moisture, trunk and leaf density for remote sensing [20].

Inverse scattering is plagued by nonlinearity and the ill-posed nature of the problem. Nonlinearity makes it difficult to solve the problem directly. Conventionally, one can assume a known internal field or current distribution, and then solve for the parameters. The Born approximation is a famous example for this approach. It assumes that the internal field is the incident field and then the relationship between the scattered field and the permittivity can be reduced to a simple Fourier transform. The diffraction tomography technique [27]-[29] belongs to this category. This kind of method suffers from the assumption that the scatterer is a weak scatterer and the object size is small compared to the wavelength. Therefore, it is not surprising that the Born approximate method cannot always retrieve the parameters successfully. A remedy to this method is to iteratively apply the Born approximation. This gives rise to the Born iterative method (BIM) [9].

The ill-posedness of the inverse scattering problems results from the lack of high-frequency information. Because the high-frequency components constitute the evanescent waves and attenuate rapidly, the matrix has a null space. In other words, it contains some zero eigenvalues. Ill-posed problems lead to non-unique solutions, and they are very sensitive to small discrepancies in the measurement data and in

the coefficient matrix. The regularization method [12], [21]-[26] serves the purpose of stabilizing the solutions and of providing a unique solution.

Unlike the diffraction tomography technique, the nonlinear inverse scattering algorithm accounts for multiple scattering. Take the Born iterative method for example. In each iteration, it needs to solve a forward problem related to the total field inside the object. Therefore, an efficient forward solver plays a key role in the inverse scattering algorithm. From the discussion of the previous chapter, CGFFT is a good choice to this end.

To gain more information about the unknown object, a multiple view scheme is usually applied. The schematic experimental setup is shown in Figure 3.1. Transmitters and receivers are placed on the same circle containing the unknown object. With each transmitter emitting a probing wave, all other receivers measure the field at each location. The configuration in Figure 3.1 is also known as a full-angle imaging system, as opposed to the limited-view system, for example, as in subsurface radar.

First, a cost function is defined as the difference between the measurement data and the calculated fields under the current object profile. A minimization method such as the conjugate gradient method is employed to find the minimal solution of the functional iteratively. Each iteration requires the gradient to determine the direction of the next step and the Hessian to find the step size along that direction. CGFFT is invoked as the forward solver to find the total field for each probing wave.

In the simulation examples, we demonstrate the capability of reconstructing high-contrast large inhomogeneous bodies by using the distorted Born iterative method (DBIM) [10], [13], [15] with CGFFT. The difference between the BIM and DBIM is that the background medium for the former algorithm is assumed unchanged throughout the iterations; on the other hand, the background medium for DBIM is the object profile from the previous iteration. We also apply the inverse

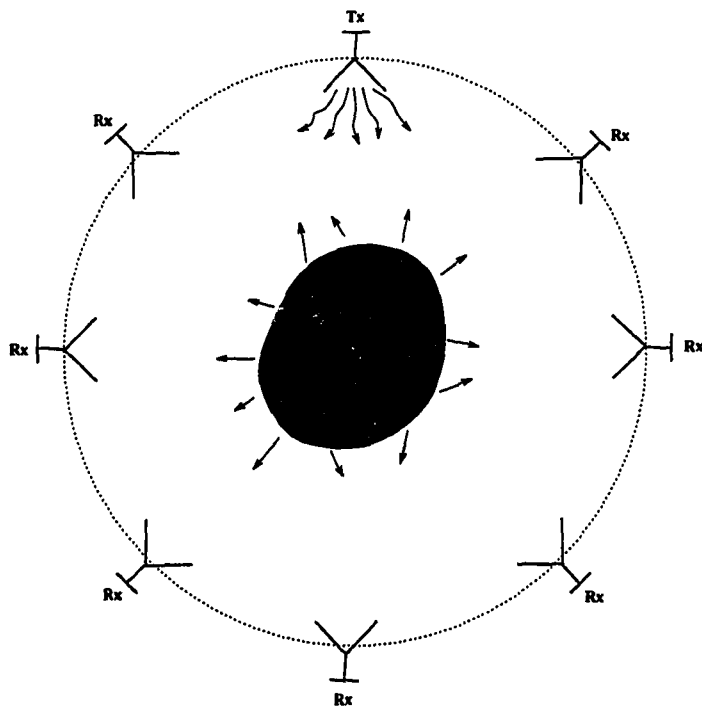


**Figure 3.1.** The schematic experimental setup for a multiple view scheme.

scattering algorithm to the experimental data provided from Barcelona research group in Spain [30]. The reconstructed images of a human arm show where the bones and muscle are located.

As the object becomes larger, the nonlinearity becomes more pronounced. A single-frequency reconstruction scheme does not yield a good image when the object becomes larger and/or the contrast is more pronounced. A multiple-frequency scheme is proposed to alleviate the difficulty. The frequency-hopping approach begins from the lowest available frequency and obtains the image, which will be used as the initial guess for the next higher frequency. We found that the nonlinear effect can be mitigated. An inhomogeneous body as large as  $10\lambda \times 10\lambda$  can be reconstructed with high fidelity.

### 3.2 Conjugate Gradient Minimization Scheme

In inverse scattering, we address the problem that given the column vector of measurement data,  $\Phi_{meas}^{sca}$  at different transmitters and receivers, we try to reconstruct the object function  $O(\mathbf{r}') = \omega^2 \mu \epsilon(\mathbf{r}') - \omega^2 \mu \epsilon_b(\mathbf{r}')$ . It is nonlinear because of multiple scattering. The strategy to this nonlinear problem is to iteratively optimize a cost function, which reflects the difference of the measurement data and the simulation data from an estimated object profile. A cost function can be defined as

$$S(\epsilon) = \frac{1}{2} (\|\Phi^{sca}(\epsilon) - \Phi_{meas}^{sca}\|^2 + \gamma \|\epsilon - \epsilon_b\|^2), \quad (3.1)$$

where  $\epsilon$  and  $\epsilon_b$  contain the discretized values of  $\epsilon(\mathbf{r}')$  and  $\epsilon_b(\mathbf{r}')$ . Note that the second norm in the above equation serves as the regularization to circumvent the inherent ill-condition nature of the inverse scattering problems and  $\gamma$  is the regularization parameter and a real number. This regularization method is a standard Tikhonov regularization [21].

A Newton-type minimization method, the conjugate gradient algorithm, is used to minimize the cost function. In each iteration, the gradient of the functional is required to calculate the conjugate vector and the Hessian to find the step size, where it is assumed that the functional changes quadratically with the object profile.

The conjugate gradient minimization scheme can be listed as follows:

- (i) For  $n = 0, 1, 2, \dots$
- (ii) If (  $\|\Phi^{sca}(\epsilon) - \Phi_{meas}^{sca}\| < \epsilon$  ) Stop
- (iii)  $\mathbf{g}_n = -\mathbf{v}_n$  (  $\mathbf{v}$  is the gradient of  $S$  )
- (iv)  $\mathbf{h}_n = \mathbf{g}_n + c_{n-1} \mathbf{h}_{n-1}$ ,  
where  $c_{n-1} = \frac{(\mathbf{g}_n - \mathbf{g}_{n-1})^t \cdot \mathbf{g}_n}{\mathbf{g}_{n-1}^t \cdot \mathbf{g}_{n-1}}$
- (v)  $\epsilon_{n+1} = \epsilon_n + a_n \mathbf{h}_n$ ,  $a_n = \frac{\mathbf{g}_n^t \cdot \mathbf{h}_n}{\mathbf{h}_n^t \cdot \overline{\mathbf{H}}_n \cdot \mathbf{h}_n}$
- (vi) Continue ...

For the first iteration,  $n = 0$ , the background medium is usually assumed as the initial guess. We invoke an efficient forward solver to solve for fields inside the reconstruction area and then calculate the scattered fields at the receivers. We compare the calculated scattered fields with the measured fields. If the difference is within the specified residual error, we stop the iteration. Otherwise, the object profile is updated according to (iii)-(v).

The gradient  $\mathbf{v}$  and the Hessian  $\overline{\mathbf{H}}$  are calculated respectively as

$$\begin{aligned} \mathbf{v} &= \left( \frac{\partial S}{\partial \epsilon^r}, \frac{\partial S}{\partial \epsilon^i} \right)^t \\ &= \begin{pmatrix} \Re \left\{ \overline{\mathbf{F}}^\dagger \cdot (\Phi^{sca}(\epsilon) - \Phi_{meas}^{sca}) + \gamma(\epsilon - \epsilon_b) \right\} \\ \Im \left\{ \overline{\mathbf{F}}^\dagger \cdot (\Phi^{sca}(\epsilon) - \Phi_{meas}^{sca}) + \gamma(\epsilon - \epsilon_b) \right\} \end{pmatrix} \end{aligned} \quad (3.2)$$

and

$$\begin{aligned} \overline{\mathbf{H}} &= \begin{pmatrix} \frac{\partial^2 S}{\partial \epsilon^r \partial \epsilon^r} & \frac{\partial^2 S}{\partial \epsilon^i \partial \epsilon^r} \\ \frac{\partial^2 S}{\partial \epsilon^r \partial \epsilon^i} & \frac{\partial^2 S}{\partial \epsilon^i \partial \epsilon^i} \end{pmatrix} \\ &= \begin{pmatrix} \Re(\overline{\mathbf{F}}^\dagger \cdot \overline{\mathbf{F}}) + \gamma \overline{\mathbf{I}} & -\Im(\overline{\mathbf{F}}^\dagger \cdot \overline{\mathbf{F}}) \\ \Im(\overline{\mathbf{F}}^\dagger \cdot \overline{\mathbf{F}}) & \Re(\overline{\mathbf{F}}^\dagger \cdot \overline{\mathbf{F}}) + \gamma \overline{\mathbf{I}} \end{pmatrix}, \end{aligned} \quad (3.3)$$

where  $\epsilon^r$  and  $\epsilon^i$  are the real and imaginary parts of  $\epsilon$ ,  $\overline{\mathbf{I}}$  is the identity matrix, and  $\Re$  and  $\Im$  denote the real and imaginary parts of the following operand.  $\overline{\mathbf{F}}$  is the so-called Fréchet operator, which is defined as

$$\overline{\mathbf{F}} = \frac{\partial \Phi^{sca}}{\partial \epsilon}. \quad (3.4)$$

Its explicit form and implementation will be introduced in the next section.  $\overline{\mathbf{F}}^\dagger$  is the complex conjugate transpose of the  $\overline{\mathbf{F}}$ .

### 3.3 Fréchet Operator and the Distorted Born Iterative Method

The scattered fields  $\Phi^{sca}$  can be expressed as

$$\Phi^{sca} = \overline{\mathbf{G}}' \cdot \overline{\mathbf{O}} \cdot \Phi, \quad (3.5)$$

where  $\overline{\mathbf{G}}'$  is the Green's function for the background medium (see Equation (2.3) for the homogeneous background medium) and  $\Phi$  is the vector containing the total fields at each grid point. Note that the field points of  $\overline{\mathbf{G}}'$  are at receivers' locations. Substituting (3.5) into (3.4), we obtain

$$\overline{\mathbf{F}} = \overline{\mathbf{G}}' \cdot \left( \frac{\partial \overline{\mathbf{O}}}{\partial \epsilon} \cdot \Phi + \overline{\mathbf{O}} \cdot \frac{\partial \Phi}{\partial \epsilon} \right). \quad (3.6)$$

The second term in the above equation contains the higher order terms in  $\overline{\mathbf{O}}$ , and it can be neglected compared with the first term under the distorted Born approximation [33]. Therefore,

$$\overline{\mathbf{F}} \sim k_0^2 \overline{\mathbf{G}}' \cdot \overline{\mathcal{D}}(\Phi), \quad (3.7)$$

where  $\overline{\mathcal{D}}$  converts a vector into a square diagonal matrix and  $k_0$  is the free space wavenumber.

The Born iterative method assumes a constant background medium as the iteration proceeds. Therefore,  $\overline{\mathbf{G}}'$  remains unchanged throughout the iteration. On the contrary, the distorted Born iterative method utilizes the object profile from the last iteration as the background medium. Hence,  $\overline{\mathbf{G}}'$  has to be updated for each iteration. It can be inferred from Equation (3.7) that the convergence rate of BIM is first order, but that of DBIM is second order.

### 3.4 Implementation of the Algorithm

Because  $\overline{\mathbf{G}}'$  and  $\Phi$  must be updated for each iteration, CGFFT is invoked as the forward solver to solve for both quantities for transmitters and receivers. However, consider the reciprocity theorem,

$$\langle \mathbf{E}_2, \mathbf{J}_1 \rangle = \langle \mathbf{E}_1, \mathbf{J}_2 \rangle, \quad (3.8)$$

which states that the field resulting from  $\mathbf{J}_1$  measured by  $\mathbf{J}_2$  is the same as the field resulting from  $\mathbf{J}_2$  measured by  $\mathbf{J}_1$ . Therefore, if transmitters and receivers occupy the same positions, according to the reciprocity theorem, it is only necessary to calculate  $\Phi$ , and then, one can obtain  $\overline{\mathbf{G}}'$  immediately by multiplying  $\Phi$  by a constant.

To speed up CGFFT calculation, either  $\overline{\mathbf{G}}'$  or  $\Phi$  are stored. We use  $\Phi$  of the previous iteration as the initial guess, which is a good initial guess because the current object function is not substantially different from the previous one. Therefore, in the CGFFT procedure of finding  $\Phi$ , iteration number is kept within a fixed number. When the reconstruction approaches the optimum, CGFFT takes only one or two iterations to converge. Note that  $\Phi$  can be stored in a disk space or kept in memory for later use depending on whether the available computer memory store is large enough.

Once  $\Phi$  is calculated (and hence also  $\overline{\mathbf{G}}'$ ), the gradient and the Hessian can be found from Equations (3.2) and (3.3). Note that implementing the gradient or applying the Hessian to a vector involves several matrix-vector multiplies. Unfortunately, the explicit forms of these matrices do not suggest any special structure to speed up the calculation. We assume that there are  $N_T$  transmitters,  $N_R$  receivers and  $N$  unknown cells of permittivity to be found. Generally,  $\Phi^{sca}$  and  $\Phi_{meas}^{sca}$  are block vectors, which contain  $N_T$  blocks of  $N_R$ -element vectors. Similarly,  $\Phi$  has  $N_T$  blocks of  $N$ -element vectors. Also,  $\overline{\mathbf{F}}$  and  $\overline{\mathbf{F}}^\dagger$  are matrices of dimension  $N_T N_R \times N$  and  $N \times N_T N_R$ , respectively. Hence, the calculation of the gradient and the Hessian multiplying a vector requires  $O(N_T N_R N)$  operations. Intuitively, the available data points, namely the product of  $N_T$  and  $N_R$ , should be of the same order of  $N$  in order to obtain a good reconstruction. Therefore, the cost of these two matrix-vector multiplies is  $O(N^2)$ , which is computationally intensive as  $N$  becomes large.

An alternative to the above implementation is to use the back-propagation con-

cept. To understand this idea better, we rewrite (3.7) as

$$\bar{\mathbf{F}}^\dagger \sim k_0^2 \bar{\mathcal{D}}(\Phi)^\dagger \cdot \bar{\mathbf{G}}^\dagger. \quad (3.9)$$

Instead of finding the explicit form of  $\bar{\mathbf{G}}^\dagger$ , the operation of  $\bar{\mathbf{G}}^\dagger$  on a vector can be viewed as calculating the total field inside the object due to the “sources” located at the receivers. It is not necessary to invoke CGFFT repeatedly for each “source,” because by collecting the incident field from all the sources, CGFFT then solves the forward problem only once. It results in an  $O(N_i N \log_2 N)$  matrix-vector multiply, instead of original  $O(N N_R)$  operations, where  $N_i$  is the number of iterations to converge. Hence, the total cost of implementing  $\bar{\mathbf{F}}^\dagger$  on a vector is  $O(N_T N_i N \log_2 N)$ . If  $N_i$  is proportional to  $N^\alpha$ , in which  $\alpha < 0.5$ , then this implementation will prevail when  $N$  is large.

As to the implementation of  $\bar{\mathbf{F}}$  on a vector,  $\bar{\mathbf{G}}'$  can be implemented in  $O(N \log N)$  operations by repeatedly applying Huygens’ equivalence principle to calculate the scattered field (see NEPAL in the next chapter for more details). If  $\bar{\mathbf{G}}'$  has no analytic form and has to be found by numerical method (for example, under the inhomogeneous medium), it can be implemented by a forward solver (CGFFT) for fields inside the object and then followed by applying a homogeneous Green’s function for the scattered fields at receivers. Then the second step can be achieved by NEPAL as mentioned earlier. Therefore, the matrix-vector multiply can be achieved in  $O(N_T N_i N \log_2 N)$  as well.

At the current stage, we still use the direct method to find the gradient or the product of the Hessian on a vector, because the pre-factor of the complexity  $N_T N_i N \log_2 N$  is large, which has not justified its efficiency for the  $N$  we have tried. Therefore, the computational cost of the inverse scattering algorithm is  $N_o(C_1 N_T N_{i1} N \log_2 N + C_2 N_R N_{i2} N \log_2 N + C_3 N^2)$ , where  $N_o$  is the number of outer iterations,  $N_{i1}$  and  $N_{i2}$  are those of inner iterations and  $C_1$ ,  $C_2$  and  $C_3$  are some constants. The first two terms within the parentheses dominate the cost for now.

### 3.5 Numerical Results and Barcelona Experimental Data

As a gauge of the accuracy of the reconstruction, a relative residual error (RRE) at the  $j$ -th iteration can be defined as

$$RRE = \frac{\|\Phi_j^{scat} - \Phi_{meas}^{scat}\|}{\|\Phi_{meas}^{scat}\|}. \quad (3.10)$$

In Figure 3.2(a), we show the real part and the imaginary part of the original dielectric profile. By using a full-angle imaging setup, there are 8 transmitters and 8 receivers occupying locations which are evenly spaced at the circle  $1.6\lambda_0$  in radius. The reconstruction area is of size  $1\lambda_0 \times 1\lambda_0$  divided into a  $13 \times 13$  mesh. Figure 3.2(b) shows the reconstructed dielectric profile after 19 iterations. The difference between the simulated scattering data and the synthetic achieves about  $10^{-3}$  relative residual error. A good reconstruction is observed.

The second example is to reconstruct a dielectric circular cylinder with  $\epsilon_r = 2.0 + i0.5$ . It has the size of the reconstruction area as in Figure 3.2, but a different  $17 \times 17$  grid. Seventeen transmitters and 17 receivers are used, and the observation distance is  $1.0\lambda_0$ . Figure 3.3 shows the profiles and the images of both the real and imaginary parts of the relative dielectric constant at iteration 22 with  $RRE = 3.85 \times 10^{-3}$ . The numerical values of  $\epsilon_r$  are reconstructed accurately.

Note that no *a priori* information is used in these reconstructions. An initial guess of a background medium is assumed. Because high-frequency components are missing in the scattered fields, the reconstructions exhibit ripples near the discontinuity of the object function. This Gibbs' phenomenon [31] can be seen clearly in Figure 3.4, in which a dielectric circular well is to be reconstructed.

The regularization parameter plays an important role in the inverse scattering algorithm. A too-strong regularization parameter will remove too much useful information and decrease the spatial resolution, while a too-weak regularization parameter renders the system susceptible to noise error and numerical error and

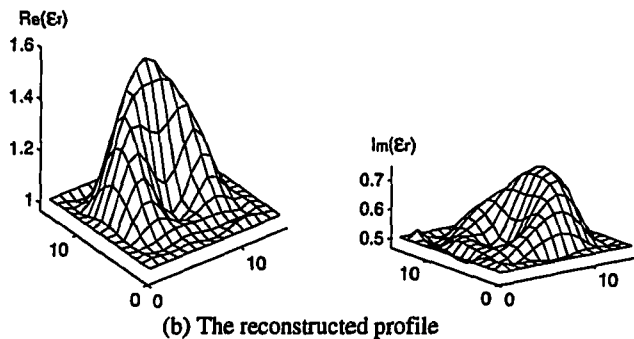
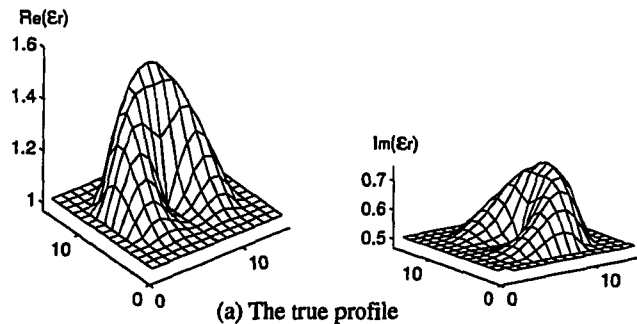
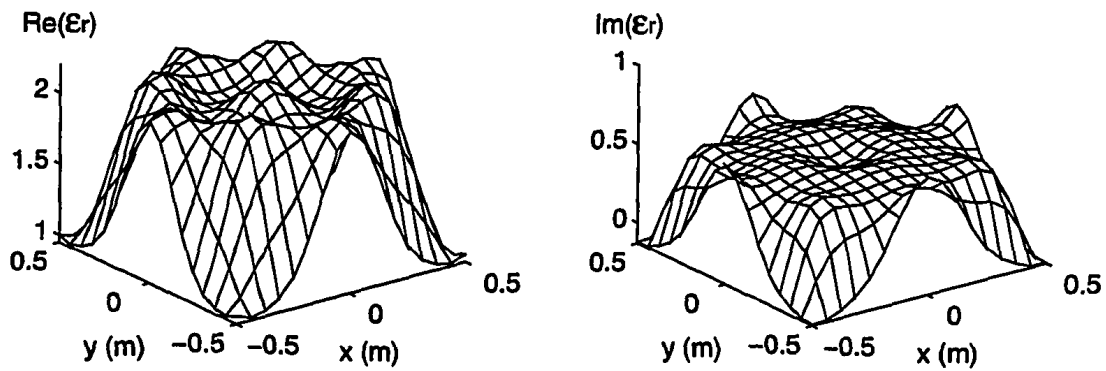
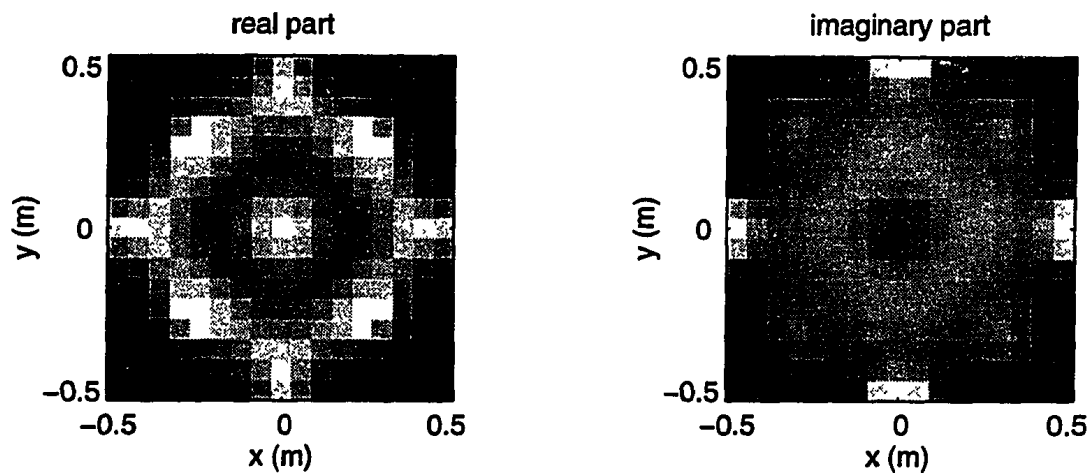


**Figure 3.2.** The true and reconstructed dielectric profiles for an inhomogeneous object. The reconstruction area is  $1\lambda_0 \times 1\lambda_0$  divided into a  $13 \times 13$  mesh. Eight transmitters and 8 receivers are evenly spaced at the circle  $1.6\lambda_0$  in radius.

produces unphysical solutions. There are various methods to find a suitable regularization parameter [12], [25], [26]. Nonetheless, it always entails significant extra computational cost to find a suitable regularization parameter. We adopt a varying-parameter scheme: in the beginning, we choose a regularization parameter large enough to overshadow those small eigenvalues that correspond to high-frequency



(a) reconstructed profiles



(b) reconstructed images

**Figure 3.3** The reconstructed profiles and images of a dielectric circular cylinder with  $\epsilon_r = 2.0 + i0.5$ . The reconstruction area is  $1\lambda_0 \times 1\lambda_0$  divided into a  $17 \times 17$  mesh. Seventeen transmitters and 17 receivers are evenly spaced at the circle  $1.0\lambda_0$  in radius.

and oscillatory components; as the iteration proceeds, the regularization parameter is reduced to enlarge the useful solution space and to include higher frequency components gradually.

The original structure for Figure 3.4 is simulating the human muscle ( $\epsilon_r \sim$

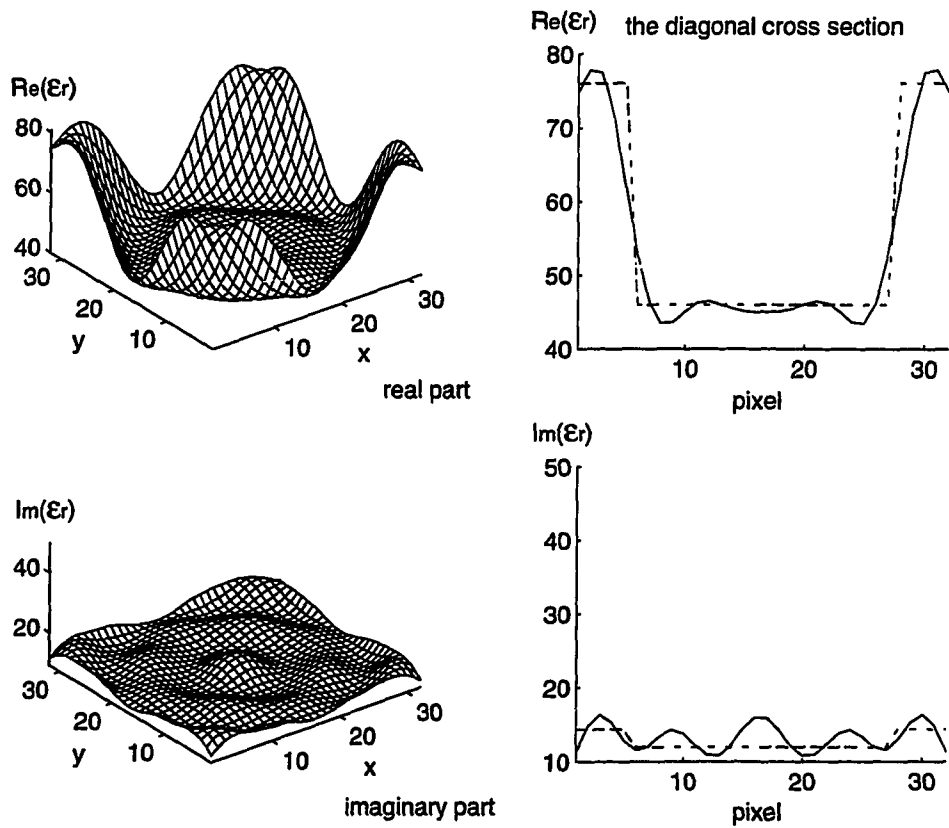


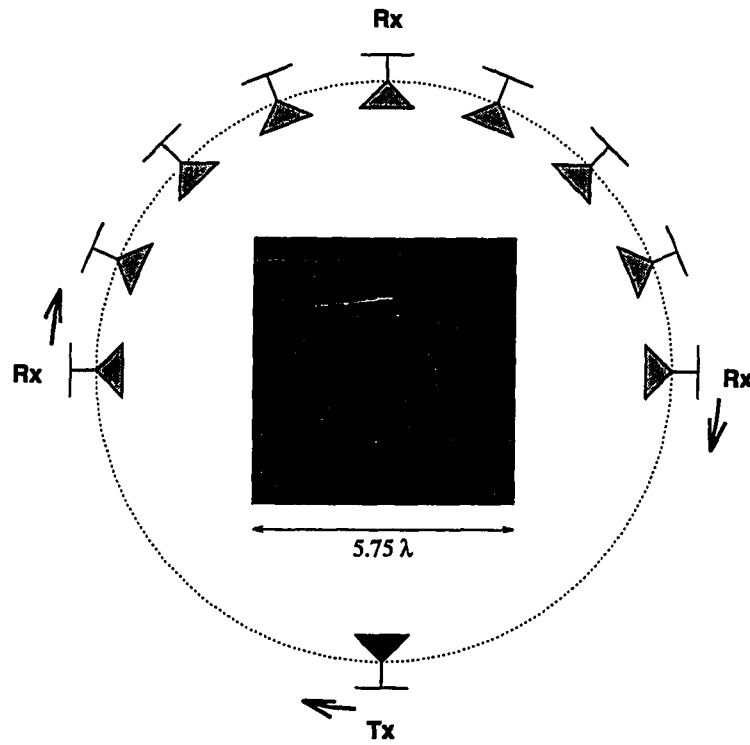
**Figure 3.4.** The reconstructed dielectric profiles and the diagonal cross section of a dielectric circular well with  $\epsilon_r = 46.0 + i12.0$  immersed in water ( $\epsilon_r = 76.0 + i14.4$ ). The reconstruction area is  $1.75\lambda_w \times 1.75\lambda_w$  divided into a  $32 \times 32$  mesh. Thirty-two transmitters and 32 receivers are evenly spaced at the circle  $2.63\lambda_w$  in radius.

$46.0 + i12.0$ ) immersed in water ( $\epsilon_r \sim 76.0 + i14.4$ ). The reconstruction area is about  $1.75\lambda_w$  on each side, where  $\lambda_w$  is the water wavelength. The area is gridded into  $32 \times 32$  cells, and there are 32 transmitters and 32 receivers lying on a circle  $2.63\lambda_w$  away from the origin. Figure 3.4 shows the reconstructed profiles and the diagonal cross sections. The dashed lines in the diagonal cross section figures denote the true

object profile and the solid line that of the reconstruction. A good agreement is observed for the real part, yet there is obvious discrepancy for the imaginary part, because the amplitude of the ripples is strong enough to smear the boundary of the wells.

Next, we apply the inverse scattering algorithm to real experimental data [30]. Figure 3.5 is the diagram of the experimental setup. The experimental setup in Barcelona in Spain is based on a cylindrical array of 64 antennas equispaced on a circle 25 cm in diameter. The basic measurement consists of using an antenna of the array as the transmitter, and the scattered fields are received at the remaining elements located at the half circle diametrically opposite to the transmitter. This procedure is repeated by sequentially transmitting with each of the antennas to complete one turn. The main parts of this system are the cylindrical array of 64 antennas immersed in water using a plastic cylindrical container; the operating frequency is 2.33 GHz as a result of the compromise among spatial resolution, tolerable attenuation and the receiver sensibility.

The size of the reconstructed area is  $5.75\lambda \times 5.75\lambda$ , and it is divided into a  $23 \times 23$  mesh. The measurement data we use is collected by only 17 receivers for 32 transmitters (more measurement data have been used, but the reconstructions do not improve). Figure 3.6 shows the images of the complex permittivity in the real and imaginary parts for the first iteration. Note that the images shown are obtained by interpolating the original images. The contrast is not obvious although there are two dark points vaguely indicating the geometrical shape and location of two bones. As the iteration proceeds, the contrast of the image becomes more obvious, and we can differentiate the composition in the biological structure. Figures 3.7 and 3.8 represent the images for the 5th and 10th iterations, respectively. We stop the algorithm at the 15th iteration, because the RRE starts stagnating. More iterations only fine-tune the reconstruction so that the RRE decreases very slowly. In other words, the first few iterations have already determined the general structure of the unknown object. It takes about 70 minutes on a SPARC 2 workstation (throughput  $\sim 5.0$  MFLOPS) to obtain these images. Shown in Figure 3.9 are the



Frequency = 2.33 GHz

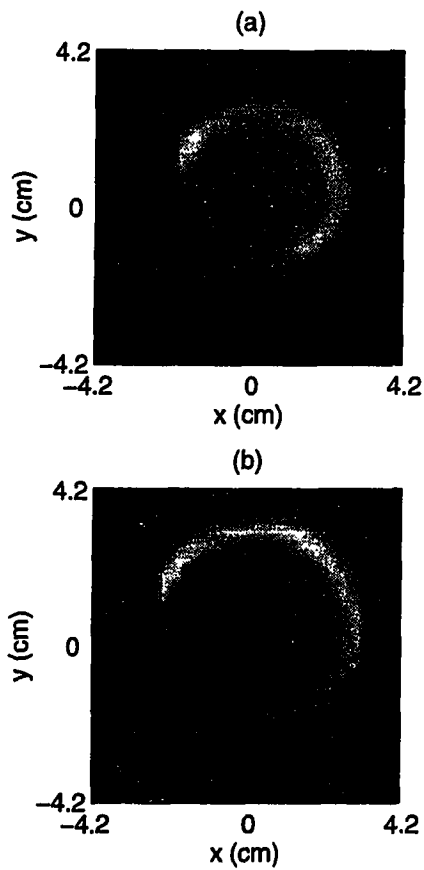
64 Transmitters

Background Medium : Water  
 $(\epsilon_r = 77.3 + i 8.66)$

33 Receivers

**Figure 3.5.** The schematic experimental setup in Barcelona.

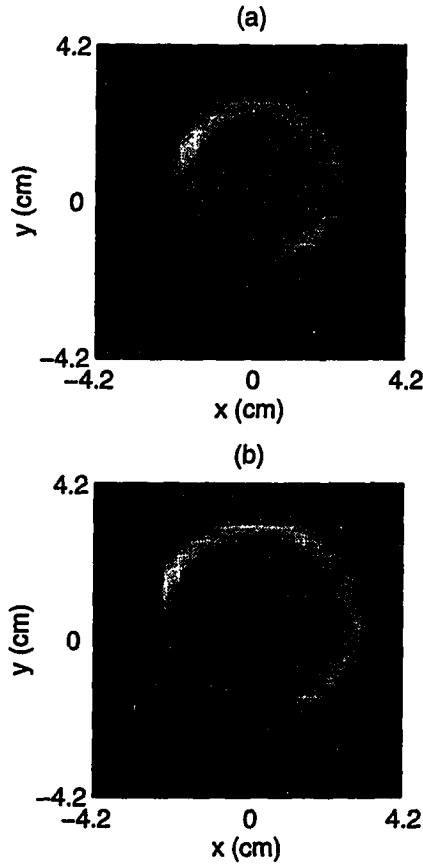
final reconstructed images along with the diagonal cross section of the reconstructed profiles. As observed in the figure, the numerical value of the dielectric constant is not in the reasonable range: there are two confusing high spikes that correspond to the bright rings around the object. The overshoots and undershoots may be explained by the Gibbs' phenomenon.



**Figure 3.6.** The 1st iteration reconstructed images of a human arm from the Barcelona experimental data: (a) real part of  $\epsilon_r$ , (b) imaginary part of  $\epsilon_r$ .

### 3.6 Frequency-Hopping Scheme

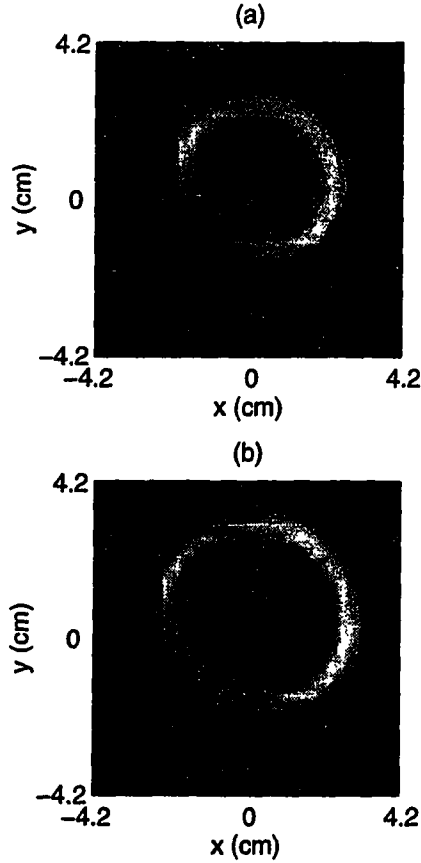
As the reconstructed area grows and the contrast of the profile becomes more pronounced, without any *a priori* information, it is difficult to obtain a good image except for the background medium. One way to circumvent this difficulty is to use the frequency-hopping scheme: start with the lowest frequency and obtain the image, which will be used as an initial guess for the next higher frequency. In this fashion, after several frequency “hops,” the final image under the highest frequency is acquired. This scheme is motivated by having observed a better performance of



**Figure 3.7.** The 5th iteration reconstructed images of a human arm from the Barcelona experimental data: (a) real part of  $\epsilon_r$  (b) imaginary part of  $\epsilon_r$ .

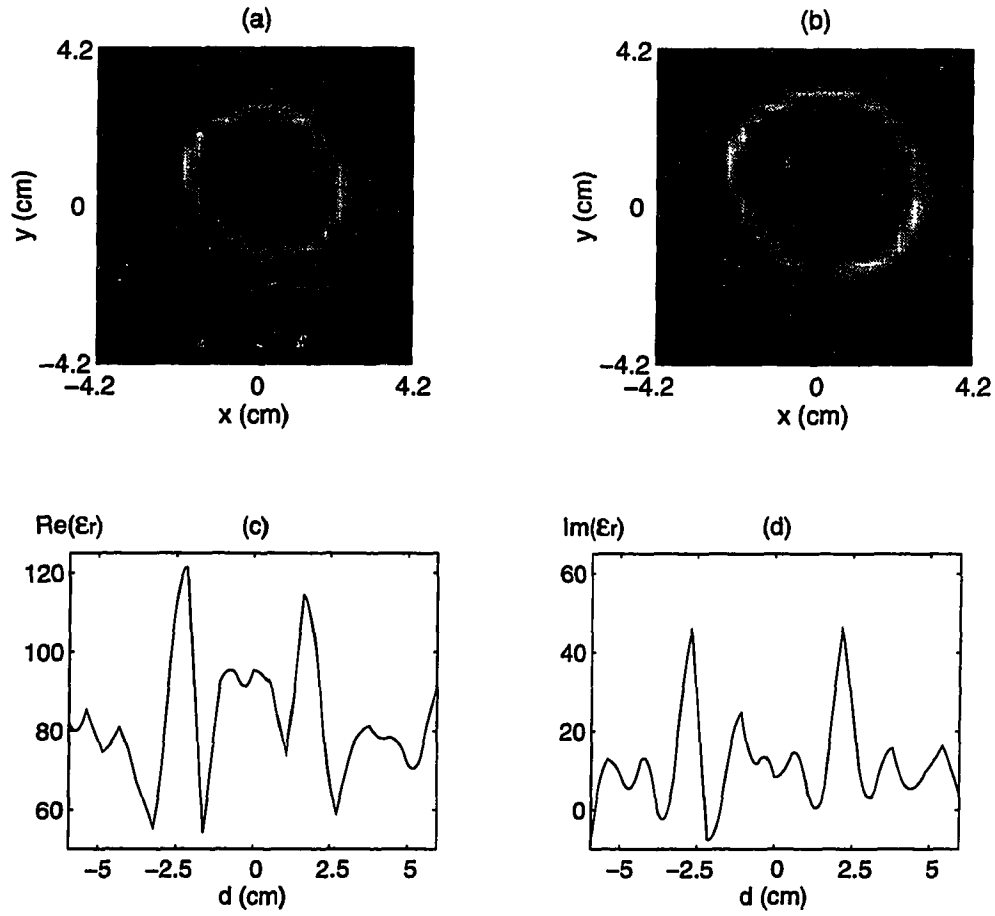
reconstructions in the time domain when pulses are used as a probing signal, where a band of frequencies automatically provides more information on the structure. We apply this scheme to some cases, and it does show the superiority over the single-frequency method.

Figure 3.10 shows a biological model that contains fat of  $\epsilon_r = 5.55 + i0.67$ , muscle of  $\epsilon_r = 45.0 + i13.0$  and bone of  $\epsilon_r = 8.35 + i1.32$  at 3 GHz [32]. It is immersed in water of  $\epsilon_r = 73.18 + i7.94$ . The reconstruction area is  $5.56\lambda_w \times 5.56\lambda_w$  divided into  $32 \times 32$  cells. There are 32 transmitters and 32 receivers located on the circle of



**Figure 3.8.** The 10th iteration reconstructed images of a human arm from the Barcelona experimental data: (a) real part of  $\epsilon_r$ , (b) imaginary part of  $\epsilon_r$ .

radius  $4.27\lambda_w$ . We adopt 1 GHz, 2 GHz and 3 GHz as the probing frequencies. The medium dispersion has been taken into account by assigning different  $\epsilon_r$  to media for different frequencies according to the tabulated data in [32]. Shown in Figure 3.11 are the images for three frequencies. As expected, the higher the frequency, the higher the resolution. But the lower the frequency, the less the nonlinearity in the inverse problem so that one obtains the better reconstruction, which in turn is a good initial guess for the next higher frequency inversion. In Figure 3.12, the diagonal cross sections for both the true profile (dashed line) and the reconstructed profile (solid line) are plotted. High fidelity of the reconstruction has been observed. The simulation takes about 11.5 minutes on a Cray-YMP vectorized computer.



**Figure 3.9.** The reconstructed images of Barcelona experimental data and the diagonal cross section profiles at iteration 15 with the  $RRE = 0.1853$ . The reconstruction area is  $5.75\lambda_w \times 5.75\lambda_w$  divided into a  $23 \times 23$  mesh. Thirty-two transmitters and 17 receivers are used. The measurement distance is  $8.56\lambda_w$  from the center. (a) Image of  $\Re(\epsilon_r)$ ; (b) image of  $\Im(\epsilon_r)$ . (c) Diagonal cross section profile of  $\Re(\epsilon_r)$ ; (d) diagonal cross section profile of  $\Im(\epsilon_r)$ .

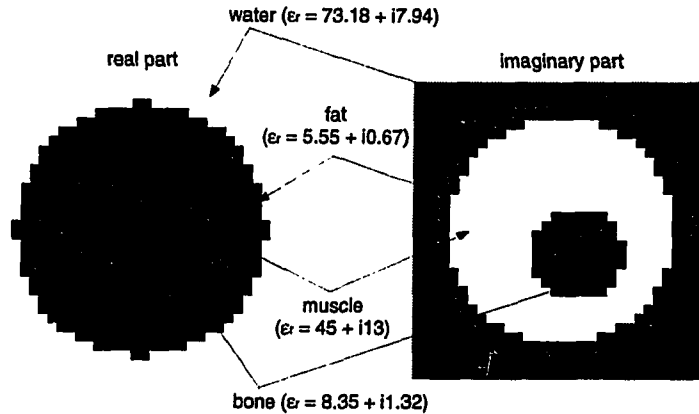


**Figure 3.10.** A biological model with fat of  $\epsilon_r = 5.55 + i0.67$ , muscle of  $\epsilon_r = 45.0 + i13.0$  and bone of  $\epsilon_r = 8.35 + i1.32$  at 3 GHz immersed in the water of  $\epsilon_r = 73.18 + i7.94$ .

As a comparison, we include the images directly reconstructed by a single frequency of 3 GHz and its diagonal cross section in Figure 3.13. The plot obviously shows that the single-frequency scheme fails to reconstruct the object and produces some unreasonable high spikes in the profiles, as we have seen in the Barcelona experimental data.

The final example is a model consisting of some circular cylinders, each of which represents fat, muscle and bone, respectively, and which have different dielectric constants at different frequencies [32]. We utilize four frequencies, 0.5, 0.9, 1.65 and 3 GHz. The size of the reconstructed area is 12 cm by 12 cm ( $10.2\lambda_w \times 10.2\lambda_w$ ) divided into  $64 \times 64$  cells. Forty-eight transmitters and 48 receivers are utilized. The total computational time is about 1 hour on a Cray-YMP machine. We observe a good reconstruction for the real part of the cross section profile in Figure 3.14.

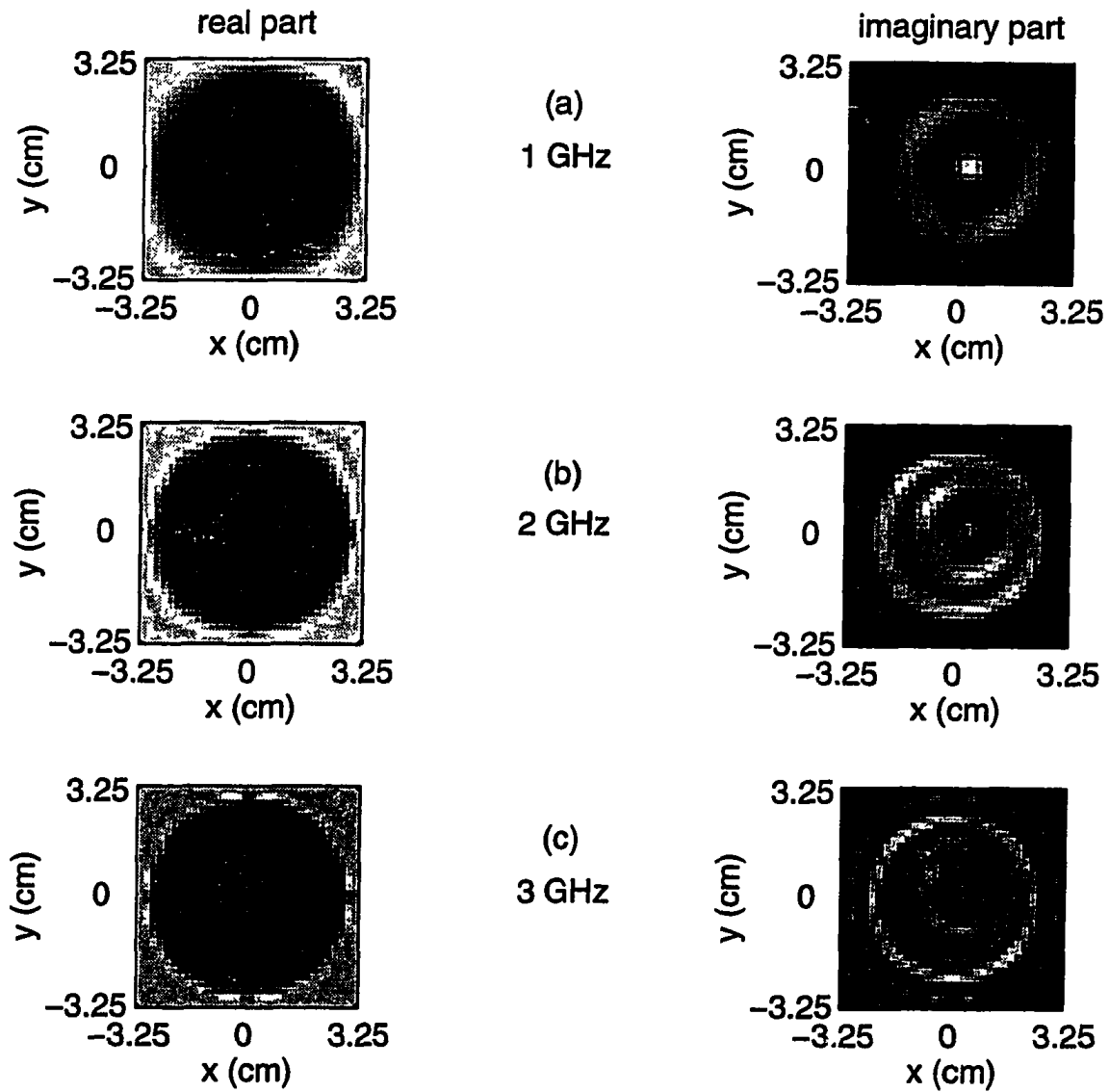


**Figure 3.11.** The reconstructed images of the Figure 3.10 model for 1 GHz, 2 GHz and 3 GHz by the frequency-hopping scheme. The reconstruction area is  $5.56\lambda_w \times 5.56\lambda_w$  divided into  $32 \times 32$  cells. There are 32 transmitters and 32 receivers located on the circle of radius  $4.27\lambda_w$ .

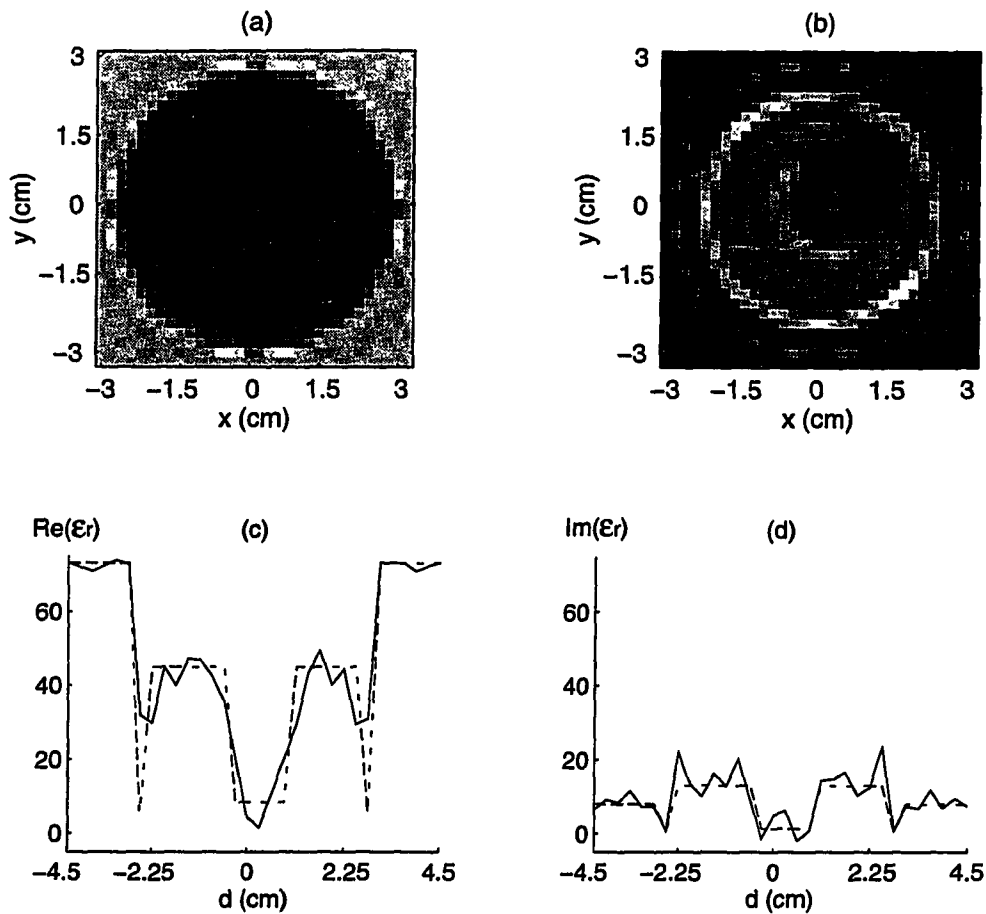


**Figure 3.12.** The reconstructed images and the diagonal cross section for the true profile (dashed line) and the reconstructed profile (solid line) at 3 GHz by the frequency-hopping method. (a) Image of  $\text{Re}(\epsilon_r)$ ; (b) image of  $\text{Im}(\epsilon_r)$ . (c) Diagonal cross section profile of  $\text{Re}(\epsilon_r)$ ; (d) diagonal cross section profile of  $\text{Im}(\epsilon_r)$ .

But a poor and misleading image is shown for the imaginary part, especially for the parts embedded deep in the object. This phenomenon can be explained by the fact that microwaves in this frequency range attenuate rapidly in biological media. Therefore, it is difficult for microwaves to provide enough information about the inner structure of the unknown object.

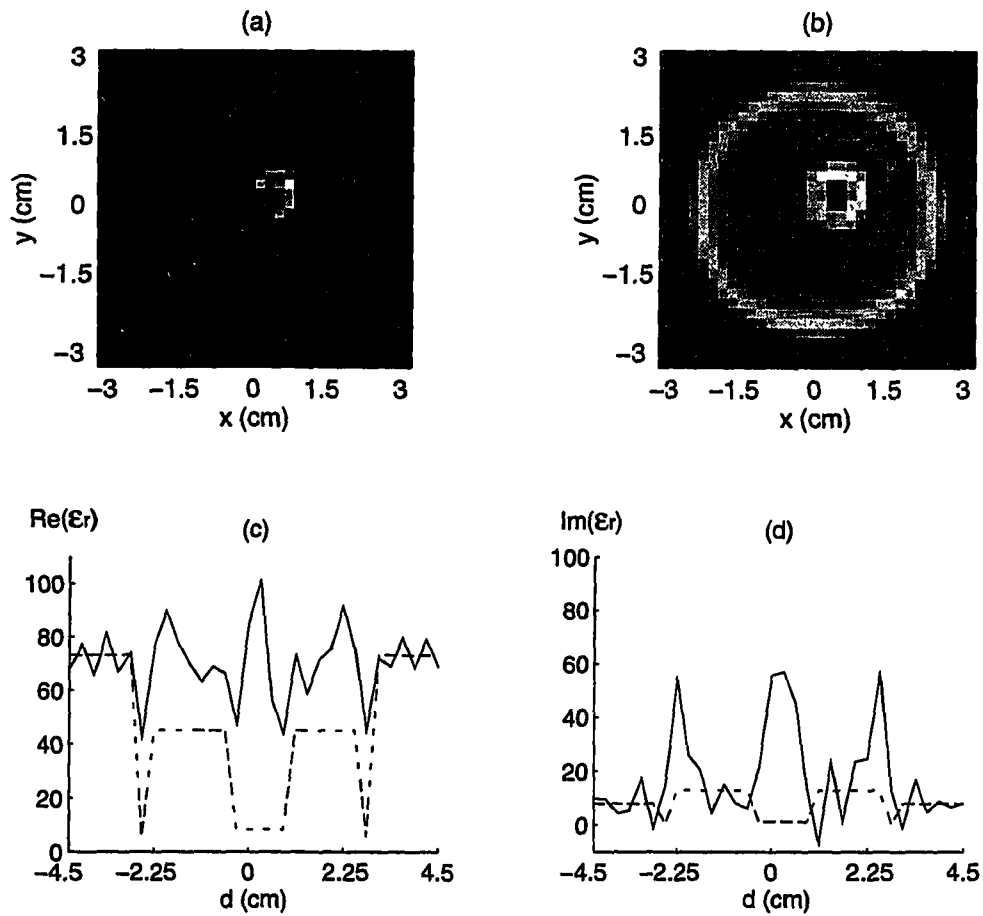


**Figure 3.13.** The reconstructed images and the diagonal cross section for the true profile (dashed line) and the reconstructed profile (solid line) at 3 GHz by the single-frequency method . (a) Image of  $\Re(\epsilon_r)$ ; (b) image of  $\Im m(\epsilon_r)$ . (c) Diagonal cross section profile of  $\Re(\epsilon_r)$ ; (d) diagonal cross section profile of  $\Im m(\epsilon_r)$ .

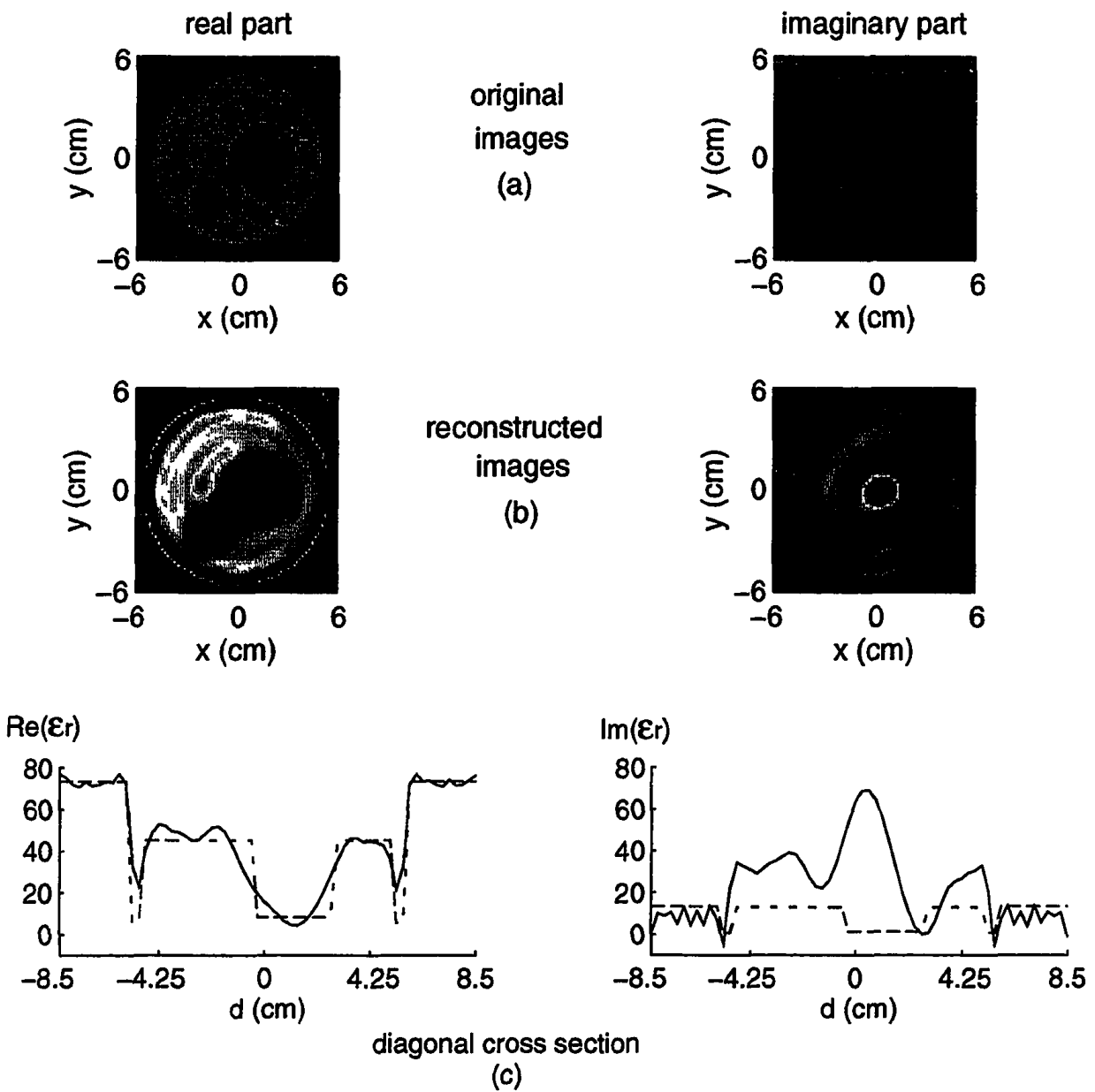


**Figure 3.14.** The original and reconstructed images and the diagonal cross section for the true profile (dashed line) and the reconstructed profile (solid line) at 3 GHz by the frequency-hopping method. The operating frequencies are 0.5, 0.9, 1.65 and 3 GHz. The reconstructed area is  $10.2\lambda_w \times 10.2\lambda_w$  divided into  $64 \times 64$  cells. Forty-eight transmitters and 48 receivers are used.

### 3.7 Conclusions

An efficient electromagnetic inverse scattering algorithm in two dimensions for TM polarization has been developed. Combining CGFFT and DBIM gives rise to an efficient algorithm with operation counts  $\sim N_o(C_1N_TN_{i1}N\log_2N + C_2N_RN_{i2}N\log_2N + C_3N^2)$ , where  $N_o$  is the outer iteration number,  $N_{i1}$  and  $N_{i2}$  inner iteration numbers,  $N_T$  and  $N_R$  the number of transmitters and receivers, respectively,  $N$  the number of cells and  $C_1$ ,  $C_2$  and  $C_3$  are the fixed constants.

The algorithm combined with the frequency-hopping scheme is capable of reconstructing the large inhomogeneous bodies of high contrasts with high fidelity. The algorithm has been tested on real experimental data, and the reconstructed images show the inner structure of the body.

Not only is the real part of the dielectric constant reconstructed, the imaginary part is also retrieved simultaneously. As the simulations show, the latter usually cannot be reconstructed well when the body is large due to the domination of the real part. Moreover, *a priori* information is needed to deliver better images or different formulations concentrating on the lossy term are required to provide better image quality of the imaginary part.

### 3.8 References

- [1] D. Colton, "The inverse electromagnetic scattering problem for a perfectly conducting cylinder," *IEEE Trans. Antennas Propag.*, vol. 29, no. 2, pp. 364-368, 1981.
- [2] C.-C. Chiu and Y.-W. Kiang, "Inverse scattering of a buried conducting cylinder," *Inverse Probl.*, vol. 7, pp. 187-202, 1991.
- [3] C.-C. Chiu and Y.-W. Kiang, "Microwave imaging of multiple conducting cylinders," *IEEE Trans. Antennas Propag.*, vol. 40, no. 8, pp. 933-941, 1992.
- [4] P. Maioni, L. Misici, and F. Zirilli, "An inverse problem for the three dimensional vector Helmholtz equation for a perfectly conducting obstacle," *Computers Math. Applic.*, vol. 22, no. 4, pp. 137-146, 1991.

- [5] W. C. Chew and G. P. Otto, "Microwave imaging of multiple metallic cylinders using local shape functions," *Proc. IEEE-APS Int. Symp.*, Chicago, Illinois, pp. 1716-1719, 1992.
- [6] W. C. Chew and G. P. Otto, "Microwave imaging of multiple conducting cylinders using local shape functions," *IEEE Microw. Guided Wave Lett.*, vol. 2, no. 7, pp. 284-286, 1992.
- [7] G. P. Otto and W. C. Chew, "Microwave inverse scattering-local shape function imaging for improved resolution of strong scatterers," *IEEE Trans. Microwave Theory Tech.*, vol. 42, no. 1, pp. 137-141, 1994.
- [8] W. H. Weedon and W. C. Chew, "Time-domain inverse scattering using local shape function (LSF) method," *J. Inverse Problems*, vol. 9, pp. 551-564, 1993.
- [9] Y. M. Wang and W. C. Chew, "An inverse solution of two-dimensional electromagnetic inverse scattering problem," *Int. J. Imag. Syst. Tech.*, vol. 1, no. 1, pp. 100-108, 1989.
- [10] W. C. Chew and Y. M. Wang, "Reconstruction of two-dimensional permittivity distribution using the distorted Born iterative method," *IEEE Trans. Med. Imaging*, vol. 9, no. 2, pp. 218-225, 1990.
- [11] J-Ch. Bolomey and Ch. Pichot, "Microwave tomography: from theory to practical imaging systems," *Int. J. Imag. Syst. Tech.*, vol. 2, no. 2, pp. 144-156, 1990.
- [12] N. Joachimowicz, Ch. Pichot, and J-P. Hugonin, "Inverse scattering: An iterative numerical method for electromagnetic imaging," *IEEE Trans. Antennas Propag.*, vol. 39, no. 12, pp. 1742-1752, 1991.
- [13] M. Moghaddam and W. C. Chew, "Comparison of the Born iterative method and Tarantola's method for an electromagnetic time-domain inverse problem," *Int. J. Imag. Syst. Tech.*, vol. 3, pp. 318-333, 1991.
- [14] M. Moghaddam and W. C. Chew, "Nonlinear two-dimensional velocity profile inversion using time domain data," *IEEE Trans. Geosci. Remote Sens.*, vol. 30, no. 1, pp. 147-156, 1992.
- [15] G. P. Otto and W. C. Chew, "Inverse scattering of  $H_z$  waves using local shape function imaging: a T-matrix formulation," *Int. J. Imaging Sys. Tech.*, vol. 5, pp. 22-27, 1994.

- [16] J.-H. Lin, C. C. Lu, Y. M. Wang, W. C. Chew, J. J. Mallorqui, A. Broquetas, Ch. Pichot, and J.-Ch. Bolomey, "Processing microwave experimental data with the distorted Born iterative method of nonlinear inverse scattering," *IEEE Antennas and Propagation Society International Symposium Digest*, pp. 500-503, 1993.
- [17] J.-Ch. Bolomey, Ch. Durix, and D. Lesselier, "Determination of conductivity profiles by time-domain reflectometry," *IEEE Trans. Antennas Propag.*, vol. 27, pp. 244-248, 1979.
- [18] Q.-H. Liu, "Nonlinear inversion of electrode-type resistivity measurements," *IEEE Trans. Geosci. Remote Sens.*, vol. 32, no. 3, pp. 499-507, 1994.
- [19] W. C. Chew and Q.-H. Liu, "Inversion of induction tool measurements using the distorted Born iterative method and CG-FFHT," *IEEE Trans. Geosci. Remote Sens.*, vol. 32, no. 4, pp. 878-884, 1994.
- [20] P. F. Polatin, K. Sarabandi, and F. T. Ulaby, "An iterative inversion algorithm with application to the polarimetric radar response of vegetation canopies," *IEEE Trans. Geosci. Remote Sens.*, vol. 32, no. 1, pp. 62-71, 1994.
- [21] A. N. Tikhonov and V. Y. Arsenin, *Solutions of Ill-posed Problems*. Washington, DC: V. H. Winston & Sons, 1977.
- [22] G. Wahba, "Practical approximate solutions to linear operator equations when the data are noisy," *SIAM J. Numer. Anal.*, vol. 14, no. 4, pp. 651-667, 1977.
- [23] P. Craven and G. Wahba, "Smoothing noisy data with spline functions," *Numerische Mathematik*, vol. 31, pp. 377-403, 1979.
- [24] T. K. Sarkar, D. D. Weiner, and V. K. Jain, "Some mathematical considerations in dealing with the inverse problem," *IEEE Trans. Antennas Propag.*, vol. 29, no. 2, pp. 373-379, 1981.
- [25] D. Girard, "Practical optimal regularization of large linear systems," *Mathematical Modelling and Numerical Analysis*, vol. 20, no. 1, pp. 75-87, 1986.
- [26] Y. M. Qin and I. R. Ciric, "Method of selecting the regularization parameter for microwave imaging," *Electronics Letters*, vol. 30, no. 24, pp. 2028-2029, 1994.
- [27] A. J. Devaney, "A filtered backpropagation algorithm for diffraction tomography," *Ultrasonic Imaging*, vol. 4, pp. 336-360, 1982.
- [28] A. J. Devaney, "Reconstructive tomography with diffracting wavefields," *Inverse Problems*, vol. 2, pp. 161-183, 1986.

- [29] A. J. Devaney, "The limited-view problem in diffraction tomography," *Inverse Problems*, vol. 5, pp. 501-521, 1989.
- [30] A. Broquetas, J. Romeu, J. M. Rius, A. R. Elias-Fuste, A. Cardama, and L. Jofre, "Cylindrical geometry: A further step in active microwave tomography," *IEEE Trans. Microwave Theory Tech.*, vol. 39, no. 5, pp. 836-844, 1991.
- [31] A. Papoulis, *The Fourier Integral and Its Applications*. New York: McGraw-Hill, 1962.
- [32] M. A. Stuchly and S. S. Stuchly, "Dielectric properties of biological substances - Tabulated," *J. Microwave Power*, vol. 15, pp. 19-26, 1980.
- [33] W. C. Chew, *Waves and Fields in Inhomogeneous Media*. New York: Van Nostrand Reinhold, 1990.

**CHAPTER 4**  
**MATRIX-VECTOR MULTIPLY BY**  
**NESTED EQUIVALENCE PRINCIPLE ALGORITHM**

**4.1 Introduction**

As mentioned in Chapter 2, solving the matrix equation iteratively has gained much attention because matrix storage is not required and for each iteration only a few matrix-vector multiplies are performed. So, if the convergence rate is reasonably fast, the iterative approach is an efficient method to solve large problems. As a result, conjugate gradient (CG) type algorithms are popular.

Directly implementing the matrix-vector multiply requires  $O(N^2)$  operations, where  $N$  is the number of unknowns. This is still computationally intensive. In most electromagnetic scattering problems, the kernel operator (for example, the Green's function in a linear, isotropic and homogeneous medium) possesses the convolution property because it obeys translational invariance. Exploiting the convolution feature of the matrix equation, we can use the fast Fourier transform (FFT) to speed up the matrix-vector multiply. The complexity of this method is  $O(N \log N)$ . This is the very reason why the conjugate gradient method with FFT (CGFFT) has been widely used in various applications [1]-[9].

However, in some cases in which the field points and the source points are not in the same region (for example, the far field calculation given the sources in a finite region), the FFT method becomes inefficient because a much larger area than the source region has to be uniformly gridded, and otherwise unnecessary zeros have to be assigned to the gridded free space.

Another complication is that fields inside an inhomogeneous body may change rapidly in some subregions, so a nonuniform grid is more efficient in required memory

storage and computational time. However, FFT can be applied only in a regular grid, whereas an excessively fine grid must be imposed on the whole region to accommodate the rapidly varying fields in a small subregion.

The nested equivalence principle algorithm (NEPAL) that we developed recently [10]-[13] can overcome the drawbacks of using FFT and is an  $O(N \log N)$  algorithm. The basic idea is to apply Huygens' equivalence principle repeatedly. Eventually, the field at each point can be evaluated from a small number of boundary sources instead of from all of the original sources. Figure 4.1 shows that the original scatterer consisting of  $N_A$  subscatterers is equivalent to the  $N_B$  subscatterers on the boundary in the sense of that the scattered fields outside the scatterer are the same for both configurations. Because  $N_B$  is much smaller than  $N_A$  when  $N_A$  is large, the second configuration is more efficient in calculating  $\phi_{sca}(\mathbf{r})$  as the scatterer size grows.

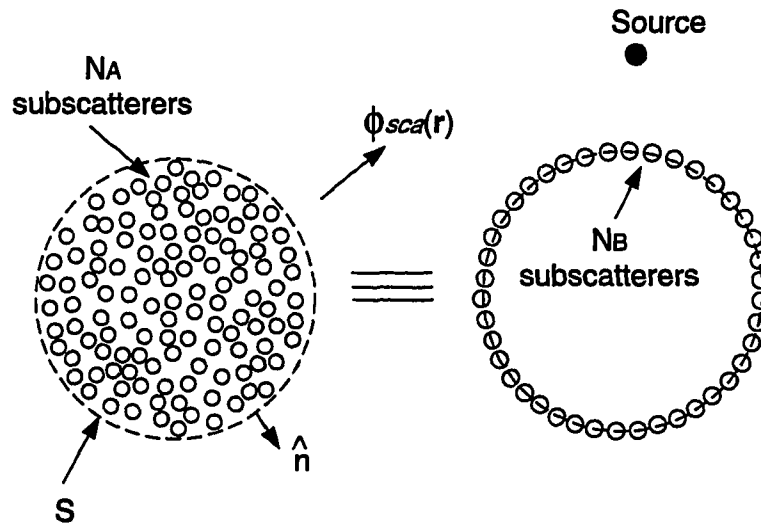


**Figure 4.1.** Use of Huygens' equivalence principle to replace the volume sources inside the scatterer with surface sources on the boundary to calculate the scattered field more efficiently.

The way NEPAL works can be described as follows. The scatterer is appropriately divided into many small groups, and then, using Huygens' equivalence principle, the sources in each small group can be replaced with the surface sources on the boundary. Next, we group four small groups as a subgroup, and again replace sources inside the subgroup with the surface sources on the boundary of each subgroup. Repeatedly nesting the subgroups within larger subgroups, we eventually obtain the four largest groups with surface sources representing the effects produced by those original sources within the groups. Therefore, in order to find the field outside the source region, we need only to calculate the contributions directly from the surface sources instead of from each original source.

Furthermore, to find the field at some specific point inside the source region, the incoming equivalent surface sources must be found on each group for each level. By identifying the group where the point belongs, and again, using Huygens' equivalence principle, we can replace those outside sources external to the group with surface sources on the group. By repeated nesting, all of the other groups in different levels are reduced to the smallest group which contains the point. Therefore, the contributions from many outside sources of this smallest group are accounted for by the surface sources lying around it.

The complexity of this algorithm is  $O(N \log N)$ . Additional techniques can be utilized to speed up the surface source calculation. The fast multipole method (FMM) [14]-[18] has recently become a powerful technique to implement the matrix-vector multiply required in iterative methods, which are used to solve surface integral equations. In view of the efficiency of calculating the interaction among surface sources by FMM, incorporating FMM in NEPAL can expedite the matrix-vector multiply in  $O(N)$  operations.

## 4.2 Relationship between Surface Sources and Volume Sources

In Equation (2.1), the scattered field after discretization can generally be ex-

pressed as

$$\phi_{sca}(\mathbf{r}) = \sum_{n=1}^{N_A} \psi^t(k_0, \mathbf{r}_n) \cdot \mathbf{a}_n, \quad (4.1)$$

where  $\mathbf{r}_n = \mathbf{r} - \mathbf{r}'_n$ ,  $\mathbf{r}'_n$  is the location of the  $n$ -th subscatterer and  $\psi^t(k_0, \mathbf{r}_n)$  is a row vector containing cylindrical harmonics. In two-dimensional problems,  $\psi^t(k_0, \mathbf{r}_n)$  has three elements, -1st, 0th and 1st harmonics, which correspond to the dipole and monopole radiations. The column vector  $\mathbf{a}_n$  contains the amplitudes of the harmonic expansions.  $N_A$  is the number of grids inside the scatterer.

The Huygens' equivalence principle states that the scattered field from a scatterer can be replaced by the field radiated from equivalent sources on a surface  $S$  that encloses the scatterer. Mathematically, it is

$$\phi_{sca}(\mathbf{r}) = \oint_S dS' \hat{n}' \cdot [\phi(\mathbf{r}') \nabla' g_b(\mathbf{r} - \mathbf{r}') - g_b(\mathbf{r} - \mathbf{r}') \nabla' \phi(\mathbf{r}')], \quad (4.2)$$

where  $g_b(\mathbf{r} - \mathbf{r}')$  is the Green's function of the background medium and  $\phi(\mathbf{r}')$  represents the total field on the surface  $S$  acting as surface sources.  $\hat{n}'$  is the outward normal to the surface  $S$ . Note that the first term in the bracket functions as dipole radiation, while the second term plays the role of monopoles.

The above equation can be discretized as

$$\phi_{sca}(\mathbf{r}) = \sum_{m=1}^{N_B} \psi^t(k_0, \mathbf{r}_m) \cdot \mathbf{b}_m, \quad (4.3)$$

where  $\mathbf{r}_m = \mathbf{r} - \mathbf{r}'_m$ ,  $\mathbf{r}'_m$  is the location of the  $m$ -th surface source, and  $\mathbf{b}_m$  depends on  $\phi(\mathbf{r}'_m)$  and  $\hat{n}' \cdot \nabla' \phi(\mathbf{r}'_m)$ . Because  $\phi(\mathbf{r}'_m)$  is a linear function of  $\mathbf{a}_n$  in (4.1), there should exist a linear relationship between  $\mathbf{a}_n$  and  $\mathbf{b}_m$ . It can be characterized by

$$\mathbf{b}_m = \sum_n \bar{\mathbf{h}}_{mn} \cdot \mathbf{a}_n, \quad (4.4)$$

where  $\bar{\mathbf{h}}_{mn}$  is a  $3 \times 3$  matrix that calculates the contribution to  $\mathbf{b}_m$  from  $\mathbf{a}_n$ .

The explicit form of  $\bar{\mathbf{h}}_{mn}$  can be derived as follows. The discretized version of (4.2) in two dimensions can be expressed as

$$\phi_{sca}(\mathbf{r}) = \sum_{m=1}^{N_B} \Delta l w_m \hat{n}'_m \left[ \phi(\mathbf{r}'_m) \nabla' g_b(\mathbf{r} - \mathbf{r}')|_{\mathbf{r}'_m} - g_b(\mathbf{r} - \mathbf{r}'_m) \nabla' \phi(\mathbf{r}')|_{\mathbf{r}'_m} \right], \quad (4.5)$$

where  $\Delta l$  is the incremental length and  $w_m$  the weighting factor depending on the numerical integration method used.

Because  $g_b(\mathbf{r} - \mathbf{r}') = \frac{i}{4} H_0^{(1)}(k_b |\mathbf{r} - \mathbf{r}'|)$ , its gradient evaluated at  $\mathbf{r}_m$  is

$$\nabla' g_b(\mathbf{r} - \mathbf{r}')|_{\mathbf{r}'_m} = \frac{ik_b}{4} (\hat{x} \cos \theta_m + \hat{y} \sin \theta_m) H_1^{(1)}(k_b |\mathbf{r} - \mathbf{r}'_m|), \quad (4.6)$$

where  $\theta_m = \cos^{-1} \frac{x - x'_m}{|\mathbf{r} - \mathbf{r}'_m|}$ .

Substituting (4.6) into (4.5) and recognizing that  $H_{-1}^{(1)}(z) = -H_1^{(1)}(z)$  [19], (4.5) can be cast in the form of (4.3):

$$\phi_{sca}(\mathbf{r}) = \sum_{m=1}^{N_B} \psi^t(k_b, \mathbf{r}_m) \cdot \begin{pmatrix} -c_1(n'_{mx} + in'_{my})\phi(\mathbf{r}'_m) \\ c_2 \hat{n}'_m \cdot \nabla' \phi(\mathbf{r}')|_{\mathbf{r}'_m} \\ c_1(n'_{mx} - in'_{my})\phi(\mathbf{r}'_m) \end{pmatrix}, \quad (4.7)$$

where  $c_1 = \frac{i\Delta l w_m k_b}{8}$ ,  $c_2 = -2c_1/k_b$  and  $n'_{mx}$  and  $n'_{my}$  are the  $x$  and  $y$  components of  $\hat{n}'_m$ . The vector  $\psi(k_b, \mathbf{r}_m)$  contains the cylindrical harmonics and can be written as

$$\psi(k_b, \mathbf{r}_m) = \begin{pmatrix} H_{-1}^{(1)}(k_b r_m) e^{-i\phi_m} \\ H_0^{(1)}(k_b r_m) \\ H_1^{(1)}(k_b r_m) e^{i\phi_m} \end{pmatrix}. \quad (4.8)$$

Therefore,  $\mathbf{b}_m$  can be related to  $\mathbf{a}_j$  through (4.1):

$$\mathbf{b}_m = \begin{pmatrix} -c_1(n'_{mx} + in'_{my}) \sum_{j=1}^{N_A} \psi^t(k_b, \mathbf{r}'_m - \mathbf{r}'_j) \cdot \mathbf{a}_j \\ c_2 \hat{n}'_m \cdot \sum_{j=1}^{N_A} \nabla' \psi^t(k_b, \mathbf{r}'_m - \mathbf{r}'_j)|_{\mathbf{r}'_m} \cdot \mathbf{a}_j \\ c_1(n'_{mx} - in'_{my}) \sum_{j=1}^{N_A} \psi^t(k_b, \mathbf{r}'_m - \mathbf{r}'_j) \cdot \mathbf{a}_j \end{pmatrix}. \quad (4.9)$$

In (4.9),  $\nabla' \psi^t(k_b, \mathbf{r}' - \mathbf{r}'_j)|_{\mathbf{r}'_m}$  after arithmetic manipulation can be further expanded as

$$\nabla' \psi^t(k_b, \mathbf{r}' - \mathbf{r}'_j)|_{\mathbf{r}'_m} = \frac{k_b}{2} \begin{pmatrix} (\hat{x} + i\hat{y})\psi_{-2} - (\hat{x} - i\hat{y})\psi_0 \\ (\hat{x} + i\hat{y})\psi_{-1} - (\hat{x} - i\hat{y})\psi_1 \\ (\hat{x} + i\hat{y})\psi_0 - (\hat{x} - i\hat{y})\psi_2 \end{pmatrix}, \quad (4.10)$$

where  $\psi_n$  denotes  $H_n^{(1)}(k_b|\mathbf{r}'_m - \mathbf{r}'_j|)e^{in\phi'}$  and  $\phi' = \tan^{-1} \frac{y'_m - y'_j}{x'_m - x'_j}$ .

Using (4.10) in (4.9), we then obtain

$$\mathbf{b}_m = \sum_{j=1}^{N_A} \begin{pmatrix} c\psi_{-1} & c\psi_0 & c\psi_1 \\ c\psi_{-2} + c^*\psi_0 & c\psi_{-1} + c^*\psi_1 & c\psi_0 + c^*\psi_2 \\ c^*\psi_{-1} & c^*\psi_0 & c^*\psi_1 \end{pmatrix} \cdot \mathbf{a}_j, \quad (4.11)$$

where  $c = \frac{-i\Delta l w_m k_b}{8}(n'_{mx} + in'_{my})$  and  $c^* = \frac{-i\Delta l w_m k_b}{8}(-n'_{mx} + in'_{my})$ . Hence, the matrix  $\bar{\mathbf{h}}_{mj}$  is found. This matrix describes how the outside sources are related to the inside sources. The transition direction is outgoing. On the other hand, following the same derivation, we can obtain the transformation matrix from the outside sources to the inside sources. The form of the resultant matrix is exactly the same as that of the outgoing matrix except for a preceding minus sign. Both matrices can be written as

$$\bar{\mathbf{h}}_{mj}^{(i)} = -\bar{\mathbf{h}}_{mj}^{(o)} = - \begin{pmatrix} c\psi_{-1} & c\psi_0 & c\psi_1 \\ c\psi_{-2} + c^*\psi_0 & c\psi_{-1} + c^*\psi_1 & c\psi_0 + c^*\psi_2 \\ c^*\psi_{-1} & c^*\psi_0 & c^*\psi_1 \end{pmatrix}, \quad (4.12)$$

where (o) and (i) represent “outgoing” and “incoming,” respectively.

### 4.3 Algorithm Implementation and Its Complexity

We assume that the object is gridded and grouped into many small basic units as shown in Figure 4.2(a). Each basic unit contains 16 nodes, which are divided into two parts: the inner nodes are contained in the dashed circle; the surface nodes lie around the dashed square (see Figure 4.2(b)). Then, the equivalent surface sources contributed from the inner nodes in  $g_{i,0}^e$  are found by (4.11) and are added

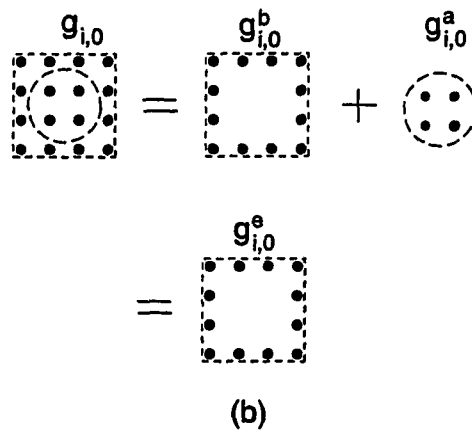
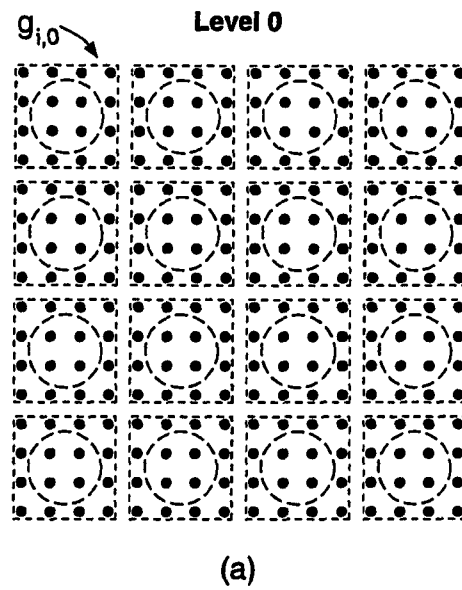


**Figure 4.2.** The diagrams for calculating the outgoing equivalent sources from the 0th level to the 1st level: (a) the original grid and the grouping scheme (b) the contributions to the equivalent sources.

to the original sources in  $g_{i,0}^b$  to yield the resultant surface sources in  $g_{i,0}^e$ . For the region external to  $g_{i,0}$ , the 12 surface sources in  $g_{i,0}^e$  have the same effect as do the 16 original sources in  $g_{i,0}$ . Advancing to the 1st level in Figure 4.3, we group four basic units,  $g_{i,0}^e$ 's, as a subgroup,  $g_{i,1}$ , and following the same procedure as described above, we replace the inside sources in  $g_{i,1}^e$  with the equivalent surface sources. These equivalent surface sources are added to the sources on  $g_{i,1}^b$  to form the resultant surface sources in  $g_{i,1}^e$ . Repeatedly nesting the subgroups,  $g_{i,l-1}^e$  of the  $(l-1)$ -th level, within larger subgroups,  $g_{i,l}$  of the  $l$ -th level, we eventually obtain the four largest groups (see Figure 4.4) with surface sources representing the effects from all of the original sources.

We adopt the trapezoidal integration rule so  $w_m$ 's in (4.11) are 1 except for the end points, where  $w_m$ 's are 0.5. Although the normals at the corner points are not defined, they are viewed as the end points sharing two sides so that there are two contributions from both sides for the corner points. The surface sources for each subgroup in each layer ( $g_{i,0}^e, g_{i,1}^e, \dots, g_{i,L-1}^e$ , assuming that there are  $L$  levels) must be stored for later use in calculating the incoming equivalent sources. If only the outermost surface sources are required in some applications (for example, the far field calculation given the induced sources inside the scatterer), the storage of all surface sources is not necessary. Figure 4.5 shows the side view of the outgoing procedure in NEPAL. Assuming that there are  $N$  points, the operation count for the outgoing procedure can be approximately calculated as  $N[48 \log_2 N - 370 + 760/\sqrt{N} - 379/N]$ .

Therefore, as shown in Figure 4.6, to calculate the field at point  $P$  in in one group from the other three, we have to calculate only the contributions directly from the surface sources in  $g_{2,1}^e, g_{3,1}^e$  and  $g_{4,1}^e$  instead from each original source inside those three groups. Furthermore, we can reverse the outgoing process as mentioned above to calculate the field at each point inside the source region. Starting from the four largest groups in Figure 4.6, the incoming equivalent surface sources in, for example,  $\zeta_{1,1}^e$  can be calculated from the outgoing equivalent sources in  $g_{2,1}^e, g_{3,1}^e$  and  $g_{4,1}^e$  by  $\bar{\mathbf{h}}_{mj}^{(i)}$  in (4.12).

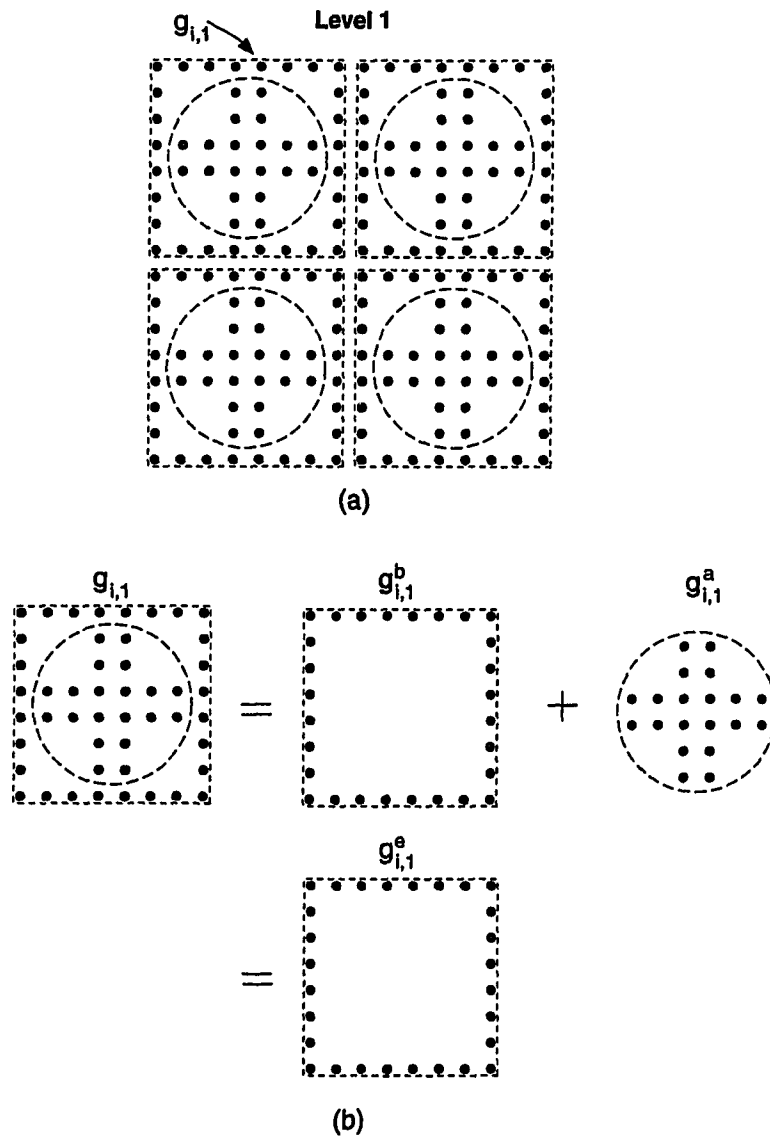
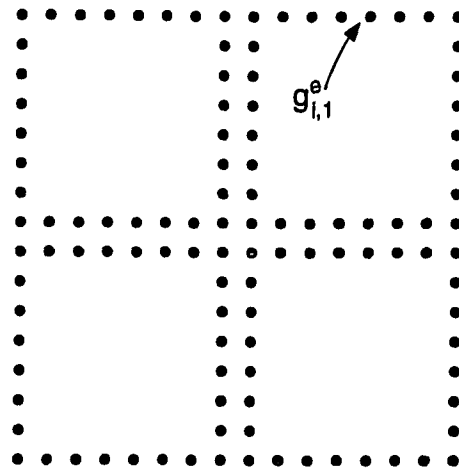


**Figure 4.3.** The diagrams for calculating the outgoing equivalent sources from the 1st level to the 2nd level: (a) the grouping scheme of the 1st level (b) the contributions to the equivalent sources.



Level 2

Figure 4.4. The highest level for calculating the outgoing equivalent sources.

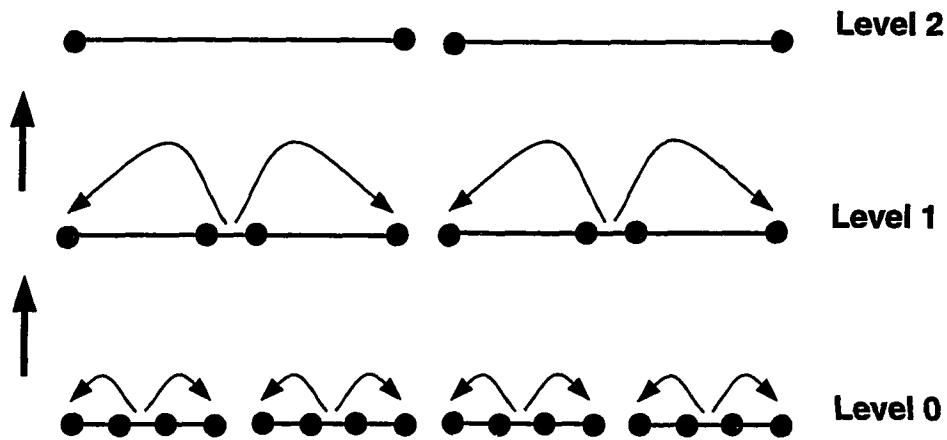
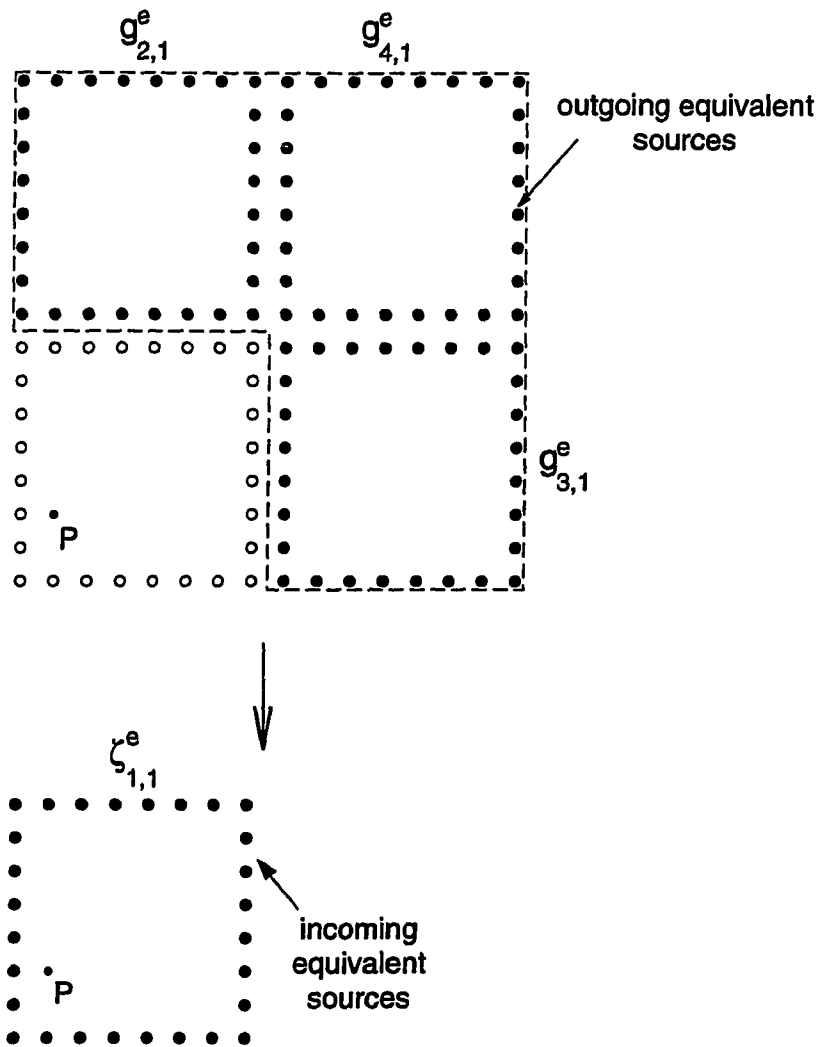
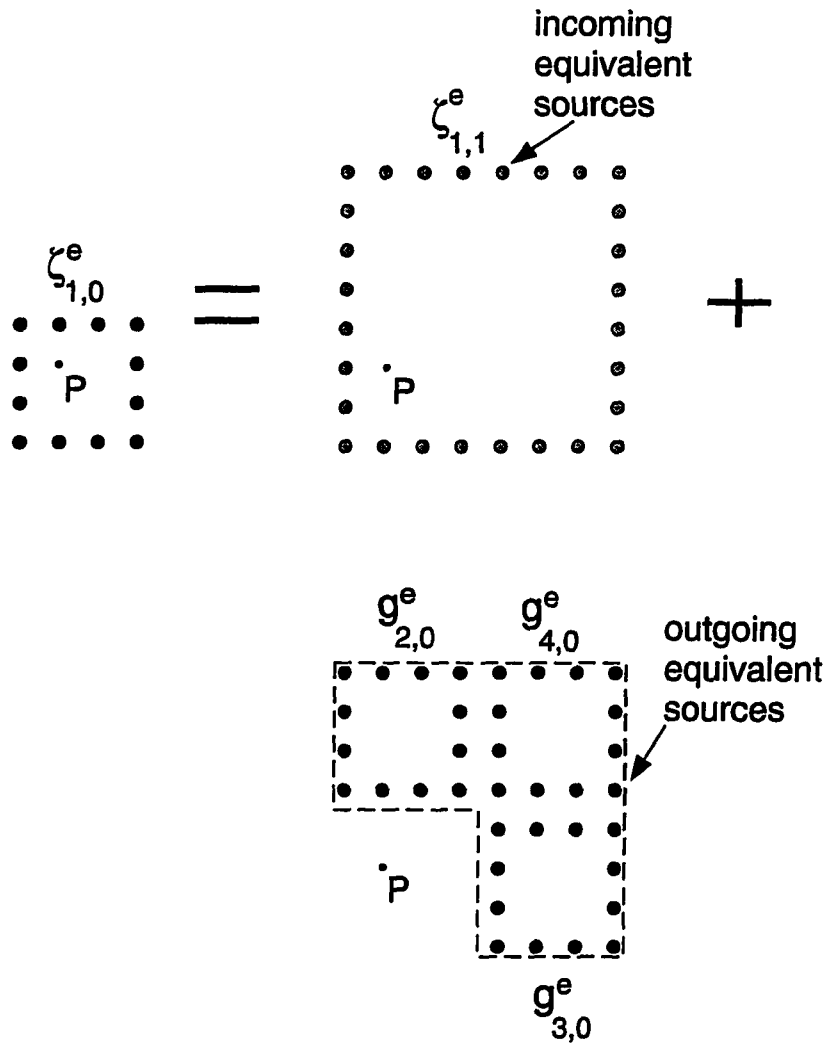


Figure 4.5. The side view of the outgoing procedure in NEPAL.



**Figure 4.6.** The diagram for calculating the incoming equivalent sources in the 2nd level.



**Figure 4.7.** The diagram for calculating the incoming equivalent sources in the 1st level.

Then, as shown in Figure 4.7, the incoming equivalent sources in the subgroup,  $\zeta_{1,0}^e$ , consist of two parts. One contribution is from sources in higher levels,  $\zeta_{1,1}^e$ , and the other one is from the outgoing sources in  $g_{2,0}^e$ ,  $g_{3,0}^e$  and  $g_{4,0}^e$ , that have been

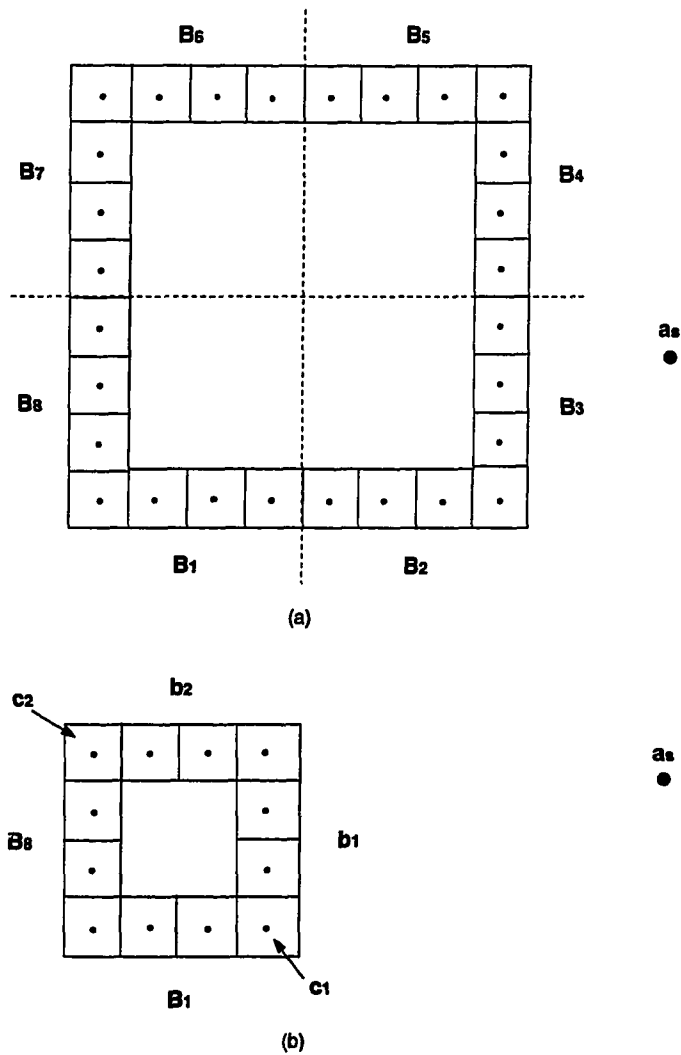


**Figure 4.8.** The diagrams for explaining special treatment required of corner points: (a) calculation of equivalent surface sources on  $B_1$ – $B_8$  (b) calculation of equivalent surface sources on  $b_1$ ,  $b_2$ ,  $B_8$  and  $B_1$ .

calculated and stored in the outgoing process. Both contributions to the incoming equivalent sources are calculated by the linear operator,  $\bar{h}_{mj}^{(i)}$ , as well. Extra caution has to be taken for the first-part calculation. Figure 4.8(a) represents the direct

calculation of equivalent surface sources on  $B_1-B_8$  due to the source  $a_s$ . The lower left quadrant of Figure 4.8(a) is shown in Figure 4.8(b), in which equivalent surface sources on  $b_1, b_2, B_8$  and  $B_1$  are to be found. From the geometry of both figures, the equivalent sources on  $B_8$  and  $B_1$ , except the corner points  $c_1$  and  $c_2$ , are the same for these two diagrams. The equivalent sources on  $b_1$  and  $b_2$  can be accounted for by those on  $B_1-B_8$ . Therefore, the equivalent sources on points such as  $c_1$  and  $c_2$  (they have the feature of not being corner points for higher layers) need be calculated directly instead in a nesting fashion.

In this nesting fashion, all of the other groups in different levels are reduced to a basic unit as shown in Figure 4.9, in which the contributions from many sources external to the basic unit are accounted for by 12 boundary sources in  $\zeta_{i,0}^e$ . The field due to the source at the same position on the surface (for sources inside the basic unit, see Equation (2.3)) cannot be calculated simply by (4.2) because it is a divergent integral when the field point coincides with the source point. However, (4.2) can be evaluated by the principal value integrals [20]. Without detailed derivation, some useful formulas are provided as follows to assist in the evaluation of fields.

$$\int_{\Delta l} d\mathbf{r}'' H_0^{(1)}(k_b r'') = \frac{4i\varepsilon}{\pi} [\log(k_b \varepsilon) - 1] + 2 \int_{\varepsilon}^{\Delta l/2} dr'' H_0^{(1)}(k_b r''), \quad (4.13)$$

$$\int_{\Delta l} d\mathbf{r}'' \hat{n}'_m \cdot (\hat{x} - i\hat{y}) H_1^{(1)}(k_b r'') e^{i\phi''} = \begin{cases} \frac{3i}{k_b}, & \text{for a corner in } \Delta l \\ \frac{2i}{k_b}, & \text{otherwise,} \end{cases} \quad (4.14)$$

$$\int_{\Delta l} d\mathbf{r}'' \hat{n}'_m \cdot (\hat{x} + i\hat{y}) H_{-1}^{(1)}(k_b r'') e^{i\phi''} = \begin{cases} \frac{-3i}{k_b}, & \text{for a corner in } \Delta l \\ \frac{-2i}{k_b}, & \text{otherwise,} \end{cases} \quad (4.15)$$

where  $\Delta l$  is an increment edge of length  $\Delta l$  and  $\varepsilon$  denotes a small number.

Figure 4.10 provides the side view of the incoming procedure and the field-calculation process. The solid lines among different groups in the same level represent the interactions between sources residing in different groups, which correspond to the second-part calculation in Figure 4.7. The dashed lines starting from the

higher levels and ending at the lower levels correspond to the first-part calculation in Figure 4.7. Hence, the operation counts for calculating incoming equivalent sources plus the field at each node are approximately  $N[240 \log_2 N - 1548 + 2664/\sqrt{N} - 1322/N]$ .

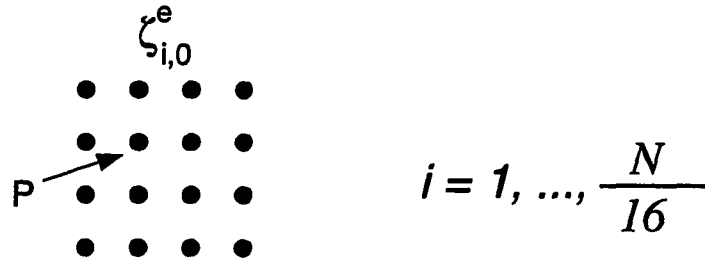


Figure 4.9. The diagram for the field calculation in the 0th level.

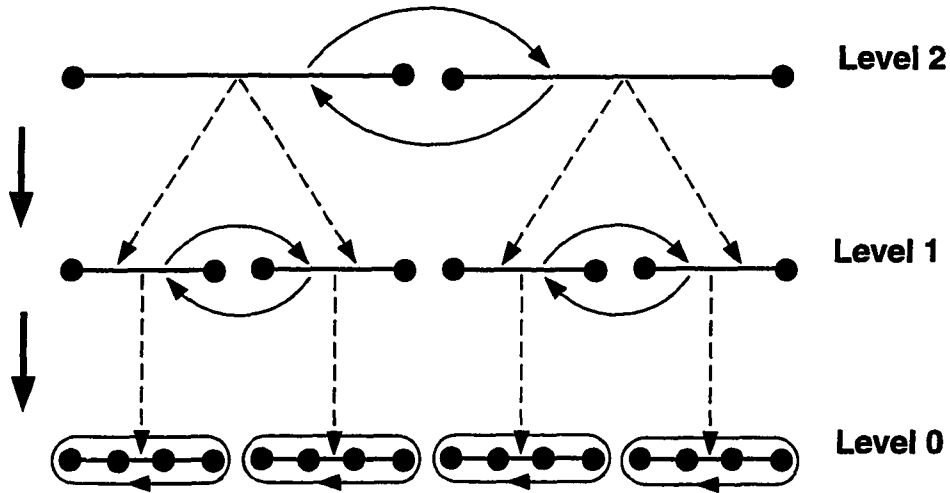


Figure 4.10. The side view of the incoming procedure in NEPAL.

#### 4.4 Comparison with FFT

As a verification example, we use NEPAL and FFT to implement a matrix-vector multiply in which, given sources on a  $16 \times 16$  grid, the field is calculated at each node. Figure 4.11 shows the real and imaginary parts of fields at all nodes. The solid line is by NEPAL and the dashed line is by FFT. The agreement is good.

For efficiency comparison, we performed several matrix-vector multiplies for different cases by NEPAL and FFT on the Cray-YMP machine. The CPU time versus the number of points by both methods is shown in Figure 4.12. For the largest case, FFT is about 7 times faster than NEPAL. The operation counts of FFT for a matrix-vector multiply are about  $40N \log_2 N + 80N$ . On the other hand, NEPAL requires  $288N \log_2 N - 1917N$  operations (as discussed in the previous section). While  $N$  is large, FFT is 7 times more efficient than NEPAL. The large pre-factor of NEPAL is due to the direct calculation of the equivalent sources on the surface, which is similar to doing the matrix-vector multiply directly in solving the surface integral equation. We will introduce fast multipole method (FMM) in the next section to alleviate the computational intensity.

To reduce the overhead of implementing NEPAL, some frequently used factors depending only on the geometry, such as cylindrical harmonics, are calculated and stored. Considering the required storage of outgoing equivalent sources, the memory required by NEPAL is larger than that of FFT, even though in the latter case, one has to extend the Toeplitz matrix into a circulant matrix four times as large as the original one.

As mentioned in the introduction, NEPAL would prevail over FFT when the far fields instead of the internal fields are of interest. This point can be justified by operation counts of the NEPAL outgoing procedure,  $N[48 \log_2 N - 370]$ , which is about the same as that of FFT. But in this application, invoking FFT involves dividing a much larger area in which the sources reside only in a small subregion. This results in a  $N'$  much larger than  $N$ . Also, notice that the outgoing equivalent

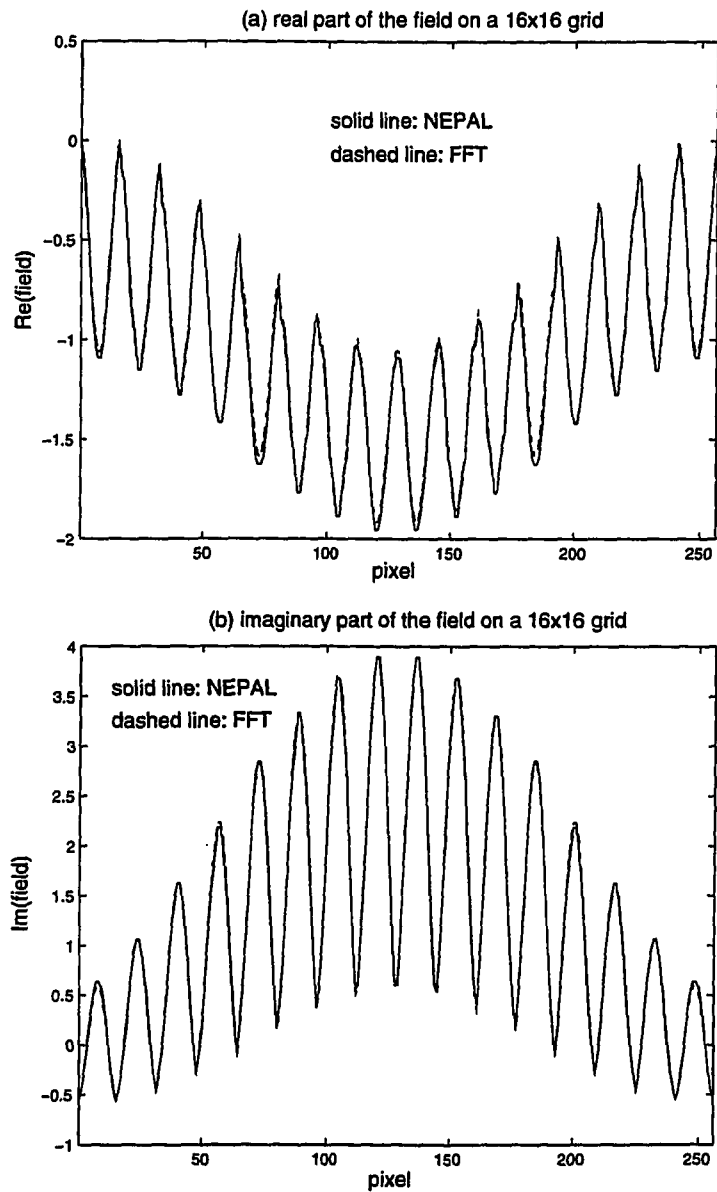


**Figure 4.11.** Comparison of calculated fields by NEPAL (solid line) and FFT (dashed line). A uniform source distribution is given on a  $16 \times 16$  grid.

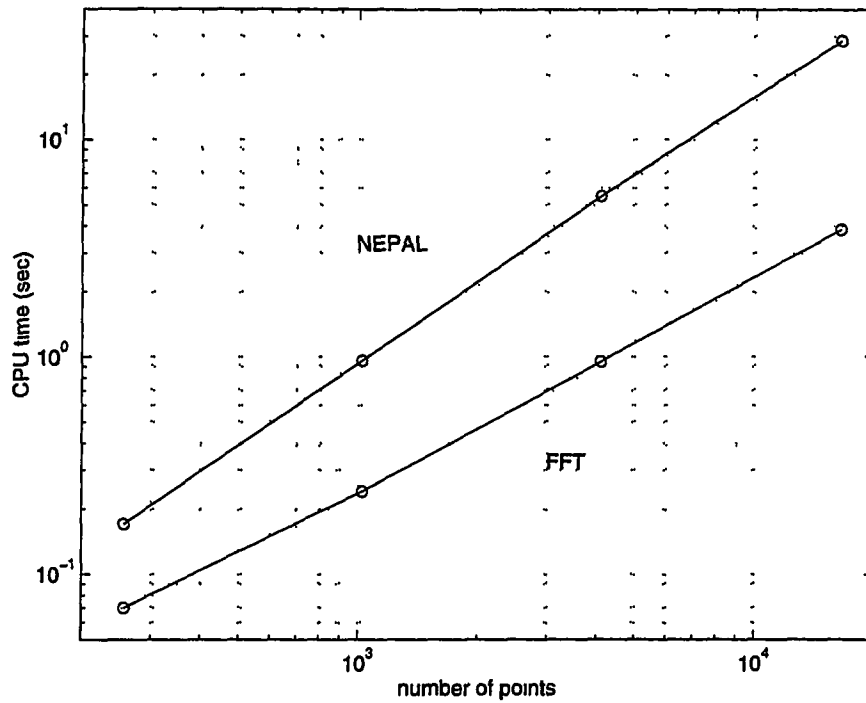


**Figure 4.12.** Comparison of CPU time in a matrix-vector multiply by NEPAL and FFT for different-size cases.

sources on layers other than the outmost layer are no longer needed when the equivalent sources of the higher level are found, which saves more required memory storage.

#### 4.5 $O(N)$ Algorithm by Fast Multipole Method

FMM was proposed by Rokhlin [14]. It is applied in matrix-vector multiply when iterative methods are used to solve surface integral equations. Instead of doing the matrix-vector multiply point to point, FMM divides all points into several groups and for each group, it collects the contribution from group elements at some point,

usually the centroid of the group. Then it finds the interaction among the groups. Finally, to the contrary of the first stage of aggregation, it distributes the resultant interaction to each group elements.

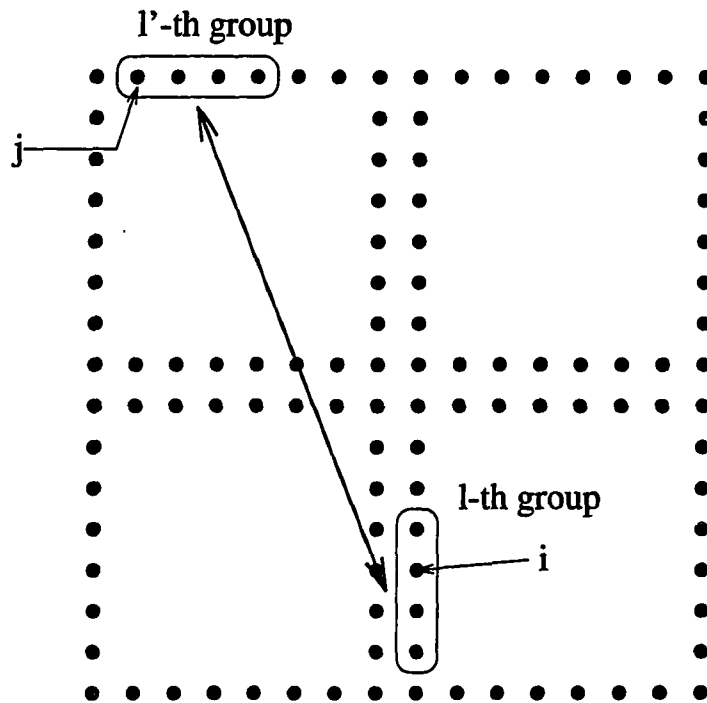


**Figure 4.13.** Illustration of the calculation of element-element interactions by FMM.

Shown in Figure 4.13 is a case in which the field at each point of a block is calculated from all other sources at the other three blocks. Direct calculation involves point-to-point evaluation characterized by  $H_{\nu}^{(1)}(k_{\nu}r_{ji})e^{i\nu\theta_{ji}}$ , where  $r_{ji}$  and  $\theta_{ji}$  are the two components of  $\mathbf{r}_{ji}$ , the vector from the  $i$ -th element to the  $j$ -th element. We assume that the center of the group where the  $i$ -th point belongs is denoted by  $l$ , and that for the  $j$  element by  $l'$ . Using the addition theorem [19],

[20], the cylindrical harmonics can be written as

$$\begin{aligned} H_\nu^{(1)}(k_b r_{ji}) e^{i\nu\theta_{ji}} &= H_\nu^{(1)}(k_b |\mathbf{r}_{j\nu} - \mathbf{r}_{i\nu}|) e^{i\nu\theta_{ji}} \\ &= e^{i\nu\pi} \sum_{m=-P/2}^{P/2-1} J_m(k_b r_{j\nu}) e^{im(\theta_{j\nu}-\pi)} H_{-(m-\nu)}^{(1)}(k_b |\mathbf{r}_{i\nu} - \mathbf{r}_{l\nu}|) e^{-i(m-\nu)\theta_{i\nu}}, \quad r_{j\nu} < r_{i\nu}, \end{aligned} \quad (4.16)$$

where  $P$  should be large enough to maintain the accuracy of expansion and usually is  $O(\sqrt{M})$ , where  $M$  is the group size. Equation (4.15) can be further expanded by applying the addition theorem on the Hankel function. Hence,

$$\begin{aligned} H_\nu^{(1)}(k_b r_{ji}) e^{i\nu\theta_{ji}} &= e^{i\nu\pi} \sum_{m=-P/2}^{P/2-1} J_m(k_b r_{j\nu}) e^{im(\theta_{j\nu}-\pi)} \\ &\quad \sum_{n=m-P/2}^{m+P/2-1} H_{m-n-\nu}^{(1)}(k_b r_{l\nu}) e^{-i(m-n)\theta_{l\nu}} J_n(k_b r_{li}) e^{-in\theta_{li}}, \quad r_{il} < r_{l\nu}, \end{aligned} \quad (4.17)$$

or more compactly,

$$= e^{i\nu\pi} \underbrace{\beta_{j\nu}^t}_{1 \times P} \cdot \underbrace{\bar{\alpha}_{l\nu}}_{P \times P} \cdot \underbrace{\beta_{li}}_{P \times 1}, \quad (4.18)$$

where  $\beta_{j\nu}^t$ ,  $\bar{\alpha}_{l\nu}$  and  $\beta_{li}$  represent the disaggregate, translation and aggregate matrices, respectively:

$$[\beta_{j\nu}]_m = J_m(k_b r_{j\nu}) e^{im(\theta_{j\nu}-\pi)}, \quad m = -\frac{P}{2}, -\frac{P}{2} + 1, \dots, \frac{P}{2} - 1. \quad (4.19)$$

$$\begin{aligned} [\bar{\alpha}_{l\nu}]_{mn} &= H_{m-n-\nu}^{(1)}(k_b r_{l\nu}) e^{-i(m-n)\theta_{l\nu}}, \\ n &= m - \frac{P}{2}, m - \frac{P}{2} + 1, \dots, m + \frac{P}{2} - 1. \end{aligned} \quad (4.20)$$

$$[\beta_{li}]_n = J_n(k_b r_{li}) e^{-in\theta_{li}}. \quad (4.21)$$

Suppose that there are  $\frac{N}{4}$  points in each block in Figure 4.13. Then, there are  $\frac{3N}{4M}$  groups to affect  $\frac{N}{4M}$  groups on the other block. Therefore, in the first stage, aggregation requires  $O(\frac{3N}{4M} P M)$  operations; the translation stage needs  $O(\frac{N}{4M} P^2 \frac{3N}{4M})$

operations; similar to the aggregate stage, the complexity for the disaggregate stage is  $\frac{N}{4M} P M$ . Because  $P \sim M$ , the total complexity of implementing (4.17) is still  $N^2$ . The main cost comes from the translation stage.

Yet, by plane-wave expansion of Bessel functions in (4.16),  $\bar{\alpha}_{l'l}$  can be diagonalized. From [20],

$$J_m(k_b r_{j'l'}) e^{im\theta_{j'l'}} = \frac{1}{2\pi} \int_0^{2\pi} d\alpha e^{ik_b r_{j'l'} \cos(\alpha - \theta_{j'l'}) + im(\alpha - \frac{\pi}{2})}, \quad (4.22)$$

and

$$J_n(k_b r_{li}) e^{-in\theta_{li}} = \frac{1}{2\pi} \int_0^{2\pi} d\alpha' e^{ik_b r_{li} \cos(\alpha' + \theta_{li}) + in(\alpha' - \frac{\pi}{2})}. \quad (4.23)$$

Substituting (4.18) and (4.19) into (4.16), exchanging the order of integration and summation and replacing  $m - n$  with  $p$ , we obtain

$$\begin{aligned} H_\nu^{(1)}(k_b r_{ji}) e^{i\nu\theta_{ji}} &= \frac{1}{(2\pi)^2} \int_0^{2\pi} d\alpha \int_0^{2\pi} d\alpha' e^{ik_b r_{j'l'} \cos(\alpha - \theta_{j'l'} + \pi)} e^{ik_b r_{li} \cos(\alpha' + \theta_{li})} \\ &e^{i\nu\pi} \sum_{p=-P/2}^{P/2-1} H_{p-\nu}^{(1)}(k_b r_{l'l}) e^{-i(p-\nu)\theta_{l'l}} e^{-ip(\alpha' - \frac{\pi}{2})} \sum_{m=-P/2}^{P/2-1} e^{im(\alpha + \alpha' - \pi)}. \end{aligned} \quad (4.24)$$

Note that the second summation in (4.20) results in a delta function,  $2\pi\delta(\alpha + \alpha' - \pi)$  as  $P \rightarrow \infty$ . Consequently, the double integrals in (4.20) are reduced by one:

$$\begin{aligned} H_\nu^{(1)}(k_b r_{ji}) e^{i\nu\theta_{ji}} &= \frac{e^{i\nu\pi}}{2\pi} \int_0^{2\pi} d\alpha e^{-ik_b r_{j'l'} \cos(\alpha - \theta_{j'l'})} \\ &e^{i\nu\theta_{l'l}} \sum_{p=-P/2}^{P/2-1} H_{p-\nu}^{(1)}(k_b r_{l'l}) e^{-ip(\theta_{l'l} - \alpha + \frac{\pi}{2})} e^{-ik_b r_{li} \cos(\alpha - \theta_{li})}. \end{aligned} \quad (4.25)$$

Using compact notation, (4.21) can be written as

$$H_\nu^{(1)}(k_b r_{ji}) e^{i\nu\theta_{ji}} = \frac{e^{i\nu\pi}}{2\pi} \int_0^{2\pi} d\alpha \tilde{\beta}_{j'l'}(\alpha) \tilde{\alpha}_{l'l}(\alpha) \tilde{\beta}_{li}(\alpha), \quad (4.26)$$

where

$$\tilde{\beta}_{j'l'}(\alpha) = e^{-ik_b r_{j'l'} \cos(\alpha - \theta_{j'l'})}, \quad (4.27)$$

$$\tilde{\alpha}_{l'l}(\alpha) = e^{i\nu\theta_{l'l}} \sum_{p=-P/2}^{P/2-1} H_{p-\nu}^{(1)}(k_b r_{l'l}) e^{-ip(\theta_{l'l} - \alpha + \frac{\pi}{2})}, \quad (4.28)$$

and

$$\tilde{\beta}_{li}(\alpha) = e^{-ik_b r_{li} \cos(\alpha - \theta_{li})}. \quad (4.29)$$

The integral in (4.25) can be approximated by a  $Q$ -point summation, and  $Q$  can be proved to be proportional to  $M$ . Then, (4.25) can be expressed as

$$H_\nu^{(1)}(k_b r_{ji}) e^{i\nu\theta_{ji}} = \frac{e^{i\nu\pi}}{2\pi} \underbrace{\tilde{\beta}_{j'l'}^t}_{1 \times Q} \cdot \underbrace{\overline{\mathcal{D}}(\tilde{\alpha}_{l'l})}_{Q \times Q} \cdot \underbrace{\tilde{\beta}_{li}}_{Q \times 1}, \quad (4.30)$$

where  $\overline{\mathcal{D}}$  converts a vector into a square diagonal matrix. The costs of each stage are  $O(\frac{3N}{4M} PQ)$ ,  $O(\frac{N}{4M} Q \frac{3N}{4M})$  and  $O(\frac{N}{4M} PQ)$ , respectively. Because  $Q$  and  $P$  is  $O(M)$ , the total cost is

$$T = C_1 \frac{N^2}{M} + C_2 NM, \quad (4.31)$$

where  $C_1$  and  $C_2$  are some constants. By choosing  $M = \sqrt{(C_1/C_2)N}$ , the cost could be minimized as

$$T = 2\sqrt{C_1/C_2} N^{1.5}. \quad (4.32)$$

Note that for two close groups not satisfying the conditions in (4.15) and (4.16), the direct calculations are performed. Also note that  $\tilde{\alpha}_{l'l}(\alpha)$  can be calculated efficiently by FFT, as indicated in (4.27).

Therefore, by applying FMM in NEPAL for calculating equivalent surface sources, a small pre-factor ensues. The size of the group is crucial for FMM. Because the surface points in each layer are not the same, different group sizes are required for different layers. For lower layers, because the surface points of each block are few, a direct calculation is more efficient. If the total points  $N$  is very large, the cost

by direct calculation either in lower layers or for nearby groups is small compared with the cost entailed by NEPAL with FMM. Then the matrix-vector multiply can be achieved in  $O(N)$  operations.

Some of our preliminary results show improvement in the pre-factor, although it is not substantial and still less efficient than FFT. This is mainly because the size of each group as needed in FMM is not optimal and the problem size is not large enough.

#### 4.6 Conclusions

NEPAL, an  $N \log N$  algorithm for the matrix-vector multiply, is developed. Due to the large pre-factor, NEPAL is still less efficient than FFT. With FMM fully incorporated in NEPAL and large  $N$ , not only can the pre-factor be reduced, an  $O(N)$  algorithm can also be achieved.

NEPAL requires more memory storage than does FFT to store intermediate results and to reduce the overhead.

In some applications, NEPAL would prevail over FFT. Far field calculation for a large amount of observation points (for example,  $O(\sqrt{N})$  receivers in Chapter 3) by NEPAL (actually, the outgoing part of NEPAL) can be achieved in  $O(N \log N)$  operations.

Figure 4.14 shows a highly inhomogeneous medium, which to keep  $N$  small, is more suitable for nonuniform grids than for uniform grids. FFT can be applied only to uniform grids, whereas NEPAL can be applied directly in nonuniform grids and would have a favorable comparison over FFT when the ratio of the numbers of cells by both schemes is over 7.2.

Although NEPAL in this chapter is presented in the two-dimensional form, it can be extended into the three-dimensional form in a straightforward manner. The

methodology and the procedure for the three-dimensional version are exactly the same as for the two-dimensional one except that the two-dimensional cylindrical functions in the matrix and/or vector elements must be changed into the three-dimensional spherical functions.

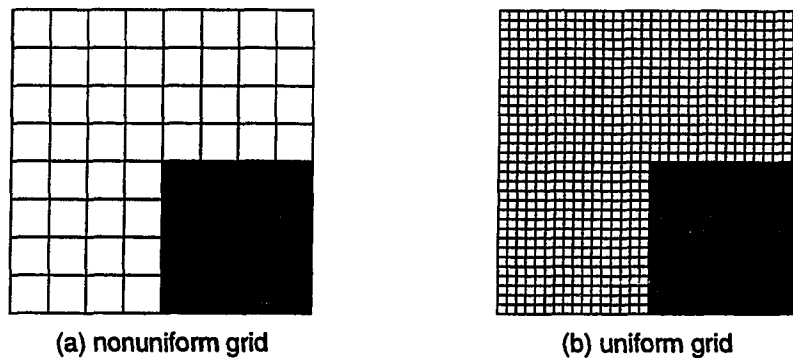


**Figure 4.14.** The nonuniform and uniform grids for objects of very different compositions.

#### 4.7 References

- [1] D. T. Borup and O. P. Gandhi, "Calculation of high-resolution SAR distributions in biological bodies using the FFT algorithm and conjugate gradient method," *IEEE Trans. Microwave Theory Tech.*, vol. 33, no. 5, pp. 417-419, 1985.
- [2] D. T. Borup, D. M. Sullivan, and O. P. Gandhi, "Comparison of the FFT conjugate gradient method and the finite-difference time-domain method for the 2-D absorption problem," *IEEE Trans. Microwave Theory Tech.*, vol. 35, no. 4, pp. 383-395, 1987.
- [3] T. K. Sarkar, "Application of FFT and the conjugate gradient method for the solution of electromagnetic radiation from electrically large and small conducting bodies," *IEEE Trans. Antennas Propag.*, vol. 34, no. 5, pp. 635-640, 1986.
- [4] M. F. Cátedra, "Solution to some electromagnetic problems using fast Fourier transform with conjugate gradient method," *Electron. Lett.*, vol. 22, no. 20, pp. 1049-1051, 1986.

- [5] T. J. Peters and J. L. Volakis, "On the formulation and implementation of a conjugate gradient FFT method," *J. Electromag. Waves Appl.*, vol. 3, no. 8, pp. 675-696, 1989.
- [6] C. Y. Shen, K. J. Glover, M. I. Sancer, and A. D. Varvatsis, "The discrete Fourier transform method of solving differential-integral equations in scattering theory," *IEEE Trans. Antennas Propag.*, vol. 37, no. 8, pp. 1032-1041, 1989.
- [7] K. Barkeshli and J. L. Volakis, "On the implementation of the conjugate gradient Fourier transform method for scattering by planar plates," *IEEE Antennas Propag. Soc. Mag.*, pp. 19-26, April 1990.
- [8] A. P. M. Zwamborn and P. M. van den Berg, "A weak form of the conjugate gradient FFT method for plate problems," *IEEE Trans. Antennas Propag.*, vol. 39, no. 2, pp. 224-228, 1991.
- [9] J.-H. Lin and W. C. Chew, "A comparison of the CG-FFT method and the recursive aggregate T-matrix algorithm," in *IEEE Antennas and Propagation Society International Symposium Digest*, pp. 1591-1594, 1992.
- [10] W. C. Chew and C. C. Lu, "NEPAL—an algorithm for solving the volume integral equation," *Microw. Opt. Tech. Lett.*, vol. 6, no. 3, pp. 185-188, 1993.
- [11] W. C. Chew and C. C. Lu, "The use of Huygens' equivalence principle for solving the volume integral equation of scattering," *IEEE Trans. Antennas Propag.*, vol. 41, no. 7, pp. 897-904, July 1993.
- [12] C. C. Lu and W. C. Chew, "The use of Huygens' equivalence principle for solving 3D volume integral equation of scattering," *IEEE Trans. Antennas Propag.*, vol. 43, no. 5, pp. 500-507, May 1995.
- [13] J.-H. Lin and W. C. Chew, "An application of nested equivalence principle algorithm (NEPAL) in matrix-vector multiplication of iterative algorithms," *IEEE APS Int. Symp.*, Ann Arbor, MI, June 1993, pp. 500-503.
- [14] V. Rokhlin, "Rapid solution of integral equations of scattering theory in two dimensions," *J. Comput. Phys.*, vol. 86, no. 2, pp. 414-439, February 1990.
- [15] N. Engheta, W. D. Murphy, V. Rokhlin, and M. S. Vassiliou, "The fast multipole method (FMM) for electromagnetic scattering problems," *IEEE Trans. Antennas Propag.*, vol. 40, no. 6, pp. 634-641, July 1992.
- [16] C. C. Lu and W. C. Chew, "A multilevel algorithm for solving boundary integral equations of wave scattering," *Microw. Opt. Tech. Lett.*, vol. 7, no. 10, pp. 466-470, July 1994.

- [17] R. L. Wagner and W. C. Chew, "A ray-propagation fast multipole algorithm," *Microw. Opt. Tech. Lett.*, vol. 7, no. 10, pp. 435-438, July 1994.
- [18] J. M. Song and W. C. Chew, "Fast multipole method solution using parametric geometry," *Microw. Opt. Tech. Lett.*, vol. 7, no. 16, pp. 769-765, November 1994.
- [19] M. Abramowitz and I. A. Stegun, *Handbook of Mathematical Functions*. New York: Dover Publications, 1965.
- [20] W. C. Chew, *Waves and Fields in Inhomogeneous Media*. New York: Van Nostrand Reinhold, 1990.

## CHAPTER 5

### 3D SCATTERING SOLUTIONS BY THE BiCG-FFT T-MATRIX METHOD

#### 5.1 Introduction

The scattering of electromagnetic fields by inhomogeneous bodies is a research topic that finds applications in many fields. In this chapter, we propose a method of solving the inhomogeneous body problem by approximating the inhomogeneous body with small dielectric cubes. The dielectric cubes are then approximated by equivolume spheres [1]-[6] (see Figure 5.1). The T matrix [7], [8] of each individual sphere can be found in closed form. A set of linear algebraic equations can be easily derived to solve for the scattering amplitudes from each of the spheres. By using this T-matrix formulation, the Green's function singularity problem is avoided, while in other formulations, such as the method of moments [9], such a singularity has to be handled with caution [10]-[12].

Direct solvers such as Gaussian elimination can be applied to solve for the scattering amplitudes in  $O(N^3)$  operations and require  $O(N^2)$  filling time and storage of the matrix, where  $N$  is the number of unknowns. However, the computation is prohibitively intensive for large objects, and the tremendous memory requirement cannot be met by most computers.

Iterative solvers such as the conjugate gradient method (CG) [13], [14] or the bi-conjugate gradient (BiCG) method [15]-[17] can be used to circumvent the matrix storage difficulty, although there are still  $O(N^2)$  operations in each iteration and the total number of iterations for convergence is problem-dependent. In this work, we apply BiCG to solve the matrix equation iteratively. When an iterative solver is used, the main cost of seeking the solution is the cost of performing a matrix-vector multiply. But when the inhomogeneous body is discretized into a regular grid, the resultant equation has a block-Toeplitz structure. Exploiting the block-Toeplitz

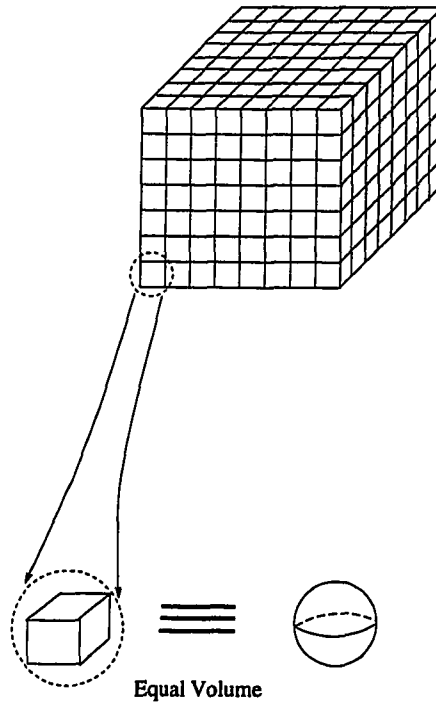


**Figure 5.1.** Discretize an object and replace each subscatterer with a equal-volume subsphere.

structure, we can perform the matrix-vector multiply in  $O(N \log N)$  operations by FFT [10]-[12], [18].

The method can be shown to require  $O(N)$  memory storage. Hence, it can be used to solve fairly large problems. Both scattered fields and internal fields can be found. A volume scattering problem with 90,000 unknowns is solved on a Sun SPARC 10 workstation (10 MFLOPS machine). It is shown that iterative solvers converge faster for lossy bodies than for lossless ones. This is because the matrix condition number for the former cases is smaller than that for the latter ones, because a lossless body could have high  $Q$  internal resonance modes.

As the simulation results show, by using the T-matrix formulation, the condition number of the resultant matrix is independent of the mesh size of a uniform grid. Therefore, the number of iterations does not grow when the body is gridded finer in order to achieve better resolution.

## 5.2 T-Matrix Formulation

### 5.2.1 Scattered fields and internal fields

An inhomogeneous scatterer is first divided into  $N$  subscatterers. Each subscatterer is centered at  $\mathbf{r}'_i$ . The total field due to  $N$  subscatterers can be written as

$$\mathbf{E}(\mathbf{r}) = \underbrace{\psi^t(k_0, \mathbf{r}_s) \cdot \mathbf{a}_s}_{\text{incident field}} + \underbrace{\sum_{i=1}^N \psi^t(k_0, \mathbf{r}_i) \cdot \mathbf{b}_i}_{\text{scattered field}}, \quad (5.1)$$

where  $\mathbf{r}_s = \mathbf{r} - \mathbf{r}'_s$ ,  $\mathbf{r}_i = \mathbf{r} - \mathbf{r}'_i$  and  $\mathbf{r}'_i$  denotes the source location.  $\psi^t(k_0, \mathbf{r}_i)$  is a row vector containing the vector spherical harmonics from each subscatterer. The first term in (5.1) comprises the incident field, while the second term is the scattered field. The vectors  $\mathbf{a}_s$  and  $\mathbf{b}_i$  contain the amplitudes of the incident field harmonics and the scattered field harmonics from the  $i$ -th subscatterer, respectively.

$\psi(k, \mathbf{r})$  is given by (see [18], [21]-[23])

$$[\psi(k, \mathbf{r})]_{lm} = [\mathbf{M}_{lm}(k, \mathbf{r}) \quad \mathbf{N}_{lm}(k, \mathbf{r})], \quad l = 1, 2, \dots, \quad m = -l, -l+1, \dots, l, \quad (5.2)$$

where vector wave functions  $\mathbf{M}_{lm}(k, \mathbf{r})$  and  $\mathbf{N}_{lm}(k, \mathbf{r})$  are defined as

$$\mathbf{M}_{lm}(k, \mathbf{r}) = \nabla \times \mathbf{r} \Psi_{lm}(k, \mathbf{r}), \quad \mathbf{N}_{lm}(k, \mathbf{r}) = \frac{1}{k} \nabla \times \mathbf{M}_{lm}(k, \mathbf{r}). \quad (5.3)$$

In the above,

$$\Psi_{lm}(k, \mathbf{r}) = h_l^{(1)}(kr) Y_{lm}(\theta, \phi), \quad (5.4)$$

and

$$Y_{lm}(\theta, \phi) = (-1)^m \sqrt{\frac{(2l+1)(l-m)!}{4\pi(l+m)!}} P_l^m(\cos\theta) e^{im\phi}, \quad (5.5)$$

$$Y_{l,-m}(\theta, \phi) = (-1)^m Y_{lm}^*(\theta, \phi), \quad (5.6)$$

where  $h_l^{(1)}(kr)$  is the  $l$ -th order spherical Hankel function of first kind and  $P_l^m(\cos\theta)$  is the associated Legendre function.  $Y_{lm}(\theta, \phi)$  defined in (5.5) are the normalized spherical harmonics satisfying [24]

$$\int Y_{lm}(\theta, \phi) Y_{l'm'}^* d\Omega = \delta_{ll'} \delta_{mm'}, \quad (5.7)$$

where the infinitesimal solid angle  $d\Omega$  is equal to  $\sin\theta d\theta d\phi$ .

In the spherical coordinate,  $\mathbf{M}_{lm}(k, \mathbf{r})$  and  $\mathbf{N}_{lm}(k, \mathbf{r})$  defined in (5.3) can be explicitly written as

$$\mathbf{M}_{lm}(k, \mathbf{r}) = \hat{\theta} \frac{im}{\sin\theta} h_l^{(1)}(kr) Y_{lm}(\theta, \phi) - \hat{\phi} h_l^{(1)}(kr) \frac{\partial Y_{lm}(\theta, \phi)}{\partial\theta}, \quad (5.8)$$

$$\begin{aligned} \mathbf{N}_{lm}(k, \mathbf{r}) = & \hat{r} \frac{l(l+1)}{kr} h_l^{(1)}(kr) Y_{lm}(\theta, \phi) + \hat{\theta} \frac{1}{kr} \frac{\partial}{\partial r} [r h_l^{(1)}(kr)] \frac{\partial Y_{lm}(\theta, \phi)}{\partial\theta} \\ & + \hat{\phi} \frac{im}{kr \sin\theta} \frac{\partial}{\partial r} [r h_l^{(1)}(kr)] Y_{lm}(\theta, \phi). \end{aligned} \quad (5.9)$$

Focusing on the  $j$ -th subscatterer, we can use the vector addition theorem or the translation matrix [6], [19], [25], [26] (or see Section 5.2.2) to change the coordinates of all of the spherical harmonics to that of the  $j$ -th subscatterer to obtain

$$\begin{aligned} \mathbf{E}(\mathbf{r}) = & \Re g \psi^t(k_0, \mathbf{r}_j) \cdot \bar{\alpha}_{j_s} \cdot \mathbf{a}_s + \Re g \psi^t(k_0, \mathbf{r}_j) \cdot \sum_{\substack{i=1 \\ i \neq j}}^N \bar{\alpha}_{j_i} \cdot \mathbf{b}_i \\ & + \psi^t(k_0, \mathbf{r}_j) \cdot \mathbf{b}_j, \end{aligned} \quad (5.10)$$

where  $\Re g \psi^t(k_0, \mathbf{r}_j)$  means replacing  $h_l^{(1)}(kr)$  in (5.8) and (5.9) with  $j_l(kr)$ , the  $l$ -th order spherical Bessel function. The translation matrices  $\bar{\alpha}_{j_s}$  and  $\bar{\alpha}_{j_i}$  allow the change of coordinates of the wave functions.

Looking at (5.10) and Figure 5.2, we see that the first two terms are incident waves impinging on the  $j$ -th subscatterer, while the third term is the scattered field off the  $j$ -th subscatterer. Therefore, the amplitude of the third term must be related to the total amplitude of the first two terms via the isolated scatterer T matrix of

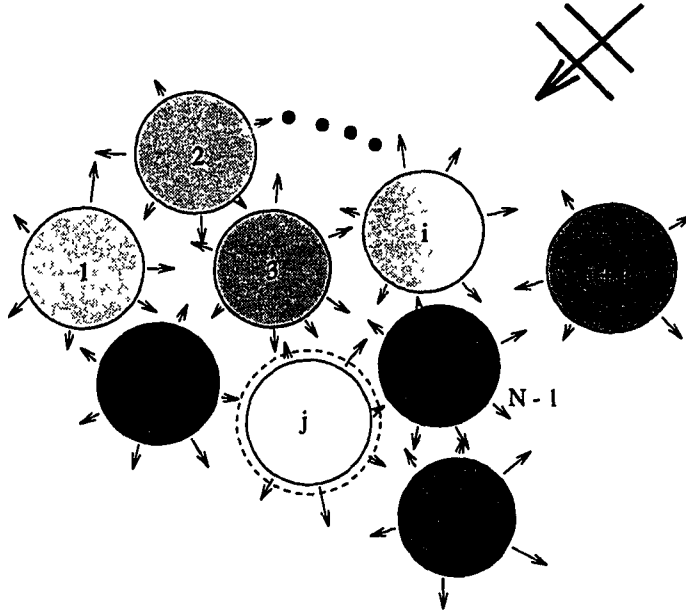


**Figure 5.2.** Multiple scattering from  $N$  subscatterers. The total field impinging on the  $j$ -th subscatterer consists of the incident field and all scattered fields from the other subscatterers.

the  $j$ -th subscatterer, i.e.,  $\bar{\mathbf{T}}_{j(1)}$ . Here,  $\bar{\mathbf{T}}_{j(1)}$  is diagonal for the spherical scatterer (see [8], [21], [22] or Section 5.2.2). Consequently, we have

$$\mathbf{b}_j = \bar{\mathbf{T}}_{j(1)} \cdot \underbrace{\left[ \bar{\alpha}_{js} \cdot \mathbf{a}_s + \sum_{\substack{i=1 \\ i \neq j}}^N \bar{\alpha}_{ji} \cdot \mathbf{b}_i \right]}_{\text{total impinging field amplitude at } j\text{-th subscatterer}}, \quad j = 1, \dots, N. \quad (5.11)$$

Essentially, we match the boundary condition at the surface of the  $j$ -th subscatterer instead of at the center of the scatterer. This explains why this formulation avoids the singularity problem.

Equation (5.11) could be rewritten as

$$\mathbf{b}_j - \bar{\mathbf{T}}_{j(1)} \cdot \sum_{\substack{i=1 \\ i \neq j}}^N \bar{\alpha}_{ji} \cdot \mathbf{b}_i = \bar{\mathbf{T}}_{j(1)} \cdot \bar{\alpha}_{js} \cdot \mathbf{a}_s \quad (5.12)$$

or

$$\mathbf{B} - \bar{\mathbf{T}} \cdot \bar{\mathbf{A}} \cdot \mathbf{B} = \bar{\mathbf{T}} \cdot \mathbf{S}, \quad (5.13)$$

where  $\bar{\mathbf{T}}$  and  $\bar{\mathbf{A}}$  are block matrices, and  $\mathbf{B}$  and  $\mathbf{S}$  are block vectors whose block elements are given by

$$[\bar{\mathbf{T}}]_{ij} = \delta_{ij} \bar{\mathbf{T}}_{j(1)}, \quad (5.14a)$$

$$[\bar{\mathbf{A}}]_{ij} = \begin{cases} \bar{\alpha}_{ij}, & \text{if } j \neq i \\ 0, & \text{otherwise,} \end{cases} \quad (5.14b)$$

$$[\mathbf{B}]_j = \mathbf{b}_j, \quad (5.14c)$$

$$[\mathbf{S}]_j = \bar{\alpha}_{js} \cdot \mathbf{a}_s. \quad (5.14d)$$

After solving for  $\mathbf{B}$  in (5.13), the scattered field can be calculated by (5.1). As to the internal field, because the total impinging field amplitude,  $\mathbf{d}_j$ , at the  $j$ -th subscatterer can be obtained from (5.11), the transmitted field amplitude can be obtained by multiplying  $\mathbf{d}_j$  by the transmission matrix  $\bar{\tau}_j$  (see Section 5.2.2). Then the field at the center of the  $j$ -th subscatterer can be expressed as

$$\Re g \psi^t(k_0, 0) \cdot \mathbf{d}_j = \Re g \psi^t(k_0, 0) \cdot \left[ \bar{\alpha}_{js} \cdot \mathbf{a}_s + \sum_{\substack{i=1 \\ i \neq j}}^N \bar{\alpha}_{ji} \cdot \mathbf{b}_i \right]. \quad (5.15)$$

### 5.2.2 Explicit expression for matrix and vector elements

In this section, the vector addition theorem is summarized and explicit forms of matrix entries are included. The T-matrix and transition matrix are explicitly described. Also, the analytic form of  $\Re g \psi^t(k_0, 0)$  is listed.

The vector addition theorem is

$$\mathbf{M}_{lm}(k, \mathbf{r}) = \sum_{\nu=1}^{\infty} \sum_{\mu=-\nu}^{\nu} [\mathbf{M}_{\nu\mu}(k, \mathbf{r}') A_{\nu\mu,lm} + \mathbf{N}_{\nu\mu}(k, \mathbf{r}') B_{\nu\mu,lm}], \quad (5.16)$$

$$\mathbf{N}_{lm}(k, \mathbf{r}) = \sum_{\nu=1}^{\infty} \sum_{\mu=-\nu}^{\nu} [\mathbf{M}_{\nu\mu}(k, \mathbf{r}') B_{\nu\mu,lm} + \mathbf{N}_{\nu\mu}(k, \mathbf{r}') A_{\nu\mu,lm}], \quad (5.17)$$

where  $\mathbf{r} = \mathbf{r}' + \mathbf{r}''$ , and the vector wave equations are defined by (5.3)–(5.6).

The scalar wave equation,  $\Psi_{lm}(k, \mathbf{r})$  defined by (5.4), satisfies the following addition theorem

$$\Psi_{lm}(k, \mathbf{r}) = \sum_{\nu=1}^{\infty} \sum_{\mu=-\nu}^{\nu} \Psi_{\nu\mu}(\mathbf{r}') \beta_{\nu\mu,lm}. \quad (5.18)$$

Efficient recurrence relations have been derived for  $\beta_{\nu\mu,lm}$  such that it can be derived from  $\beta_{\nu\mu,00}$  [19].

The vector addition theorem can be efficiently computed if it can be related to the scalar addition theorem for which an efficient recurrence relation exists.

The  $A_{\nu\mu,lm}$  and  $B_{\nu\mu,lm}$  are related to  $\beta_{\nu\mu,lm}$  as

$$\begin{aligned} A_{\nu\mu,lm} = & \beta_{\nu\mu,lm} + r'' \sin \theta'' \frac{e^{-i\phi''}}{2(\nu+1)} \sqrt{\frac{(\nu-\mu+2)(\nu-\mu+1)}{(2\nu+1)(2\nu+3)}} \beta_{\nu+1,\mu-1,lm} \\ & - r'' \sin \theta'' \frac{e^{-i\phi''}}{2\nu} \sqrt{\frac{(\nu+\mu-1)(\nu+\mu)}{(2\nu-1)(2\nu+1)}} \beta_{\nu-1,\mu-1,lm} \\ & - r'' \sin \theta'' \frac{e^{i\phi''}}{2(\nu+1)} \sqrt{\frac{(\nu+\mu+2)(\nu+\mu+1)}{(2\nu+1)(2\nu+3)}} \beta_{\nu+1,\mu+1,lm} \\ & + r'' \sin \theta'' \frac{e^{i\phi''}}{2\nu} \sqrt{\frac{(\nu-\mu)(\nu-\mu-1)}{(2\nu-1)(2\nu+1)}} \beta_{\nu-1,\mu+1,lm} \\ & + r'' \cos \theta'' \frac{1}{\nu+1} \sqrt{\frac{(\nu+\mu+1)(\nu-\mu+1)}{(2\nu+1)(2\nu+3)}} \beta_{\nu+1,\mu,lm} \\ & + r'' \cos \theta'' \frac{1}{\nu} \sqrt{\frac{(\nu+\mu)(\nu-\mu)}{(2\nu-1)(2\nu+1)}} \beta_{\nu-1,\mu,lm}, \end{aligned} \quad (5.19a)$$

$$B_{\nu\mu,lm} = r'' \cos \theta'' \frac{i\mu}{\nu(\nu+1)} \beta_{\nu\mu,lm} + \frac{ir'' \sin \theta''}{2\nu(\nu+1)} \left[ \sqrt{(\nu-\mu)(\nu+\mu-1)} \cdot e^{i\phi''} \beta_{\nu,\mu+1,lm} + \sqrt{(\nu+\mu)(\nu-\mu-1)} e^{-i\phi''} \beta_{\nu,\mu-1,lm} \right]. \quad (5.19b)$$

The scalar translation formulas are derived by the following recurrence relations:

$$a_{lm}^+ \beta_{\nu\mu,l+1,m} = -a_{lm}^- \beta_{\nu\mu,l-1,m} + a_{\nu-1,\mu}^+ \beta_{\nu-1,\mu,lm} + a_{\nu+1,\mu}^- \beta_{\nu+1,\mu,lm}, \quad (5.20a)$$

$$b_{ll}^+ \beta_{\nu\mu,l+1,l+1} = b_{\nu-1,\mu-1}^+ \beta_{\nu-1,\mu-1,ll} + b_{\nu+1,\mu-1}^- \beta_{\nu+1,\mu-1,ll}, \quad (5.20b)$$

where

$$a_{lm}^+ = - \left[ \frac{(l+m+1)(l-m+1)}{(2l+1)(2l+3)} \right]^{\frac{1}{2}}, \quad a_{lm}^- = \left[ \frac{(l+m)(l-m)}{(2l+1)(2l-1)} \right]^{\frac{1}{2}}, \quad (5.21)$$

and

$$b_{lm}^+ = \left[ \frac{(l+m+2)(l+m+1)}{(2l+1)(2l+3)} \right]^{\frac{1}{2}},$$

$$b_{lm}^- = \left[ \frac{(l-m)(l-m-1)}{(2l+1)(2l-1)} \right]^{\frac{1}{2}}. \quad (5.22)$$

The initial values for the recurrence relations are given by

$$\beta_{00,lm} = (-1)^l \beta_{lm,00}^* = (-1)^l \sqrt{4\pi} Y_{lm}^*(\theta'', \phi'') j_n(kr''). \quad (5.23)$$

Also, it can be shown that

$$A_{\nu\mu,l,-m} = (-1)^{\mu+m} e^{-2i(\mu+m)\phi''} A_{\nu,-\mu,lm}, \quad (5.24)$$

$$A_{\nu,-\mu,l,-m} = (-1)^{\mu-m} e^{2i(\mu-m)\phi''} A_{\nu\mu,lm}, \quad (5.25)$$

and

$$B_{\nu\mu,l,-m} = (-1)^{\mu+m+1} e^{-2i(\mu+m)\phi''} B_{\nu,-\mu,lm}, \quad (5.26)$$

$$B_{\nu,-\mu,l,-m} = (-1)^{\mu-m+1} e^{2i(\mu-m)\phi''} B_{\nu\mu,lm}. \quad (5.27)$$

Because the subspheres are small compared to  $\lambda_0$ , they possess only electric dipole moments that correspond to the first three harmonics in  $\bar{\mathbf{T}}_{j(1)}$ , which will be

described later in this section. In other words, only the second term in (5.17) is considered. Therefore,  $\bar{\alpha}_{ij}$  is a  $3 \times 3$  matrix:

$$\begin{aligned} \bar{\alpha}_{ij} &= \begin{pmatrix} A_{1,-1,1,-1} & A_{10,1,-1} & A_{11,1,-1} \\ A_{1,-1,10} & A_{10,10} & A_{11,10} \\ A_{1,-1,11} & A_{10,11} & A_{11,11} \end{pmatrix} \\ &= \begin{pmatrix} \beta_{00,00} - \frac{1}{2\sqrt{5}} \beta_{20,00} & -\frac{\sqrt{3}}{2\sqrt{5}} \beta_{21,00} & -\sqrt{\frac{3}{10}} \beta_{22,00} \\ \frac{\sqrt{3}}{2\sqrt{5}} \beta_{2,-1,00} & \beta_{00,00} + \frac{1}{\sqrt{5}} \beta_{20,00} & \frac{\sqrt{3}}{2\sqrt{5}} \beta_{21,00} \\ -\sqrt{\frac{3}{10}} \beta_{2,-2,00} & -\frac{\sqrt{3}}{2\sqrt{5}} \beta_{2,-1,00} & \beta_{00,00} - \frac{1}{2\sqrt{5}} \beta_{20,00} \end{pmatrix} \end{aligned} \quad (5.28)$$

where, more explicitly,

$$A_{1,-1,1,-1} = A_{11,11} = \sqrt{4\pi} (Y_{0,0}(\theta'', \phi'') j_0(kr'') - \frac{1}{2\sqrt{5}} Y_{2,0}(\theta'', \phi'') j_2(kr'')), \quad (5.29)$$

$$A_{10,1,-1} = -A_{11,10} = \frac{\sqrt{3}}{2\sqrt{5}} \sqrt{4\pi} Y_{2,-1}(\theta'', \phi'') j_2(kr''), \quad (5.30)$$

$$A_{11,1,-1} = -\sqrt{\frac{3}{10}} \sqrt{4\pi} Y_{2,-2}(\theta'', \phi'') j_2(kr''), \quad (5.31)$$

$$A_{1,-1,10} = -A_{10,11} = -\frac{\sqrt{3}}{2\sqrt{5}} \sqrt{4\pi} Y_{2,1}(\theta'', \phi'') j_2(kr''), \quad (5.32)$$

$$A_{10,10} = \sqrt{4\pi} (Y_{0,0}(\theta'', \phi'') j_0(kr'') + \frac{1}{\sqrt{5}} Y_{2,0}(\theta'', \phi'') j_2(kr'')), \quad (5.33)$$

$$A_{1,-1,11} = -\sqrt{\frac{3}{10}} \sqrt{4\pi} Y_{2,-2}(\theta'', \phi'') j_2(kr''). \quad (5.34)$$

Therefore, there are only 6 independent elements in  $\bar{\alpha}_{ij}$ .

The T-matrix and the transmission matrix for the sphere can be found from transition coefficients and the transmission coefficients, which are given by (see [8], [21], [22])

$$t_{lm}^{TE} = \frac{\sqrt{\epsilon_s \mu_b} \hat{j}_l'(k_s a) \hat{j}_l(k_b a) - \sqrt{\epsilon_b \mu_s} \hat{j}_l(k_s a) \hat{j}_l'(k_b a)}{\sqrt{\epsilon_b \mu_s} \hat{h}_l'(k_b a) \hat{j}_l(k_s a) - \sqrt{\epsilon_s \mu_b} \hat{h}_l(k_b a) \hat{j}_l'(k_s a)}, \quad (5.35)$$

$$t_{lm}^{TM} = \frac{\sqrt{\epsilon_b \mu_s} \hat{j}_l'(k_s a) \hat{j}_l(k_b a) - \sqrt{\epsilon_s \mu_b} \hat{j}_l(k_s a) \hat{j}_l'(k_b a)}{\sqrt{\epsilon_s \mu_b} \hat{h}_l'(k_b a) \hat{j}_l(k_s a) - \sqrt{\epsilon_b \mu_s} \hat{h}_l(k_b a) \hat{j}_l'(k_s a)}, \quad (5.36)$$

$$w_{lm}^{TE} = \frac{i \mu_s \sqrt{\frac{\epsilon_s}{\mu_b}}}{\sqrt{\epsilon_b \mu_s} \hat{h}_l'(k_b a) \hat{j}_l(k_s a) - \sqrt{\epsilon_s \mu_b} \hat{h}_l(k_b a) \hat{j}_l'(k_s a)}, \quad (5.37)$$

$$w_{lm}^{TM} = \frac{i \epsilon_s \sqrt{\frac{\mu_s}{\epsilon_b}}}{\sqrt{\epsilon_s \mu_b} \hat{h}_l'(k_b a) \hat{j}_l(k_s a) - \sqrt{\epsilon_b \mu_s} \hat{h}_l(k_b a) \hat{j}_l'(k_s a)}, \quad (5.38)$$

where  $t_{lm}^{TE}$  is the transition coefficient of TE to  $r$  mode,  $t_{lm}^{TM}$  is the transition coefficient of TM to  $r$  mode,  $w_{lm}^{TE}$  is the transmission coefficient of TE to  $r$  mode, and  $w_{lm}^{TM}$  is the transmission coefficient of TM to  $r$  mode.  $\hat{j}_l(x) = x j_l(x)$ ,  $\hat{h}_l(x) = x h_l^{(1)}(x)$  and  $a$  is the radius of the sphere. Note that all of these coefficients are independent of  $m$  because the scatterer is a sphere. Moreover, we define

$$\bar{\mathbf{T}}_{lm} = \begin{pmatrix} t_{lm}^{TE} & 0 \\ 0 & t_{lm}^{TM} \end{pmatrix}, \quad (5.39)$$

$$\bar{\mathbf{w}}_{lm} = \begin{pmatrix} w_{lm}^{TE} & 0 \\ 0 & w_{lm}^{TM} \end{pmatrix}. \quad (5.40)$$

Because  $a$  is small compared to the wavelength, and the medium is nonmagnetic,  $t_{lm}^{TE}$  and  $t_{lm}^{TM}$  can be approximated as

$$t_{lm}^{TE} \sim \frac{-i(1 - \frac{\epsilon_s}{\epsilon_b})}{(2l+3)[1 \cdot 3 \cdot \dots \cdot (2l+1)]^2} (k_b a)^{(2l+3)}, \quad \text{as } k_b a \rightarrow 0 \text{ and } \mu_s = \mu_b, \quad (5.41)$$

$$t_{lm}^{TM} \sim \frac{-i(l+1)(2l+1)(1 - \frac{\epsilon_s}{\epsilon_b})}{[1 \cdot 3 \cdot \dots \cdot (2l+1)]^2 [1 + (l+1) \frac{\epsilon_s}{\epsilon_b}]} (k_b a)^{(2l+1)}, \quad \text{as } k_b a \rightarrow 0 \text{ and } \mu_s = \mu_b. \quad (5.42)$$

Clearly, the electric dipole terms ( $t_{lm}^{TM}$ ,  $l = 1$  and  $m = \pm 1$ ) are sufficient for characterizing small dielectric spheres.

To find the internal field by (5.15),  $\Re g\psi^t(k_0, 0)$  can be calculated by (5.2)–(5.6). Using the small argument approximation [28],  $\Re g\psi^t(k_0, 0)$  can be explicitly written as

$$\Re g\psi^t(k, 0) = [\Re g\mathbf{M}_{lm}(k, 0) \quad \Re g\mathbf{N}_{lm}(k, 0)], \quad (5.43)$$

where

$$\Re g\mathbf{M}_{lm}(k, 0) = 0, \quad \text{for any } l \text{ and } m, \quad (5.44)$$

$$\Re g\mathbf{N}_{lm}(k, 0) = 0, \quad l \neq 1, \quad (5.45a)$$

and

$$\Re g\mathbf{N}_{1,\pm 1}(k, 0) = \frac{2}{3}\sqrt{\frac{3}{8\pi}}(\pm\hat{x} - i\hat{y}) \quad \Re g\mathbf{N}_{1,0}(k, 0) = \frac{2}{3}\sqrt{\frac{3}{4\pi}}\hat{z}. \quad (5.45b)$$

### 5.3 BiCGFFT Implementation

Equation (5.13) can be solved with iterative methods such as the bi-conjugate gradient (BiCG) method introduced in Chapter 2. It is well known that CG-type methods converge to the solution in at most  $N$  iterations under exact arithmetics [13], [14], [27] and generally can achieve enough accuracy in many fewer iterations than  $N$ . Also, in most cases, the BiCG method converges faster than the CG method because the former deals with the matrix equation directly instead of the normal equation implied in the latter, in which the condition number has been squared.

In such a method, the major computational cost would be in the matrix-vector multiplication  $\bar{\mathbf{A}} \cdot \mathbf{B}$ . For a dense matrix, the cost of such a matrix-vector multiplication requires  $O(N^2M^2)$  operations, where  $M$  is the dimension of the  $\bar{\alpha}_{ij}$  matrices and is equal to 3 as discussed in Section 5.2.2.

When the scattering centers are placed on a regular grid, then  $\bar{\alpha}_{ij} = \bar{\alpha}(\mathbf{r}'_i - \mathbf{r}'_j)$ . The translation matrix is only a function of  $\mathbf{r}'_i - \mathbf{r}'_j$  as illustrated by (5.28)–(5.34). When the formulation is implemented, the summation in Equation (5.12) is actually

replaced with a three-dimensional summation. In such a case,  $\bar{\mathbf{A}}$  can be expressed as a block-Toeplitz matrix. In one dimension, it appears as

$$\bar{\mathbf{A}} = \begin{pmatrix} \bar{\alpha}_0 & \bar{\alpha}_{-1} & \dots & \bar{\alpha}_{1-n} \\ \bar{\alpha}_1 & \bar{\alpha}_0 & \dots & \bar{\alpha}_{2-n} \\ \vdots & \vdots & \ddots & \vdots \\ \bar{\alpha}_{n-1} & \bar{\alpha}_{n-2} & \dots & \bar{\alpha}_0 \end{pmatrix}, \quad (5.46)$$

where  $\bar{\alpha}_m = \bar{\alpha}_{ij}$ , as  $i - j = m$ . By grouping the elements of same harmonics into one block, the block-Toeplitz matrix is converted to a Toeplitz-block matrix (i.e., each block is Toeplitz). Because  $\bar{\alpha}_m$  is a  $3 \times 3$  matrix, (5.46) can be permuted into

$$\bar{\mathbf{A}} = \begin{pmatrix} \bar{\mathbf{A}}_{-1,-1} & \bar{\mathbf{A}}_{-1,0} & \bar{\mathbf{A}}_{-1,1} \\ \bar{\mathbf{A}}_{0,-1} & \bar{\mathbf{A}}_{0,0} & \bar{\mathbf{A}}_{0,1} \\ \bar{\mathbf{A}}_{1,-1} & \bar{\mathbf{A}}_{1,0} & \bar{\mathbf{A}}_{1,1} \end{pmatrix}, \quad (5.47)$$

where each  $\bar{\mathbf{A}}_{m,n}$  is a Toeplitz matrix.

The fast Fourier transform (FFT) method can then be used to expedite the matrix-vector multiply,  $\bar{\mathbf{A}} \cdot \mathbf{B}$  with an operation count of  $O(NM \log N)$ .

If the spheres are small compared to  $\lambda_0$ , they possess only electric dipole moments that correspond to the first three harmonics in  $\bar{\mathbf{T}}_{j(1)}$ . Therefore,  $M = 3$ , and furthermore, there are only 6 independent elements in the  $3 \times 3$  matrix  $\bar{\alpha}_{ij}$ , due to the rotational symmetry.

To perform the matrix-vector multiply more efficiently,  $\bar{\mathbf{A}}$  is first extended to a circulant matrix in the  $x$ -,  $y$ - and  $z$ -directions to obtain  $\bar{\mathbf{A}}'$ . Then the Fourier transform of any column of  $\bar{\mathbf{A}}'$ ,  $\tilde{\mathbf{A}}$  is calculated only once outside the iteration loop and stored. Also, zeros have to be padded to the original vector to prevent aliasing. Hence, whenever a matrix-vector multiply is required in each iteration, three forward 3D-FFT's corresponding to three harmonics are first performed, then they are multiplied by  $\tilde{\mathbf{A}}$  in the frequency domain and, finally, three inverse 3D-FFT's are accomplished. Then the product can be obtained by discarding those entries with zero padding in the first place. An illustrative example of this procedure in one dimension can be seen in Chapter 2.

The memory requirement of the method is still  $O(N)$  because each block matrix in  $\overline{\mathbf{A}}$  can be represented by one of its rows or columns.

#### 5.4 Numerical Results

In Figure 5.3, a dielectric layered sphere is considered. This sphere is approximated by a cluster of small cubes. For those cubes that lie astride two different media, they are assigned to either medium according to whether the center of the cube is inside the spherical interface or not. Then all of the cubes are replaced with equivolume spheres. The incident field is a uniform plane wave impinging from the  $+z$  axis and with  $x$  polarization. The BiRCS, near field and the internal field results have been shown in Figure 5.3(a)-(c) and they all agree well with the Mie series solutions. The BiRCS is defined as

$$BiRCS(\phi, \theta) = 10 \log(\sigma_\infty(\phi, \theta)) - 10 \log(\lambda_0^2) \quad dB,$$

where

$$\sigma_\infty(\phi, \theta) = \lim_{R \rightarrow \infty} 4\pi R^2 \frac{\|\mathbf{E}^s(\phi, \theta)\|^2}{\|\mathbf{E}^i(\phi, \theta)\|^2}$$

and in which  $\mathbf{E}^s(\phi, \theta)$  and  $\mathbf{E}^i(\phi, \theta)$  denote the scattered field and incident field vectors, respectively. The algorithm converges in 53 iterations for the case in Figure 5.3 and takes about 1.5 hours of CPU time on a SPARC 10 workstation (10 MFLOPS machine) working in double precision.

A good agreement is also observed in Figure 5.4 for a dielectric cube [12]. Figure 5.5 shows the number of iterations versus the number of unknowns for lossless and lossy objects. As we have observed in 2D cases [20], the number of iterations increases with the size of the object and in the lossy medium, fewer iterations are required to converge than for the lossless medium. This shows that in the lossy medium, the complex permittivity shifts the otherwise small eigenvalues in the lossless medium away from the origin. Physically, the resonant frequencies of the lossy dielectric body are complex, while in practice, the operating frequency is always real, which precludes the eigenvalues from being too close to zero.

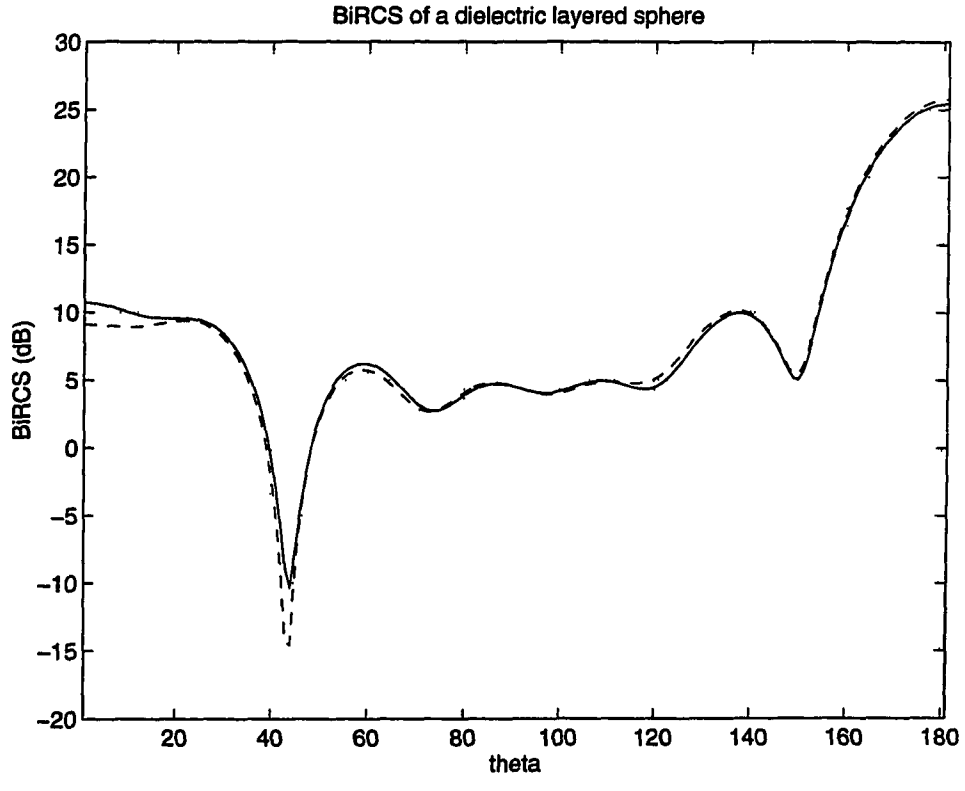
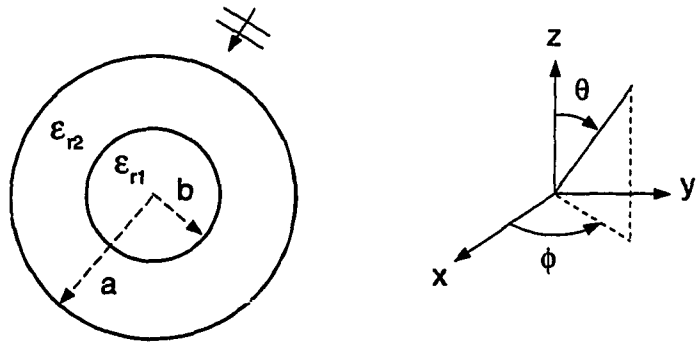


**Figure 5.3(a).** The BiRCS of a spherically layered sphere. The solid line is from the Mie series solution; the dashed line is the numerical solution. Here,  $b = 0.5\lambda_0$ ,  $\epsilon_{r1} = 1.2$ ,  $a = 1.0\lambda_0$  and  $\epsilon_{r2} = 2.4$ . A  $30 \times 30 \times 30$  grid is used.

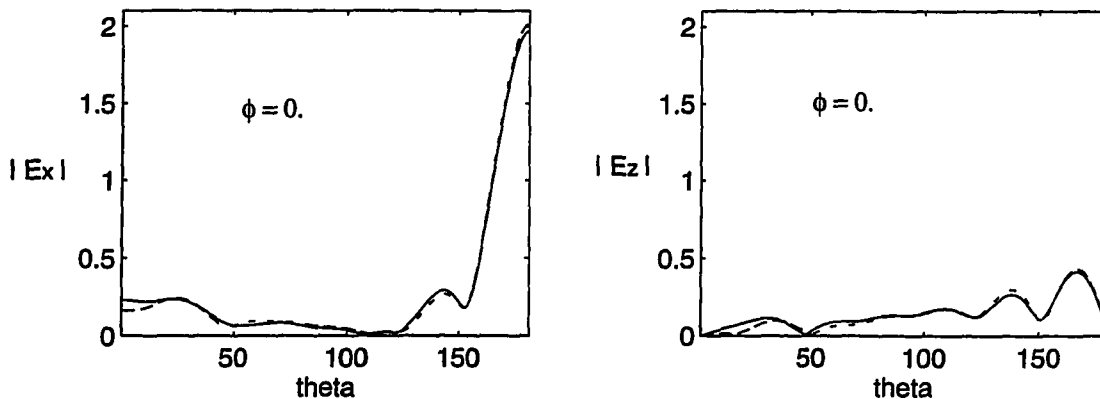


**Figure 5.3(b).** The near fields of the spherically layered sphere. The observation points are  $3\lambda_0$  away from the center. The solid line and dashed line denote the Mie series solution and numerical solution, respectively.

The number of iterations is approximately proportional to  $N$  for lossless objects and seemingly to  $N^{0.75}$  for lossy ones when  $N$  is large. Without preconditioners, the eigenvalue distribution seems dispersive without confinement as  $N$  grows and the erratic convergence of BiCG algorithm worsens the already poor condition number. In order for BiCG-FFT or its like to be more favorable, a suitable preconditioner is necessary.

Finally, we demonstrate that when the object is gridded finer, the T-matrix formulation is still stable. The first example is a homogeneous dielectric sphere with  $\epsilon_r = 4.0$  and the radius  $= 10^{-5}\lambda_0$ . The simulation results show that the number of iterations remains as 6 for the cases of  $8 \times 8 \times 8$ ,  $16 \times 16 \times 16$  and  $32 \times 32 \times 32$  grids. Figure 5.6 shows one of the results, and it agrees very well with the exact solution. We have also run a second example (not shown here), which is a homogeneous dielectric cube with  $\epsilon_r = 9.0$  and the side length  $= 0.34\lambda_0$ . Similar to the first example, the number of iterations is 16 for all three different grids as mentioned above.

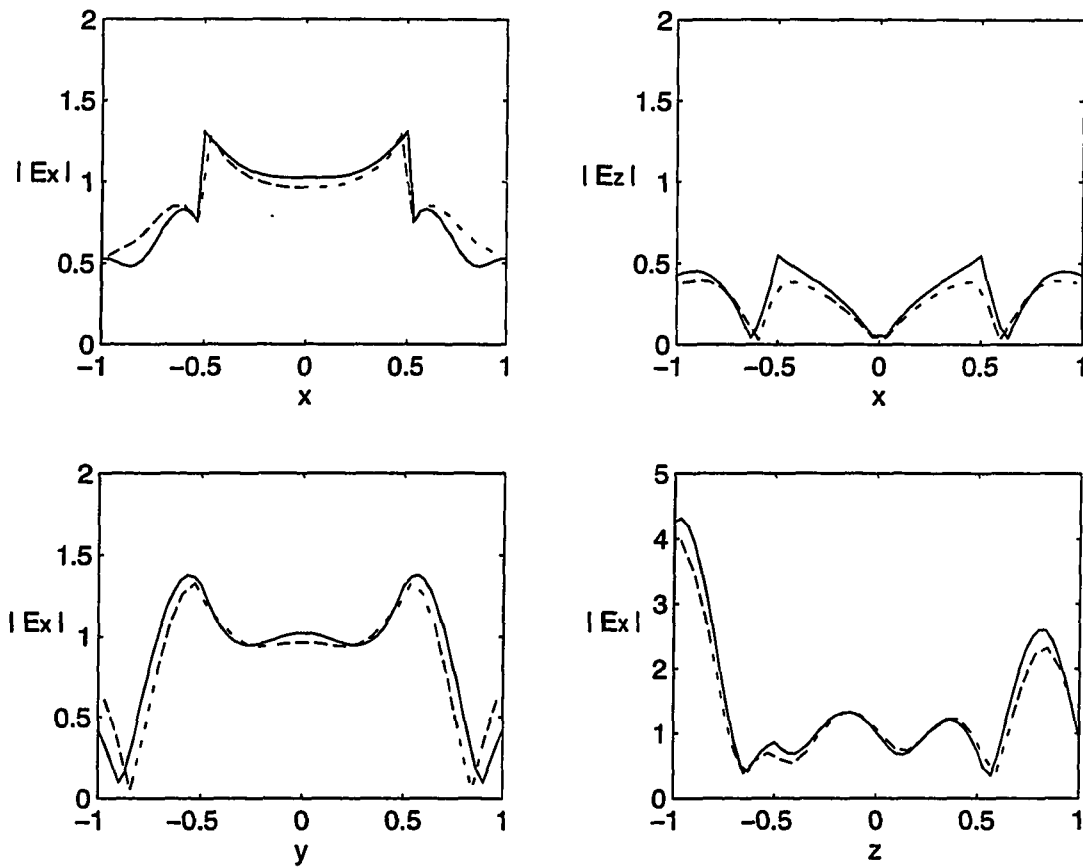
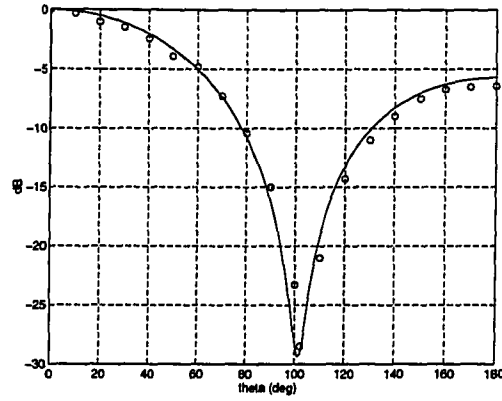


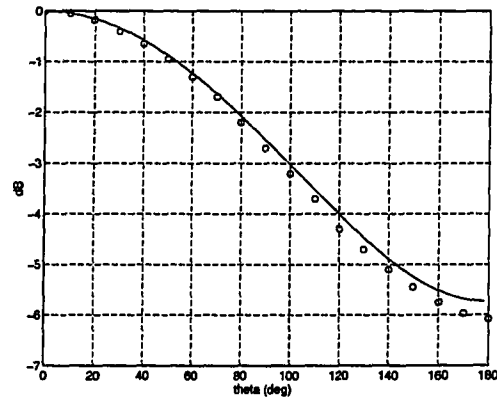
**Figure 5.3(c).** Different components of the internal fields of the spherically layered sphere are calculated at the  $x$ ,  $y$ , and  $z$  axes by the Mie series (solid lines) and the algorithm (dashed lines).

$$\phi = 0^\circ$$



(a) The far field  $\|\mathbf{E}_\theta\|$  as a function of  $\theta$

$$\phi = 90^\circ$$



(b) The far field  $\|\mathbf{E}_\phi\|$  as a function of  $\theta$

**Figure 5.4.** The far fields as a function of  $\theta$  computed for a lossless dielectric cube with  $\epsilon_r = 9$  and  $k_0 a = 0.628319$ . The solid lines represent the results by the BiCG-FFT T-matrix method, and the symbols  $\circ$  represent the results by Zwamborn and van den Berg [12]. A  $7 \times 7 \times 7$  grid is used.

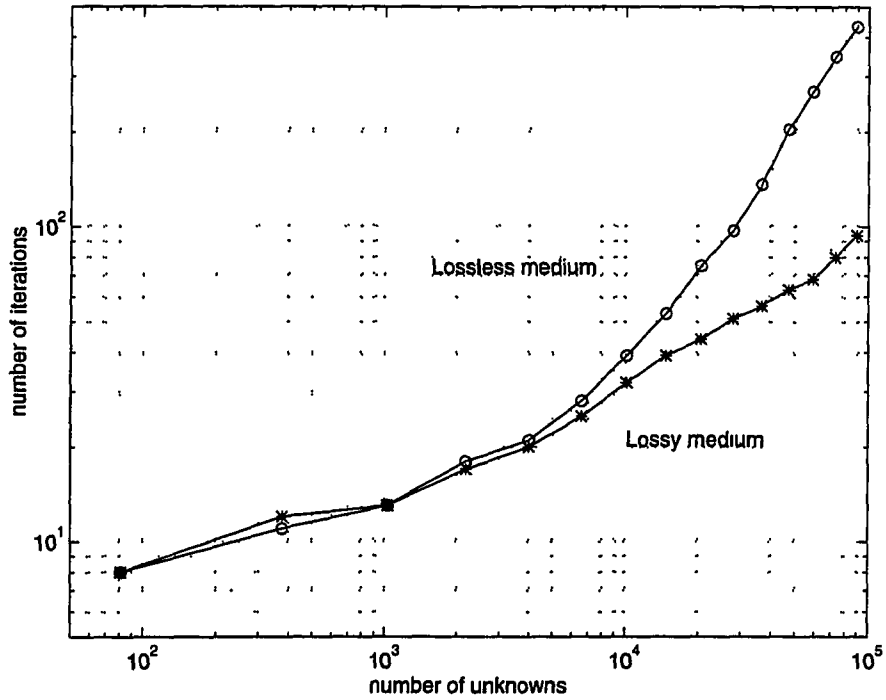


**Figure 5.5.** The number of iterations vs. the number of unknowns for lossless cubes of  $\epsilon_r = 9.0$  and for lossy cubes of  $\epsilon_r = 9.0 + i3.0$ .

## 5.5 Conclusions

A BiCG-FFT T-matrix algorithm has been developed to efficiently solve three-dimensional scattering problems of inhomogeneous bodies. The memory storage is of  $O(N)$  ( $N$  is the number of unknowns), and each iteration in BiCG requires  $O(N \log N)$  operations. Both the internal field and scattered field can be calculated via this algorithm.

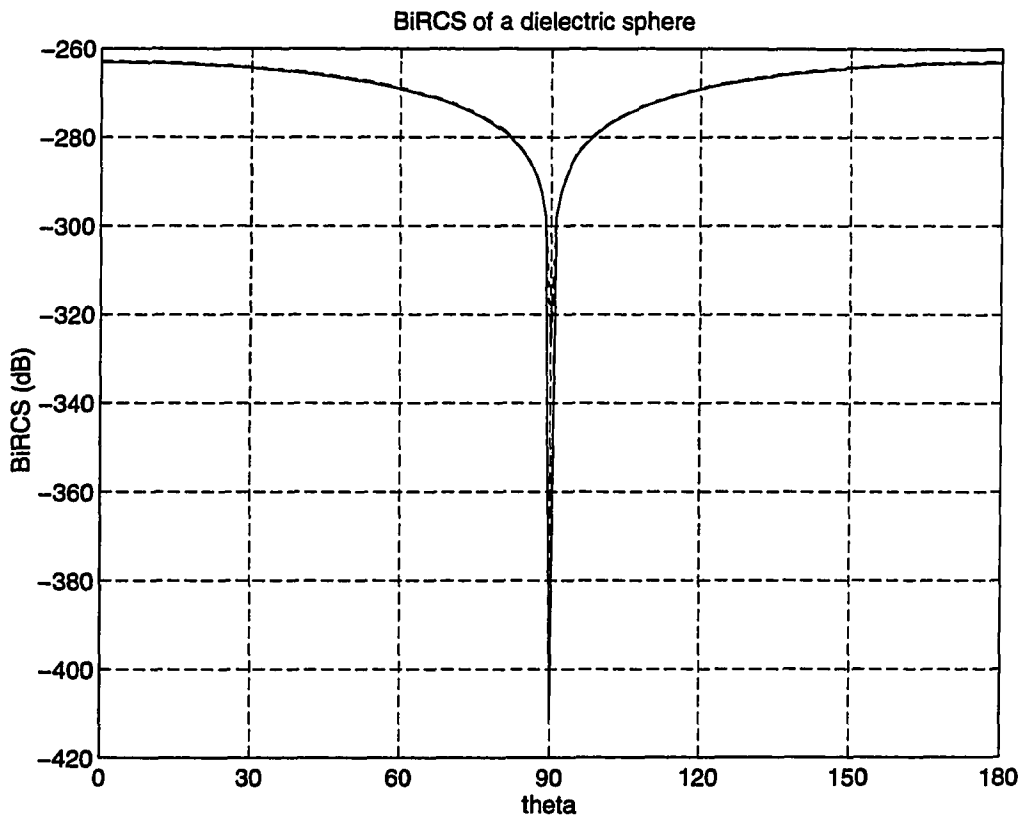
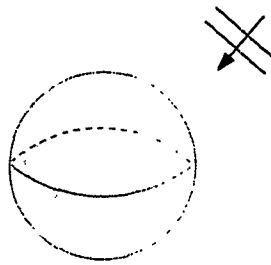


**Figure 5.6.** The BiRCS of a dielectric sphere. The solid line is from the Mie series solution; the dashed line is the numerical solution. Here, the radius =  $10^{-5}\lambda_0$  and  $\epsilon_r = 4.0$ . A  $16 \times 16 \times 16$  grid is used.

This algorithm can also be applied to scattering from a cluster of randomly located discrete scatterers [29].

The T-matrix formulation avoids the Green's function singularity problem. In order for BiCG-FFT or its like to be more favorable, a suitable preconditioner is necessary, especially for large-size and high-contrast problems.

The numerical results demonstrate that the matrix condition number for fine grids is the same as that for coarse grids. This phenomenon can also be observed in other integral equation formulations. Hence, high resolution can be achieved without changing the condition number.

## 5.6 References

- [1] J. H. Richmond, "Scattering by a dielectric cylinder of arbitrary cross section shape," *IEEE Trans. Antennas Propag.*, vol. 13, no. 5, pp. 334-341, May 1965.
- [2] D. E. Livesay and K. M. Chen, "Electromagnetic fields induced inside arbitrarily shaped biological bodies," *IEEE Trans. Microwave Theory Tech.*, vol. 22, no. 12, pp. 1273-1280, 1974.
- [3] T. C. Guo and W. W. Guo, "Scattering of vector waves by arbitrary three-dimensional dielectric objects," *Proceedings of the 1987 International Microwave Symposium*, pp. 307-312, Rio de Janeiro, Brazil, July 1987.
- [4] T. C. Guo, W. W. Guo, and H. N. Oguz, "A technique for three-dimensional dosimetry and scattering computation of vector electromagnetic fields," *IEEE Trans. Magnetics*, vol. 29, no. 2, pp. 1636-1641, 1993.
- [5] T. C. Guo and W. W. Guo, "A matrix formulation of dielectric imaging, dosimetry and computation of vector electromagnetic field," *Proceedings of the Fifth Biennial IEEE Conference in Electromagnetic Field Computation*, pp. 413-423, Monterey, CA, 22-26 March 1993.
- [6] Y. M. Wang and W. C. Chew, "A recursive T-matrix approach for the solution of electromagnetic scattering by many spheres," *IEEE Trans. Antennas Propag.*, vol. 41, no. 12, pp. 1633-1639, December 1993.
- [7] P. C. Waterman, "Matrix formulation of electromagnetic scattering," *Proc. IEEE*, vol. 53, pp. 805-811, 1965.

- [8] W. C. Chew, *Waves and Fields in Inhomogeneous Media*. New York: Van Nostrand Reinhold, 1990.
- [9] R. H. Harrington, *Field Computations by Moment Methods*. New York: McGraw-Hill, 1968.
- [10] D. T. Borup and O. P. Gandhi, "Fast-Fourier transform method for the calculation of SAR distribution in finely discretized models of biological bodies," *IEEE Trans. Microwave Theory Tech.*, vol. 32, no. 4, pp. 355-360, 1984.
- [11] C. Y. Shen, K. J. Glover, M. I. Sancer, and A. D. Varvatsis, "The discrete Fourier transform method of solving differential-integral equations in scattering theory," *IEEE Trans. Antennas Propag.*, vol. 37, no. 8, pp. 1032-1041, 1989.
- [12] A. P. M. Zwamborn and P. M. van den Berg, "The three-dimensional weak form of the conjugate gradient FFT method for solving scattering problems," *IEEE Trans. Microwave Theory Tech.*, vol. 40, no. 9, pp. 1757-1766, 1992.
- [13] M. R. Hestenes and E. Stiefel, "Methods of conjugate gradient for solving linear systems," *J. Res. Natl. Bur. Stand.*, vol. 49, pp. 409-435, 1952.
- [14] O. Axelsson and V. A. Barker, *Finite Element Solution of Boundary Value Problems: Theory and Computation*. New York: Academic Press, 1984.
- [15] C. Lanczos, "An iteration method for the solution of the eigenvalue problem of linear differential and integral operators," *J. Res. Nat. Bur. Stand.*, vol. 45, pp. 255-282, 1950.
- [16] R. Fletcher, "Conjugate gradient methods for indefinite systems," in *Numerical Analysis Dundee 1975*, G. A. Watson, Ed. New York: Springer-Verlag, 1976, pp. 73-89.
- [17] T. K. Sarkar, "On the application of the generalized bi-conjugate gradient method," *J. Electromagn. Waves Appl.*, vol. 1, no. 3, pp. 223-242, 1987.
- [18] M. F. Cátedra, J. G. Cuevas, and L. Nuño, "A scheme to analyze conducting plates of resonant size using the conjugate-gradient method and the fast Fourier transform," *IEEE Trans. Antennas Propagat.*, vol. 36, no. 12, pp. 1744-1752, 1988.
- [19] W. C. Chew, "Recurrence relation for three dimensional scalar addition theory," *J. Electromagn. Waves Appl.*, vol. 6, no. 2, pp. 133-142, 1992.
- [20] J.-H. Lin and W. C. Chew, "A comparison of the CG-FFT method and the recursive aggregate T-matrix algorithm," in *IEEE Antennas and Propagation Society International Symposium Digest*, pp. 1591-1594, 1992.

- [21] R. F. Harrington, *Time-Harmonic Electromagnetic Fields*. New York: McGraw-Hill, 1961.
- [22] J. A. Kong, *Electromagnetic Wave Theory*. New York: John Wiley & Sons, 1986.
- [23] J. A. Stratton, *Electromagnetic Theorem*. New York: McGraw-Hill, 1941.
- [24] A. Messiah, *Quantum Mechanics*. Amsterdam: North-Holland Publishing Company, 1958.
- [25] W. C. Chew and Y. M. Wang, "Efficient ways to compute the vector addition theorem," *J. Electromag. Waves Appl.*, vol. 7, no. 5, pp. 651-665, May 1993.
- [26] R. C. Wittmann, "Spherical wave operators and the translation formulas," *IEEE Trans. Antennas Propag.*, vol. 36, no. 8, pp. 1078-1087, 1988.
- [27] G. H. Golub and C. F. Van Loan, *Matrix Computations*, 2nd ed. Baltimore: John Hopkins University Press, 1989.
- [28] M. Abramowitz and I. A. Stegun, *Handbook of Mathematical Functions*. New York: Dover Publications, 1965.
- [29] W. C. Chew, J.-H. Lin and X. G. Yang, "An FFT T-matrix method for 3D electromagnetic scattering solutions from random discrete scatterers," *Microw. Opt. Tech. Lett.*, vol. 9, no. 4, pp. 194-196, July 1995.

## CHAPTER 6

### ULTRASONIC IMAGING BY LOCAL SHAPE FUNCTION WITH CGFFT

#### 6.1 Introduction

The use of scattered electromagnetic and acoustic waves to determine the internal material properties of objects is a much-studied problem in the fields of geophysics, nondestructive evaluation, sonar, and medical imaging. The potential of ultrasound as a diagnostic tool was recognized as early as the late 1940s. Wild and Reid's work [1] demonstrated that tissue pathology might be characterized by echoes reflected or scattered back from internal structures of the tissue. They laid the foundation for much of the tissue characterization research that blossomed in the 1970s, which remains an area of active research of paramount interest to many scientists in the world [2], [3]. In the early stage, despite the fact that techniques are primitive and only very limited information in echoes is available to clinicians, they have been able to characterize the tissue in certain cases, which illustrates well the potential of ultrasound for tissue characterization.

Thus far, most wave-equation inversion methods for ultrasonic imaging have used diffraction tomography approaches: linearizations obtained by first-order perturbation approximation of the wave equation. The Born and Rytov methods [4]-[12] belong in this category. The Born approximation is obtained by first-order approximation of the Helmholtz equation. Similarly, the Rytov method is derived from first-order approximation of the Ricatti equation. Both methods, while numerically efficient, have not proven to be accurate enough for realistic tissue imaging.

On the other hand, directly applying nonlinear iteration methods to the equation uses no simplifying linearization. It properly includes all diffraction and refraction effects. The disadvantage is, of course, the numerical complexity and cost of such methods. Recent improvements in the numerical efficiency of our algorithms suggest that this limitation may be surmountable.

Considering the lack of knowledge regarding the three-dimensional architecture of tissue, the inhomogeneous continuum model for scattering process is probably the most realistic choice at this point in time [13]. In this model, a fluid is assumed to be a continuous medium characterized by steady values of density and compressibility, but in addition containing inhomogeneities of differing equilibrium densities and/or compressibility from which scattering of acoustic waves takes place.

A differential equation used to model ultrasound propagation through tissues can be described as [14]

$$\rho \nabla \cdot \rho^{-1} \nabla p + k^2 p = 0, \quad (6.1)$$

where  $\rho$  is the medium density as a function of position and the wave number  $k^2 = \omega^2 \rho (\kappa + i \frac{\gamma}{\omega})$ , where  $\kappa$  and  $\gamma$  are the medium compressibility and absorption factor, respectively. By a change of variable, the above equation can be converted into the Helmholtz wave equation:

$$\nabla^2 f + \left( k^2 - \sqrt{\rho} \nabla^2 \frac{1}{\sqrt{\rho}} \right) f = 0, \quad (6.2)$$

where  $f = p/\sqrt{\rho}$  and the parenthesized term can be viewed as a scattering potential. Most nonlinear iteration methods are concentrated on (6.2) to reconstruct the scattering potential [15]-[20] instead of on (6.1) to extract both  $\rho$  and  $\kappa$  simultaneously [21].

Because the acoustic wave Equation (6.1) has a one-to-one correspondence to the electromagnetic wave equation for  $H_z$  polarization in two dimensions, we can formulate the problem in exactly the same fashion as in [22]. The forward model is essentially the replica of that mentioned in Section 5.2, but for two dimensions. However, the matrix and vector elements assume much simpler forms, which will be detailed in Section 6.2.

In Section 6.3, as in Chapter 3, inverse scattering problems are reposed as optimization problems. By way of iteratively updating the sought parameters, the difference between real data and calculated data keeps decreasing. One way to

reduce the difference iteratively is to employ the conjugate gradient minimization scheme. In each iteration, one finds the gradient of the functional to determine the updating direction and calculate the Hessian to determine the step size along the conjugate vector. Then, one calculates the scattered field due to the new update. Another way is to equate the gradient to zero to find the extremum in each iteration. The resultant nonlinear equation is then linearized and solved for the new parameters. Both approaches utilize the distorted Born method to expedite the convergence rate.

The implementation of the local shape function (LSF) method will be introduced in Section 6.4. Mainly, CGFFT is employed to solve for scattering amplitudes for different insonifications and for different receiving locations in view of back propagation.

In Section 6.5, some reconstruction results are presented. They include synthetic data, and real data provided by ThermoTrex Corporation in San Diego. Simulation results indicate that the single-frequency reconstruction is not sufficient to obtain good images; the multiple-frequency scheme can produce better reconstruction quantitatively. An alternative to the multiple-frequency scheme is the frequency-hopping method, which was mentioned in Chapter 3 and is utilized in this chapter as well. A reconstruction area as large as  $18\lambda \times 18\lambda$  is considered. The reconstructed image shows the exterior boundary of a boiled egg and its yolk within. Also, a tiny structure inside the egg can be identified. Finally, some conclusions are drawn in the last section.

## 6.2 Forward Model by T-Matrix Method

The formulation is exactly the same as described in Section 5.2. In what follows, we summarize some final results for later reference and explicitly list necessary matrix and vector elements.

The scattered field due to  $N$  subscatterers can be expressed as

$$\Phi^{sca} = \bar{\Psi}^t \cdot \mathbf{a}, \quad (6.3)$$

where  $\mathbf{a}$  contains scattering amplitudes for each subscatterer, which has three elements corresponding to the -1st, 0th and 1st harmonics when the subscatterer is small compared to the wavelength.  $\bar{\Psi}^t$  contains the cylindrical wave functions between the subscatterer and the receiver. Its elements can be written as

$$[\bar{\Psi}^t]_{l,mn} = H_l^{(1)}(k_0 r_{mn}) e^{il\theta_{mn}}, \quad l = -1, 0, 1, \quad (6.4)$$

where  $r_{mn}$  and  $\theta_{mn}$  denote the distance and angle from  $m$ -th subscatterer to the  $n$ -th receiver.  $k_0$  is the wave number of the homogeneous background.

According to (6.1), the scattered field can be derived as [14], [23].

$$\phi^{sca}(\mathbf{r}) = \int_V [k_0^2 \gamma_\kappa(\mathbf{r}') \phi(\mathbf{r}') g(k_0; \mathbf{r}, \mathbf{r}') + \gamma_\rho(\mathbf{r}') \nabla' \phi(\mathbf{r}') \cdot \nabla' g(k_0; \mathbf{r}, \mathbf{r}')] d\mathbf{r}', \quad (6.5)$$

where  $\gamma_\kappa = (\kappa - \kappa_0)/\kappa_0$  and  $\gamma_\rho = (\rho - \rho_0)/\rho$ ;  $g(k_0; \mathbf{r}, \mathbf{r}')$  is the free space Green's function, which is  $H_0^{(1)}(k_0 |\mathbf{r} - \mathbf{r}'|)$  in two dimensions;  $\phi(\mathbf{r}')$  is the total field inside the scatterer. The first term in the bracket accounts for the monopole radiation, while the second term represents the dipole radiation. Therefore, it is justified that only the first three harmonics in (6.4) are sufficient to describe the scattering behavior of each subscatterer.

Furthermore,  $\mathbf{a}$  can be expressed as

$$\mathbf{a} = (\bar{\mathbf{I}} - \bar{\mathbf{T}} \cdot \bar{\mathbf{A}})^{-1} \cdot \bar{\mathbf{T}} \cdot \bar{\mathbf{B}} \cdot \mathbf{e}, \quad (6.6)$$

where  $\bar{\mathbf{I}}$  is identity matrix,  $\bar{\mathbf{T}}$  the T-matrix,  $\bar{\mathbf{A}}$  the translation matrix among the subscatterers, and  $\bar{\mathbf{B}}$  the translation matrix between the source and the subscatterers and  $\mathbf{e}$  the vector of incident field amplitudes. If the subscatterer is replaced with an equal-area circle [24],  $\bar{\mathbf{T}}$  becomes a diagonal matrix and can be denoted as  $\bar{\mathcal{D}}(\mathbf{O})$ , where  $\bar{\mathcal{D}}$  converts a vector into a square diagonal matrix and the transition

coefficients in  $\mathbf{O}$  can be found as [25], [26]

$$[\mathbf{O}]_{l,m} = \frac{k_0 \rho_m J_l(k_m a) J_l'(k_0 a) - k_m \rho_0 J_l'(k_m a) J_l(k_0 a)}{k_m \rho_0 J_l'(k_m a) H_l^{(1)}(k_0 a) - k_0 \rho_m J_l(k_m a) H_l^{(1)'}(k_0 a)},$$

$$l = -\infty, \dots, \infty, \quad m = 1, \dots, N, \quad (6.7)$$

where  $k_m = \omega \sqrt{\rho_m \kappa_m}$ ,  $a$  is the circle radius and  $N$  is the number of grid cells. Note that  $[\mathbf{O}]_{lm} = [\mathbf{O}]_{-lm}$ . Because  $a$  is small compared to  $\lambda_0$  or  $k_0 a \rightarrow 0$ , (6.7) can be reduced to

$$[\mathbf{O}]_{l,m} \sim \begin{cases} \frac{i\pi}{4} (k_0 a)^2 \left( \frac{\kappa_m}{\kappa_0} - 1 \right), & \text{for } l = 0 \\ \frac{i\pi}{4^l l! (l-1)!} (k_0 a)^{2l} \frac{\rho_m - \rho_0}{\rho_m + \rho_0}, & \text{for } l = 1, 2, \dots \end{cases} \quad (6.8)$$

Apparently, the first three harmonics,  $l = 0, \pm 1$  are sufficient to characterize the small circle, which once again fortifies (6.4). Once  $[\mathbf{O}]_{l,m}$  has been reconstructed,  $\kappa_m$  and  $\rho_m$  can be found through

$$\kappa_m = \kappa_0 (1 + c [\mathbf{O}]_{0,m}) \quad \text{and} \quad \rho_m = \frac{1 + c [\mathbf{O}]_{1,m}}{1 - c [\mathbf{O}]_{1,m}}, \quad (6.9)$$

where the constant  $c = \frac{4}{i\pi (k_0 a)^2}$ .

By the addition theorem, elements in  $\overline{\mathbf{A}}$  can be expressed as

$$[\overline{\mathbf{A}}]_{kl,mn} = \begin{cases} 0, & \text{if } m = n \\ H_{k-l}^{(1)}(k_0 r_{mn}) e^{-i(k-l)\theta_{mn}}, & \text{otherwise.} \end{cases} \quad (6.10)$$

In the implementation, the subscatterers are not numbered in serial order as implied in the above equations, but are kept in their original grid setup. Therefore, for each subscatterer, there should be two indices in the  $x$  and  $y$  directions to describe its position. In this way,  $\overline{\mathbf{A}}$  is a block-Toeplitz matrix. By grouping the elements of the same harmonics into one block, the block-Toeplitz matrix is converted to a Toeplitz-block matrix, which facilitates the FFT implementation.

Similarly, elements in  $\overline{\mathbf{B}}$  can be written as

$$[\overline{\mathbf{B}}]_{kl,m} = J_{l-k}(k_0 r_m) e^{-i(l-k)(\theta_m + \pi)},$$

$$k = -P, \dots, P, \quad l = -1, 0, 1, \quad m = 1, \dots, N, \quad (6.11)$$

where  $P$  depends on the object size and is proportional to  $\sqrt{N}$  in two dimensions.

For the monopole illumination of a line source,  $\mathbf{e}$  can be found by

$$H_0^{(1)}(k_0|\mathbf{r} - \mathbf{r}_s|) = \sum_k H_k^{(1)}(k_0r_s)e^{-ik\theta_s} J_k(k_0r)e^{ik\theta} \quad \text{as } r_s > r. \quad (6.12)$$

Thereby,

$$[\mathbf{e}]_k = H_k^{(1)}(k_0r_s)e^{-ik\theta_s}. \quad (6.13)$$

Sometimes both the transmitting and the receiving patterns are dipole radiation patterns. Then,  $\mathbf{e}$  and  $\bar{\Psi}^t$  have to be modified. It is known that a dipole is equivalent to two monopoles with opposite charges of infinite  $Q$  and displaced by a infinitesimal  $\delta$ . The dipole field can be expressed as

$$\begin{aligned} \Phi^i(\mathbf{r}) &= QH_0^{(1)}(k_0|\mathbf{r} - (\mathbf{r}_s + \delta\hat{r}_s)|) - QH_0^{(1)}(k_0|\mathbf{r} - (\mathbf{r}_s - \delta\hat{r}_s)|) \\ &\approx Q[H_0^{(1)}(k_0r_1) - k_0\delta\hat{r}_s \cdot \hat{r}_1 H_0^{(1)'}(k_0r_1)] - Q[H_0^{(1)}(k_0r_1) + k_0\delta\hat{r}_s \cdot \hat{r}_1 H_0^{(1)'}(k_0r_1)] \\ &= 2k_0\delta Q\hat{r}_s \cdot \hat{r}_1 H_1^{(1)}(k_0r_1), \end{aligned} \quad (6.14)$$

where  $\mathbf{r}$ ,  $\mathbf{r}_s$  and  $\mathbf{r}_1$  are denoted as in Figure 6.1(a). By identifying that  $\hat{r}_s \cdot \hat{r}_1 = \frac{1}{2}[e^{i(\theta_1 - \theta_s)} + e^{-i(\theta_1 - \theta_s)}]$  and using the addition theorem to expand the cylindrical harmonics,  $H_{\pm 1}^{(1)}(k_0r_1)e^{i\theta_1}$ , (6.13) can be written as

$$\Phi^i(\mathbf{r}) \approx 2k_0\delta Q \sum_k H_k^{(1)'}(k_0r_s)e^{-ik_0\theta_s} J_k(k_0r)e^{ik\theta}. \quad (6.15)$$

Accordingly,

$$[\mathbf{e}]_k = H_k^{(1)'}(k_0r_s)e^{-ik_0\theta_s}. \quad (6.16)$$

Because each subscatterer has three components in scattering amplitudes (-1st, 0th and 1st harmonics),  $\bar{\Psi}^t$  is more complicated than the transmitting part. For the 0th component, in the same manner as above, we obtain

$$\Phi_0^r(\mathbf{r}_n) \approx -2k_0\delta Q\hat{r}_n \cdot \hat{r}_{mn} H_1^{(1)}(k_0r_{mn}), \quad (6.17)$$

where  $\mathbf{r}_n$  denotes the  $n$ -th receiver location and  $\mathbf{r}_{mn} = \mathbf{r}_n - \mathbf{r}_m$ .  $\mathbf{r}_m$  is the position

vector of the  $m$ -th subscatterer. Referring to Figure 6.1(b) and by the first-order approximation,

$$\begin{aligned}\Phi_1^r(\mathbf{r}_n) &= QH_1^{(1)}(k_0r_{mn+})e^{i\theta_{mn+}} - QH_1^{(1)}(k_0r_{mn-})e^{i\theta_{mn-}} \\ &\approx 2k_0\delta Q[\cos(\theta_n - \theta_{mn})H_0^{(1)}(k_0r_{mn}) - \frac{H_1^{(1)}(k_0r_{mn})}{k_0r_{mn}}e^{-i(\theta_n - \theta_{mn})}]e^{i\theta_{mn}}.\end{aligned}\quad (6.18)$$

Similarly,

$$\begin{aligned}\Phi_{-1}^r(\mathbf{r}_n) &= QH_{-1}^{(1)}(k_0r_{mn+})e^{i\theta_{mn+}} - QH_{-1}^{(1)}(k_0r_{mn-})e^{i\theta_{mn-}} \\ &\approx -2k_0\delta Q[\cos(\theta_n - \theta_{mn})H_0^{(1)}(k_0r_{mn}) - \frac{H_1^{(1)}(k_0r_{mn})}{k_0r_{mn}}e^{i(\theta_n - \theta_{mn})}]e^{-i\theta_{mn}}.\end{aligned}\quad (6.19)$$

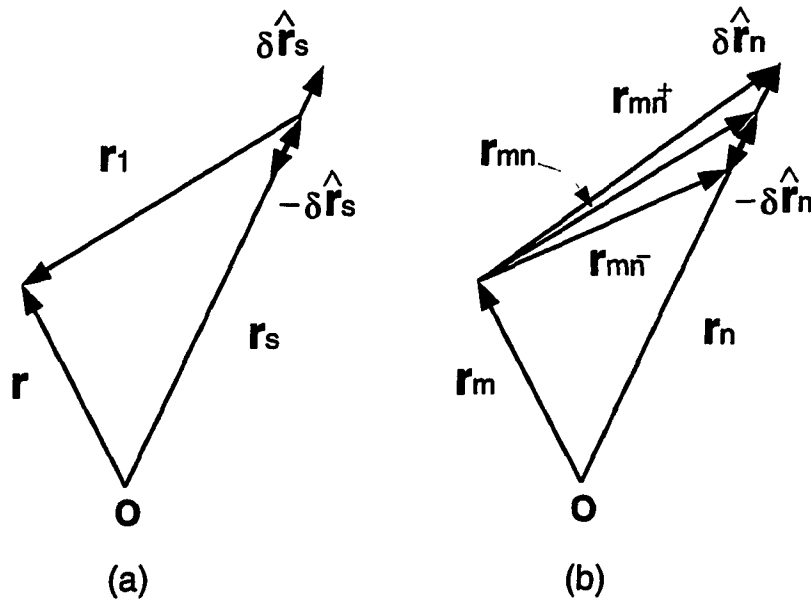


**Figure 6.1.** The diagram for (a) the dipole illumination and (b) the dipole reception.

### 6.3 Iterative Minimization Schemes

#### 6.3.1 Conjugate gradient minimization

This minimization scheme has been mentioned in Section 3.2. A cost function is defined as

$$S(\mathbf{O}) = \frac{1}{2} (\|\boldsymbol{\Phi}^{sca}(\mathbf{O}) - \boldsymbol{\Phi}_{meas}^{sca}\|^2 + \gamma \|\mathbf{O} - \mathbf{O}_b\|^2). \quad (6.20)$$

Refer to Section 3.2 for the list of the conjugate gradient minimization method.

In calculating the gradient and Hessian, the Fréchet operator can be found as

$$\bar{\mathbf{F}} = \frac{\partial \boldsymbol{\Phi}^{sca}}{\partial \mathbf{O}} = \frac{\partial}{\partial \mathbf{O}} [\bar{\boldsymbol{\Psi}}^t \cdot (\bar{\mathbf{I}} - \bar{\mathcal{D}}(\mathbf{O}) \cdot \bar{\mathbf{A}})^{-1} \cdot \bar{\mathcal{D}}(\mathbf{O}) \cdot \bar{\mathbf{B}} \cdot \mathbf{e}], \quad (6.21)$$

where (6.3) and (6.6) are used to substitute for  $\boldsymbol{\Phi}^{sca}$ . The above can be expanded into

$$\frac{\partial \boldsymbol{\Phi}^{sca}}{\partial \mathbf{O}} = \bar{\boldsymbol{\Psi}}^t \cdot \left[ \frac{\partial (\bar{\mathbf{I}} - \bar{\mathcal{D}}(\mathbf{O}) \cdot \bar{\mathbf{A}})^{-1}}{\partial \mathbf{O}} \cdot \bar{\mathcal{D}}(\mathbf{O}) \cdot \bar{\mathbf{B}} \cdot \mathbf{e} + (\bar{\mathbf{I}} - \bar{\mathcal{D}}(\mathbf{O}) \cdot \bar{\mathbf{A}})^{-1} \cdot \frac{\partial \bar{\mathcal{D}}(\mathbf{O})}{\partial \mathbf{O}} \cdot \bar{\mathbf{B}} \cdot \mathbf{e} \right]. \quad (6.22)$$

Let  $(\bar{\mathbf{I}} - \bar{\mathcal{D}}(\mathbf{O}) \cdot \bar{\mathbf{A}})^{-1} = \bar{\mathbf{K}}$ . We then have  $\bar{\mathbf{I}} = (\bar{\mathbf{I}} - \bar{\mathcal{D}}(\mathbf{O}) \cdot \bar{\mathbf{A}}) \cdot \bar{\mathbf{K}}$ . Thus,

$$\begin{aligned} 0 &= \frac{\partial}{\partial \mathbf{O}} (\bar{\mathbf{I}} - \bar{\mathcal{D}}(\mathbf{O}) \cdot \bar{\mathbf{A}}) \cdot \bar{\mathbf{K}} + (\bar{\mathbf{I}} - \bar{\mathcal{D}}(\mathbf{O}) \cdot \bar{\mathbf{A}}) \cdot \frac{\partial \bar{\mathbf{K}}}{\partial \mathbf{O}}, \\ \rightarrow \frac{\partial \bar{\mathbf{K}}}{\partial \mathbf{O}} &= (\bar{\mathbf{I}} - \bar{\mathcal{D}}(\mathbf{O}) \cdot \bar{\mathbf{A}})^{-1} \cdot \frac{\partial \bar{\mathcal{D}}(\mathbf{O})}{\partial \mathbf{O}} \cdot \bar{\mathbf{A}} \cdot (\bar{\mathbf{I}} - \bar{\mathcal{D}}(\mathbf{O}) \cdot \bar{\mathbf{A}})^{-1}. \end{aligned} \quad (6.23)$$

Substituting (6.23) into (6.22) and identifying that  $(\bar{\mathbf{I}} - \bar{\mathcal{D}}(\mathbf{O}) \cdot \bar{\mathbf{A}})^{-1} \cdot \bar{\mathcal{D}}(\mathbf{O}) \cdot \bar{\mathbf{B}} \cdot \mathbf{e} = \mathbf{a}$  by (6.6),  $\bar{\mathbf{F}}$  can be expressed as

$$\bar{\mathbf{F}} = \bar{\boldsymbol{\Psi}}^t \cdot (\bar{\mathbf{I}} - \bar{\mathcal{D}}(\mathbf{O}) \cdot \bar{\mathbf{A}})^{-1} \cdot \frac{\partial \bar{\mathcal{D}}(\mathbf{O})}{\partial \mathbf{O}} \cdot (\bar{\mathbf{A}} \cdot \mathbf{a} + \bar{\mathbf{B}} \cdot \mathbf{e}), \quad (6.24)$$

where the operation of  $\frac{\partial \bar{\mathcal{D}}(\mathbf{O})}{\partial \mathbf{O}}$  on a vector  $\mathbf{v} = [v_{-1,1} \ v_{0,1} \ v_{1,1} \ \dots \ v_{-1,N} \ v_{0,N} \ v_{1,N}]^t$  can be seen as

$$\begin{aligned} \frac{\partial \bar{\mathcal{D}}(\mathbf{O}) \cdot \mathbf{v}}{\partial \mathbf{O}} &= \frac{\partial}{\partial \mathbf{O}} [\gamma_1 v_{-1,1} \ \alpha_1 v_{0,1} \ \gamma_1 v_{1,1} \ \dots \ \gamma_N v_{-1,N} \ \alpha_N v_{0,N} \ \gamma_N v_{1,N}]^t, \\ &= \begin{pmatrix} v_{-1,1} & 0 & v_{-1,1} & 0 & \dots & 0 & 0 & 0 \\ 0 & v_{0,1} & 0 & 0 & \dots & 0 & 0 & 0 \\ v_{1,1} & 0 & v_{1,1} & 0 & \dots & 0 & 0 & 0 \\ \vdots & \vdots & \vdots & \vdots & \ddots & \vdots & \vdots & \vdots \\ 0 & 0 & 0 & 0 & \dots & v_{-1,N} & 0 & v_{-1,N} \\ 0 & 0 & 0 & 0 & \dots & 0 & v_{0,N} & 0 \\ 0 & 0 & 0 & 0 & \dots & v_{1,N} & 0 & v_{1,N} \end{pmatrix}, \end{aligned} \quad (6.25)$$

which is a block-diagonal matrix. Here  $\mathbf{O}$  is denoted as  $[\gamma_1 \ \alpha_1 \ \gamma_1 \ \dots \ \gamma_N \ \alpha_N \ \gamma_N]^t$ .

Note that at the  $n$ -th iteration,  $\bar{\mathbf{F}}$  is evaluated at  $\mathbf{O}_b$ , which is essentially  $\mathbf{O}_{n-1}$ , the transition coefficients from the previous iteration.

### 6.3.2 Distorted Born iterative method

The extremum of the functional (6.20) is the  $\mathbf{O}$  that equates the gradient to zero. Recalling from (3.2), the condition for the gradient to be zero is

$$\bar{\mathbf{F}}^\dagger \cdot (\boldsymbol{\Phi}^{sca} - \boldsymbol{\Phi}_{meas}^{sca}) + \gamma(\mathbf{O} - \mathbf{O}_b) = 0. \quad (6.26)$$

The above equation is a nonlinear equation, which can be acknowledged by writing  $\boldsymbol{\Phi}^{sca}$  as the function of  $\mathbf{O}$ . However, for the  $n$ -th iteration, (6.26) can be linearized by way of approximating  $\boldsymbol{\Phi}_n^{sca}$  by

$$\boldsymbol{\Phi}_n^{sca} \simeq \boldsymbol{\Phi}_{n-1}^{sca} + \bar{\mathbf{F}}_{n-1} \cdot (\mathbf{O}_n - \mathbf{O}_{n-1}), \quad (6.27)$$

where  $\bar{\mathbf{F}}_{n-1}$  denotes  $\bar{\mathbf{F}}|_{\mathbf{O}=\mathbf{O}_{n-1}}$ . Hence, substituting (6.27) into (6.26) and solving for  $\mathbf{O}_n$ , we obtain

$$\mathbf{O}_n = \mathbf{O}_{n-1} + (\bar{\mathbf{F}}_{n-1}^\dagger \cdot \bar{\mathbf{F}}_{n-1} + \gamma \bar{\mathbf{I}})^{-1} \cdot \bar{\mathbf{F}}_{n-1}^\dagger \cdot (\boldsymbol{\Phi}_{meas}^{sca} - \boldsymbol{\Phi}_{n-1}^{sca}). \quad (6.28)$$

The above is the updating scheme of  $\mathbf{O}_n$  for the distorted Born iterative method (DBIM). The explicit form for  $\bar{\mathbf{F}}_n$  was described in Section 6.3.1.

## 6.4 Algorithm Implementation

In implementing either algorithm in Section 6.3, the scattered field  $\Phi_n^{sca}$  is always calculated according to (6.3) and (6.6). The operation of the inverse matrix on the vector in (6.6) is implemented by CGFFT. Because CGFFT is an iterative method, it has to be invoked again whenever the operated vector changes. In a multiview imaging setup, there are  $N_T$  views, so that the cost of implementing (6.6) is  $O(N_T N_{i1} N \log N)$ , where  $N_{i1}$  is the iteration number for CGFFT to converge for each incident field. The matrix-vector multiply in (6.3) can be carried out efficiently by the nested equivalence principle algorithm (NEPAL) as suggested in Chapter 4 and can be achieved in  $O(N_T N \log N)$  operations followed by a propagation from the boundary points to the receivers, which requires a small  $O(N_T N^{0.5} N_R)$  cost, where  $N_R$  is the number of receivers. At the current stage, (6.3) is still calculated directly since (6.6) is the most dominant part because  $N$  is not very large.

In addition to  $\Phi_n^{sca}$ , in each iteration,  $\bar{\mathbf{F}}_n \cdot \mathbf{v}$  and  $\bar{\mathbf{F}}_n^\dagger \cdot \mathbf{v}$  have to be calculated and are computationally intensive. In (6.24),  $\bar{\mathbf{A}} \cdot \mathbf{a}$  can be calculated by FFT in  $O(N \log N)$  operations and the following operation by  $\partial \bar{\mathcal{D}}(\mathbf{O}) \cdot \mathbf{v} / \partial \mathbf{O}$  is achieved with the aid of (6.25). Next, the multiplication of the inverse matrix,  $(\bar{\mathbf{I}} - \bar{\mathcal{D}}(\mathbf{O}) \cdot \bar{\mathbf{A}})^{-1}$  with the resultant vector is again implemented by CGFFT, which has an  $O(N_T N_{i2} N \log N)$  cost, where  $N_{i2}$  is the iteration number for CGFFT to converge per view. Finally,  $\bar{\Psi}^t \cdot \mathbf{v}$  is calculated by NEPAL in  $O(N_T N \log N)$  operations.

The second way to implement (6.24) is to calculate the explicit matrix  $\bar{\Psi}^t \cdot (\bar{\mathbf{I}} - \bar{\mathcal{D}}(\mathbf{O}) \cdot \bar{\mathbf{A}})^{-1}$  by CGFFT because it can be rewritten as  $[(\bar{\mathbf{I}} - \bar{\mathcal{D}}(\mathbf{O}) \cdot \bar{\mathbf{A}})^{-t} \cdot \bar{\Psi}]^t$ , where the bracketed term can be interpreted as that for each “incident” field back-propagating from the receiver to the object, the “scattering” amplitudes are found in all the cells. This process takes  $N_R N_{i3} N \log N$  operations. In this way, the calculated matrix is stored and the ensuing matrix-vector multiply is implemented directly in  $O(N_R N_T N)$  operations.

Generally, better reconstructions can be obtained with  $N_R N_T \sim N$  or  $N_R \sim N^{0.5}$  and  $N_T \sim N^{0.5}$ . Therefore, the complexity of the first method is  $O(N_{i2} N^{1.5} \log N)$ , while that of the second one is  $O(N^2)$ . If  $N_{i2} \sim N^\beta$ , where  $\beta < 0.5$ , the former is more efficient than the latter. To date, the second method is adopted in our algorithms because from the observation of simulations, the forward solving part still dominates the total computational cost. However, when  $N$  is very large and  $N_T$  and  $N_R$  are appropriately chosen, the first method should prevail over the second one.

Similarly, the implementation of the conjugate transpose of  $\bar{\mathbf{F}}_n$  on a vector or

$$\bar{\mathbf{F}}_n^\dagger \cdot \mathbf{v} = \left[ \frac{\partial \bar{\mathcal{D}}(\mathbf{O})}{\partial \mathbf{O}} \cdot (\bar{\mathbf{A}} \cdot \mathbf{a} + \bar{\mathbf{B}} \cdot \mathbf{e}) \right]^\dagger \cdot (\bar{\mathbf{I}} - \bar{\mathcal{D}}(\mathbf{O}) \cdot \bar{\mathbf{A}})^{-\dagger} \cdot \bar{\Psi}^* \cdot \mathbf{v}, \quad (6.29)$$

can be done by utilizing NEPAL (see Chapter 4) for  $\bar{\Psi}^*$  for calculating the “incident” field at each cell due to the “sources” at receivers and followed by  $N_T$  times of CGFFT solvers to account for  $(\bar{\mathbf{I}} - \bar{\mathcal{D}}(\mathbf{O}) \cdot \bar{\mathbf{A}})^{-\dagger}$ . The complexity of these operations is  $O(N_{i4} N^{1.5} \log N)$ , where  $N_{i4}$  is the number of iterations for CGFFT to converge for every view. On the other hand, directly implementing the operator,  $\bar{\Psi}^\dagger \cdot (\bar{\mathbf{I}} - \bar{\mathcal{D}}(\mathbf{O}) \cdot \bar{\mathbf{A}})^{-\dagger}$  results in an  $O(N^2)$  algorithm.

As a result, if there are  $N_O$  iterations for the conjugate gradient minimization method to arrive at the satisfactory reconstruction, the cost is  $O(N_O [N_{i1} + N_{i2} + 2N_{i4}] N^{1.5} \log N)$  or  $O(N_O N^2)$  depending on how one implements  $\bar{\Psi}^\dagger \cdot (\bar{\mathbf{I}} - \bar{\mathcal{D}}(\mathbf{O}) \cdot \bar{\mathbf{A}})^{-\dagger}$  and its transpose.

On the other hand, DBIM involves one more level of iteration, namely the inverse operator  $(\bar{\mathbf{F}}_{n-1}^\dagger \cdot \bar{\mathbf{F}}_{n-1} + \gamma \bar{\mathbf{I}})^{-1}$  in (6.28). This inversion can be done by the conjugate gradient method (CGM). Provided that  $N_m$  are needed for convergence, the cost becomes  $O(N_{O'} N_m (N_{i1} + N_{i2} + 2N_{i4}) N^{1.5} \log N)$  or  $O(N_{O'} N_m N^2)$ , where  $N_{O'}$  is the iteration number for outermost layer iteration. It can be expected that  $N_O > N_{O'}$  because the former minimization scheme advances only one step along the conjugate direction toward the minimum for each iteration, while the latter reaches

the bottom of the multi-dimensional parabolic curve according to the conjugate vector for each iteration. This can be illustrated by Figure 6.2 for a simple one-variable case. Besides, DBIM is more sensitive to the choice of the regularization parameter since the inverse operator in (6.28) is ill-posed when  $\gamma$  is small.

To expedite the algorithm, the calculated scattering amplitudes in the current iteration have to be stored in the memory or the disk space until the next iteration launches. The required space is proportional to  $N^{1.5}$ , which easily swamps the computer memory when  $N$  is large. Therefore, the disk space usage efficiency is the choice to sacrifice some computational efficiency.

## 6.5 Results

We begin with validation of the forward solver code. Figure 6.3 shows the comparison between the exact solution and the numerical result for a two-layered circle with  $\rho_1 = 1.1$ ,  $\kappa_1 = 1.05 + i0.2$  and  $\rho_2 = 1.2$ ,  $\kappa_2 = 1.1 + i0.3$ . The inner radius is  $0.5\lambda_0$  and the outer radius  $1\lambda_0$ , where  $\lambda_0$  is the background wavelength. In the following simulations, the object is assumed to be immersed in the water with  $\rho_0 = 1$  and  $\kappa_0 = 1$ . A good agreement is observed in the scattered fields. The second case is similar to the first one except that  $\rho_1 = 1.5$  and  $\kappa_1 = 0.80 + i0.3$ ;  $\rho_2 = 2.0$  and  $\kappa_2 = 0.6 + i0.4$ . The numerical result agrees well with the exact solution as shown in Figure 6.4.

### 6.5.1 Synthetic data

We first reconstruct an inhomogeneous object with density variation only. The compressibility is the same constant as that of the background medium. The reconstructed area is  $2.26\lambda_0 \times 2.26\lambda_0$  and is divided into a  $32 \times 32$  mesh. Only 16 transmitters and 32 receivers are used. Both the true profile and the reconstructed one are shown in Figure 6.5, and a good reconstruction is observed. DBIM is employed in this case, and it takes 14 iterations for the relative residual error (RRE) to be reduced to  $1.6 \times 10^{-3}$ . The CPU time is about 2.4 hours on a 5 MFLOPS machine.

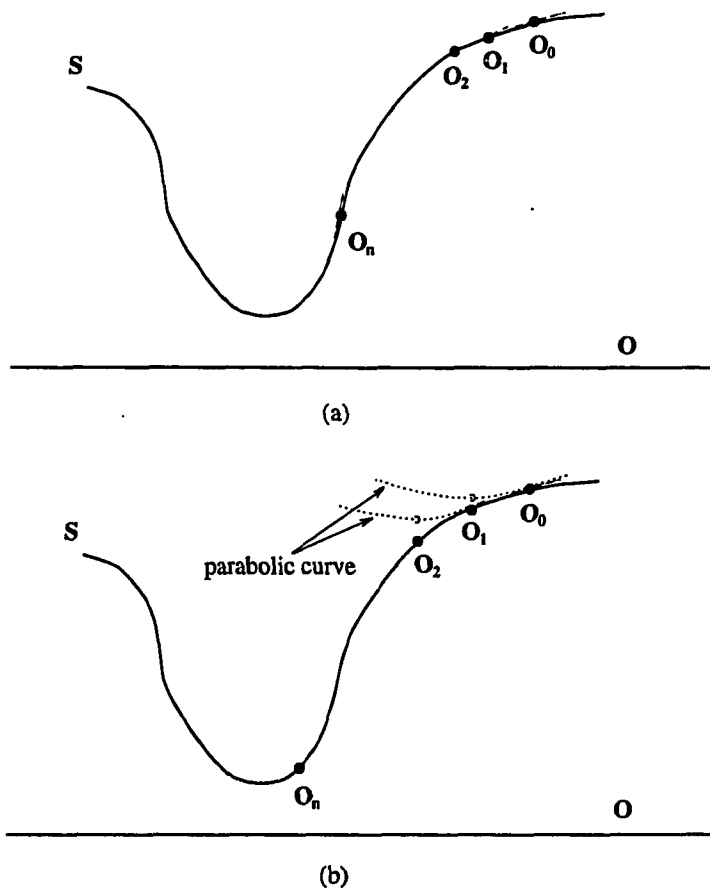


**Figure 6.2.** (a) The conjugate gradient minimization scheme; (b) the distorted Born iterative method.

As mentioned in Chapter 3, the inverse problem becomes more nonlinear when the object becomes larger. It is difficult to obtain a good reconstruction quantitatively by only a single frequency. As suggested by better reconstruction using the pulse in time domain to probe the object, the multiple-frequency method can alleviate the nonlinear problem when the object size is large. Simultaneously processing the multiple-frequency data by an inverse scattering algorithm is one way to achieve this end; another way is to use the frequency-hopping scheme proposed

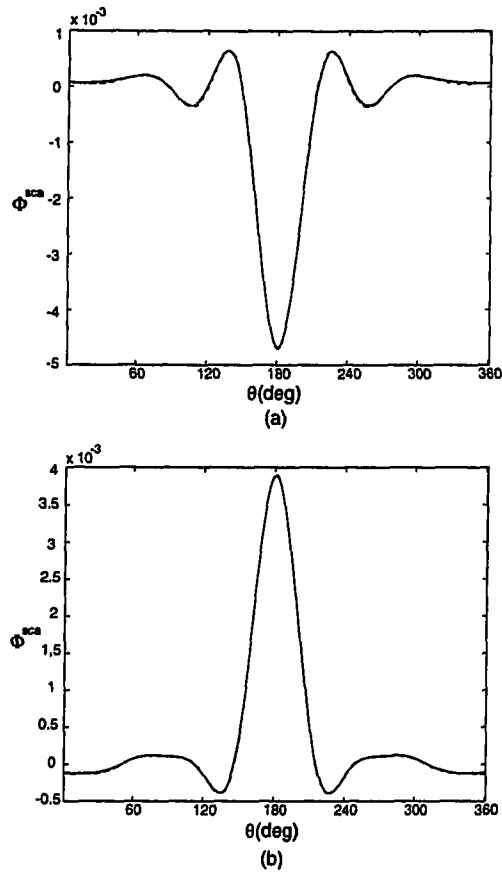


**Figure 6.3.** Comparison of the exact solution (solid line) and the numerical result (dashed line) for a two-layered circle with  $\rho_1 = 1.1$ ,  $\kappa_1 = 1.05 + i0.2$  and  $\rho_2 = 1.2$ ,  $\kappa_2 = 1.1 + i0.3$ .  $r_1 = 1.0\lambda_0$  and  $r_2 = 0.5\lambda_0$ : (a) real component; (b) imaginary component.

in Chapter 3. The idea is that the reconstruction for the lower frequency is used as the initial guess for the next higher frequency; the process is repeated until the desired highest frequency is reached. Only several discrete frequencies are required to complete the hopping scheme. Demonstrated in Figure 6.6 are the profiles of true and reconstructed objects for two frequencies. Figure 6.7 shows the corre-

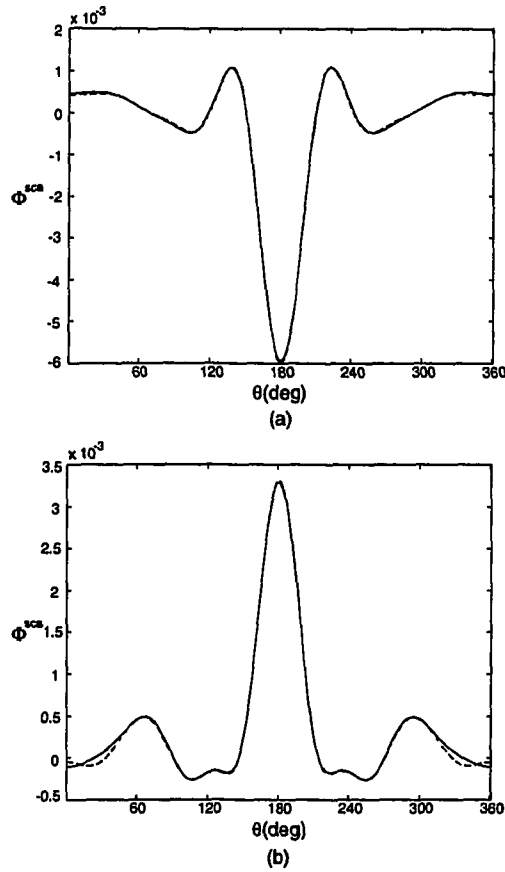


**Figure 6.4.** Comparison of the exact solution (solid line) and the numerical result (dashed line) for a two-layered circle with  $\rho_1 = 1.5$ ,  $\kappa_1 = 0.80 + i0.3$  and  $\rho_2 = 2.0$ ,  $\kappa_2 = 0.6 + i0.4$ .  $r_1 = 1.0\lambda_0$  and  $r_2 = 0.5\lambda_0$ : (a) real component; (b) imaginary component.

sponding images. The area size is  $4.52\lambda_0 \times 4.52\lambda_0$ , and a  $64 \times 64$  grid is used under a configuration of 32 transmitters and 64 receivers. Only 150 kHz and 300 kHz are used as the probing frequencies. The fidelity of the reconstructed density, as well as the high resolution, can be observed in Figures 6.6 and 6.7. The conjugate gradient minimization method is run on a Cray 90 machine, and the total CPU time is about 23 minutes to achieve  $RRE = 2.9 \times 10^{-3}$  accuracy.

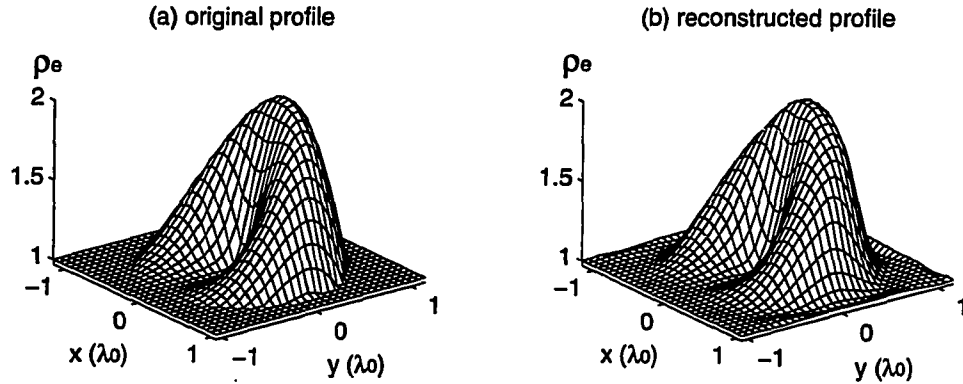


**Figure 6.5.** The true and reconstructed density profiles (no compressibility variation). The reconstructed area is  $2.26\lambda_0 \times 2.26\lambda_0$  and is divided into a  $32 \times 32$  mesh. There are 16 transmitters and 32 receivers.

In addition to the density variation, real bodies often contain compressibility variation. In Figure 6.8, an object inhomogeneous in density and modulus (or  $1/\text{compressibility}$ ) is reconstructed. A  $16 \times 16$  grid is used for the reconstruction area of  $1\lambda_0 \times 1\lambda_0$ . Similarly, a full-angle imaging system is utilized and consists of 16 transmitters and 15 receivers for each insonification. From Figure 6.8(b), the single-frequency method fails to reconstruct both parameters properly. This is because the scattered fields either by the induced dipoles (accounted for by density) or monopoles (accounted for by modulus) cannot be differentiated in the nonlinear problem. One remedy is to use the multiple-frequency concept: when the object is not large compared to the wavelength, the inverse scattering problem is less nonlinear. This conjecture is justified by the frequency-hopping reconstruction shown in Figure 6.8(c). Probing frequencies are 150 kHz, 225 kHz and 300 kHz. The CPU time on an HP 715 machine is about 22 minutes, and the RRE is reduced to  $4.26 \times 10^{-3}$ . The density profile shows more high-frequency structures than does

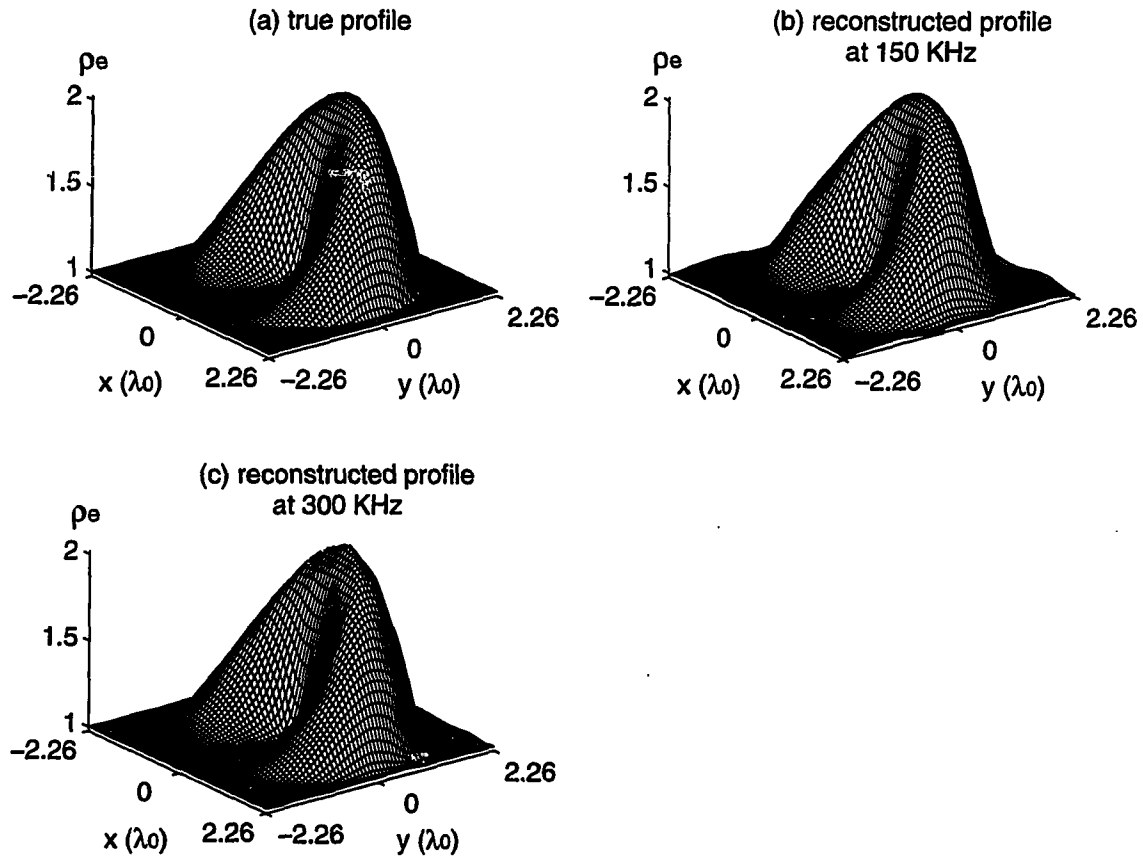


**Figure 6.6.** The true and reconstructed density profiles (no compressibility variation) by the frequency-hopping scheme. The reconstructed area is  $4.52\lambda_0 \times 4.52\lambda_0$  (background wavelength at 300 kHz) and is divided into a  $64 \times 64$  mesh. There are 32 transmitters and 64 receivers.

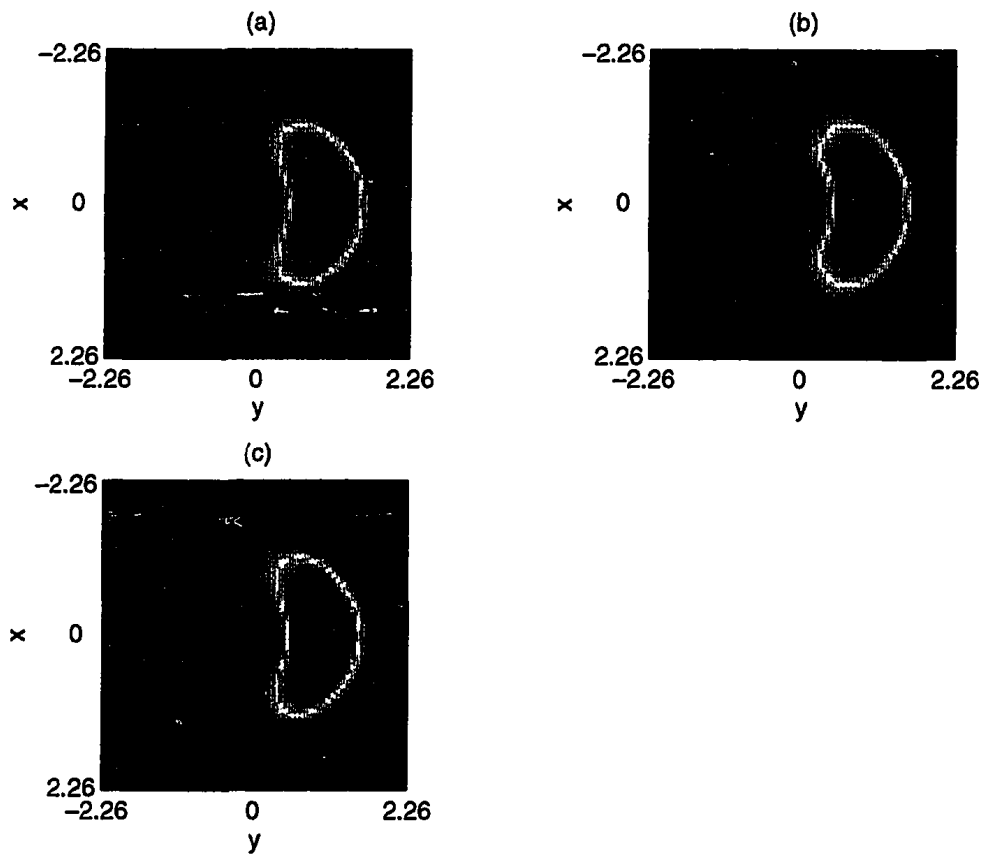


**Figure 6.7.** The true and reconstructed density images by the frequency-hopping scheme: (a) true image (b) reconstructed image at 150 kHz (c) reconstructed image at 300 kHz. The reconstructed area is  $4.52\lambda_0 \times 4.52\lambda_0$  (background wavelength at 300 kHz) and is divided into a  $64 \times 64$  mesh. There are 32 transmitters and 64 receivers.

the modulus profile, which is like a smeared version of the true profile. In all, the reconstruction by the frequency-hopping method correctly predicts how the true profile changes.

The next example is a circular cylinder profile in density and modulus shown in Figure 6.9. The problem size, imaging configuration and frequencies are the same as the first example in Figure 6.8. The frequency-hopping reconstruction is much better than the single-frequency one. The density reconstruction in Figure 6.9(c) can delineate the circular boundary quite well in spite of the much smoother modulus reconstruction.

The third case consists of enlarging the problem size to  $2\lambda_0 \times 2\lambda_0$  with a  $32 \times 32$  mesh and changing the circular cylinder to a circular well in the modulus profile. Thirty-two transmitters sequentially emit the probing wave with the other elements as the receivers. Hence, there are  $32 \times 31$  sets of measurement data. The frequency-hopping method utilizes 300 kHz, 600 kHz, 1.2 MHz and 2.4 MHz. Figure 6.10 shows the reconstruction results. Apparently, Figure 6.10(c) provides better reconstructions quantitatively than Figure 6.10(b). The RRE is less than  $10^{-3}$ , and it takes 4 hours CPU time on a HP 715 workstation.

As a final example in this subsection, we consider a case similar to the previous one, except that the density contrast is increased to 1.2 and the modulus contrast is reduced to 0.833. Results are shown in Figure 6.11. It is observed that the single-frequency scheme still can give a good reconstruction qualitatively even though the reconstructed values are not correct. This observation is helpful when the multiple-frequency data is not available.

### **6.5.2 Experimental data**

Some experimental data are provided by ThermoTrex Corporation (TTC) in San Diego, California. Their experimental system consists of a cylindrical transducer array. Each element in turn acts as a transmitter, while the remaining transducers record the signal emanating from the object. One-thousand twenty-four separate

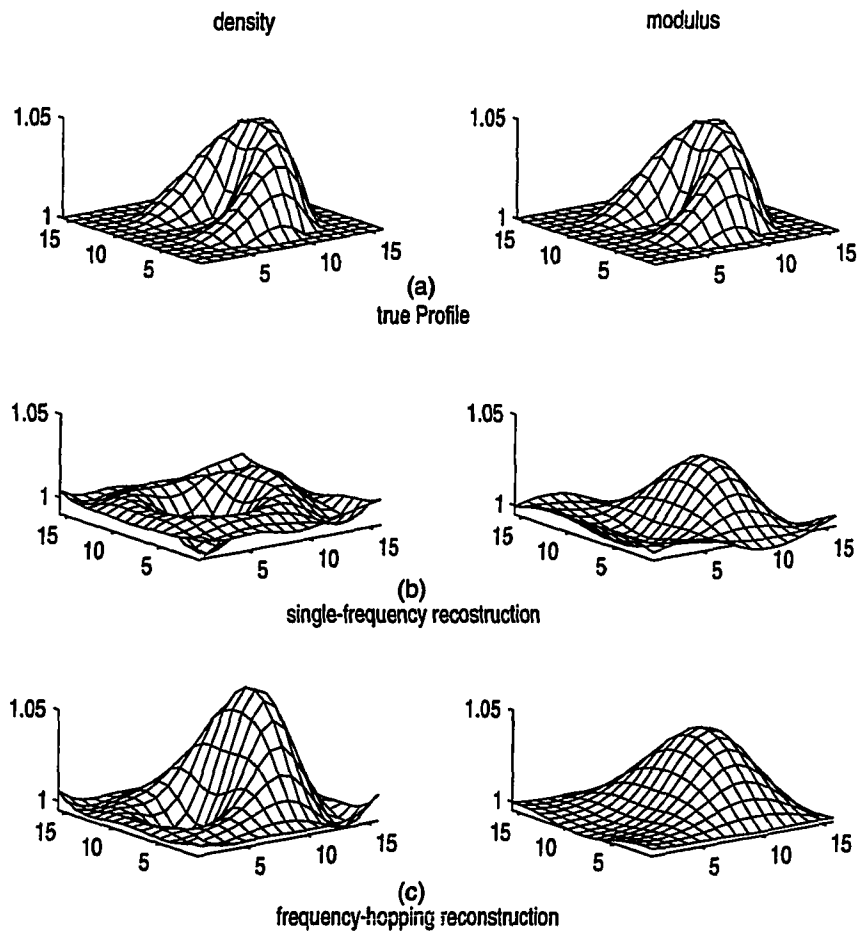


**Figure 6.8.** The true and reconstructed profiles in the density and modulus. The reconstructed area is  $1\lambda_0 \times 1\lambda_0$  and divided into a  $16 \times 16$  mesh. There are  $16 \times 15$  sets of measurement data. 150 kHz, 225 kHz and 300 kHz are used in the frequency-hopping scheme.

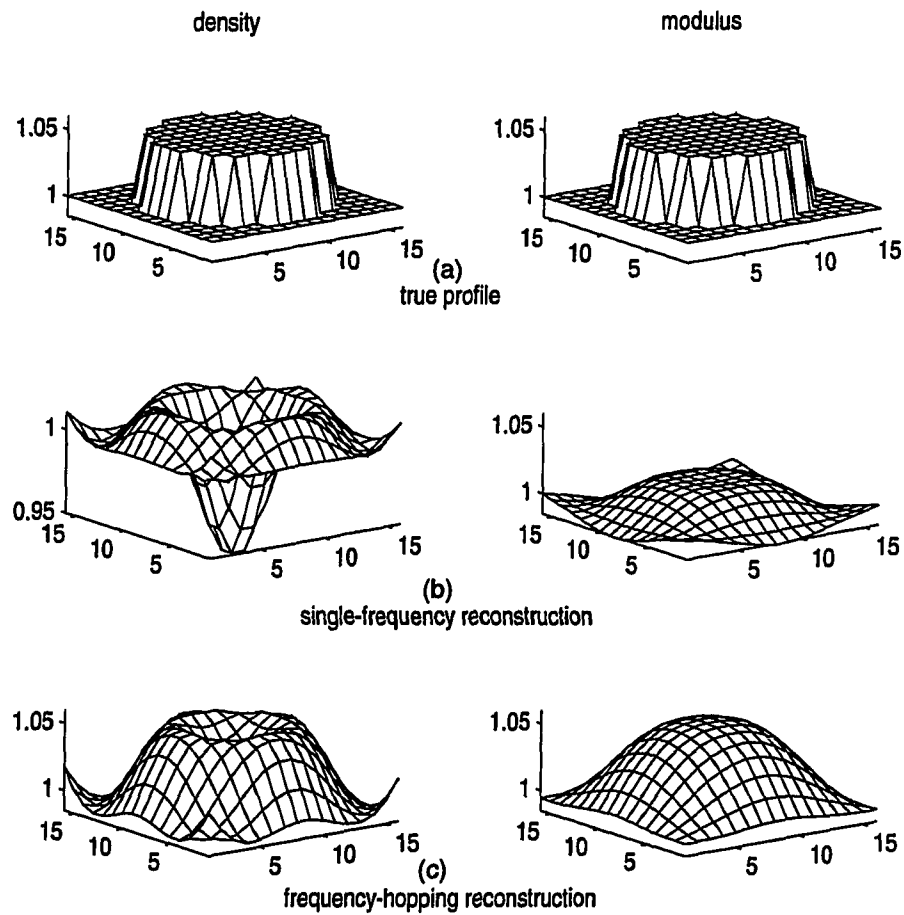


**Figure 6.9.** The true and reconstructed profiles in the density and modulus. The reconstructed area is  $1\lambda_0 \times 1\lambda_0$  and divided into a  $16 \times 16$  mesh. There are  $16 \times 15$  sets of measurement data. 150 kHz, 225 kHz and 300 kHz are used in the frequency-hopping scheme.

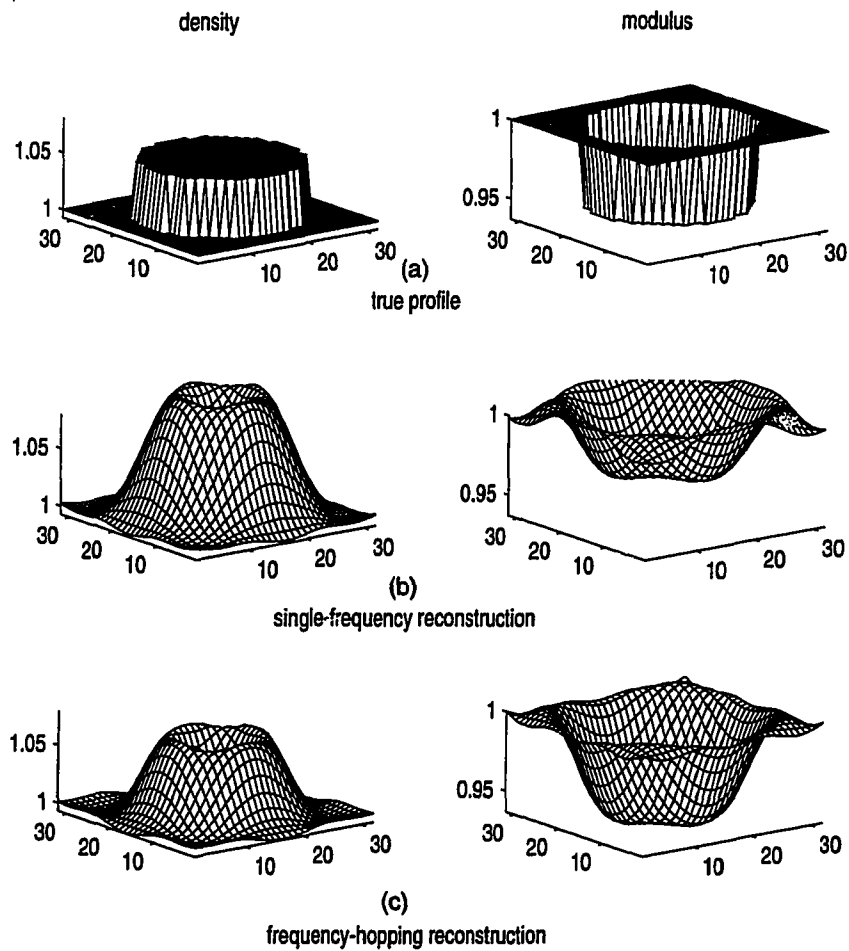


**Figure 6.10.** The true and reconstructed profiles in the density and modulus. The reconstructed area is  $2\lambda_0 \times 2\lambda_0$  and divided into a  $32 \times 32$  mesh. There are  $32 \times 31$  sets of measurement data. 300 kHz, 600 kHz, 1.2 MHz and 2.4 MHz are used in the frequency-hopping scheme.

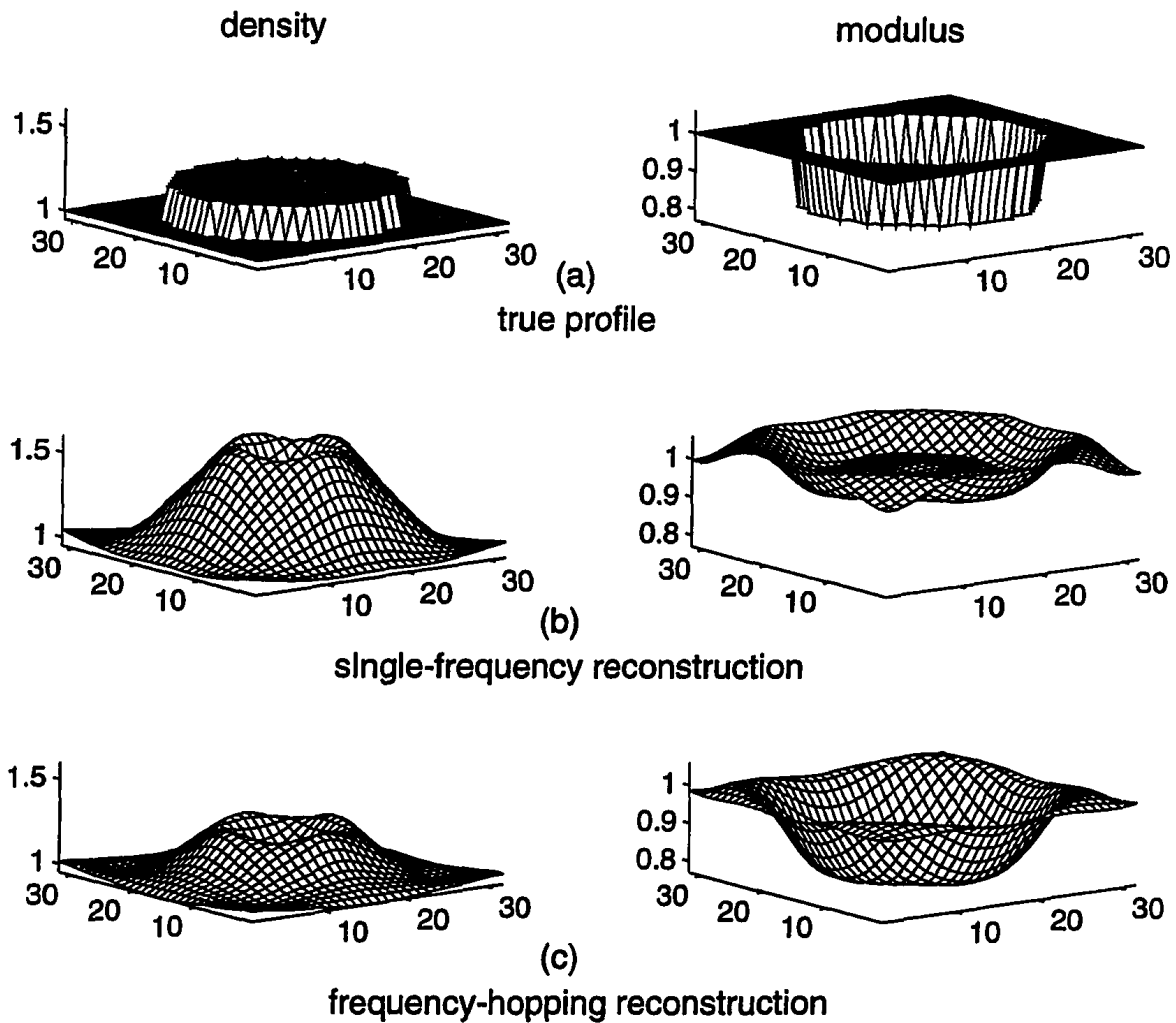


**Figure 6.11.** The true and reconstructed profiles in the density and modulus. The reconstructed area is  $2\lambda_0 \times 2\lambda_0$  and divided into a  $32 \times 32$  mesh. There are  $32 \times 31$  sets of measurement data. 300 kHz, 600 kHz, 1.2 MHz and 2.4 MHz are used in the frequency-hopping scheme.

transmissions are made around the object. The 20cm cylindrical transducer array of 1024 elements is placed in the water bath.

The first object is a dual-balloon placed in the water. There are  $512 \times 512$  sets of measurement data available. Due to the near field effects, the data within 50 transducers of the transmitter are not used. Because of computer resource limitations, only  $128 \times 102$  transmitter/receiver paired data are used to reconstruct a  $14\lambda_0 \times 14\lambda_0$  area, which is divided into  $127 \times 127$  cell. The operating frequency is 312.5 kHz and the background wavelength is 4.8 mm. Shown in Figures 6.12 and 6.13 are the reconstructed images for iteration 1 and iteration 8. Both images show the shape and location of the dual-balloon, but the image contrast in Figure 6.13 is more pronounced than that in Figure 6.12. The dark point at the center is the tank origin. The  $x$ -axis cross sections through the center for the real part of the modulus are shown in Figure 6.14. The data processing is done on a Sun SPARCclassic machine (5 MFLOPS). It takes about 12 hours CPU time for each iteration. After the 9th iteration, the RRE still remains at around 0.95. This is probably because the ratio of signal to noise is too small in the measurement data, which makes it difficult to extract the proper information from the data. The diffraction tomography method (DT) is used by TTC to reconstruct the dual-balloon images. Because they consider Equation (6.2), images for the sound speed and attenuation are reconstructed and shown in Figure 6.15.

The second object is a boiled egg. The operating frequency is 468.75 kHz and  $\lambda_0 = 3.2$  mm. A  $181 \times 181$  grid is placed onto a  $18.14\lambda_0 \times 18.14\lambda_0$  area, in which 256 transmitters are illuminating and 205 receivers are collecting the signal. The images of the density and modulus are shown in Figures 6.16, 6.17 and 6.18, respectively. The egg is suspended in the tank through a hole indicated by its central point. The egg's exterior boundary and the yolk within can be identified from the images. An artificial wire scar of  $60 \mu\text{m}$  as well as some tiny knicks can also be found. The shapes of the egg and the yolk are somehow distorted in the images of the modulus imaginary part. Plots of  $x$ -axis cross sections are shown in Figure 6.19. We resort to the Power Challenge machine (300 MFLOPS per processor) in NCSA to process

the data. It takes about 8 hours CPU time per iteration. Restricted by available CPU time allocation, only two iterations are accomplished thus far and the RRE is 0.897. Images for the sound speed and attenuation reconstructed by DT are shown in Figure 6.20. In TTC, the egg images were computed at 343.75 kHz.

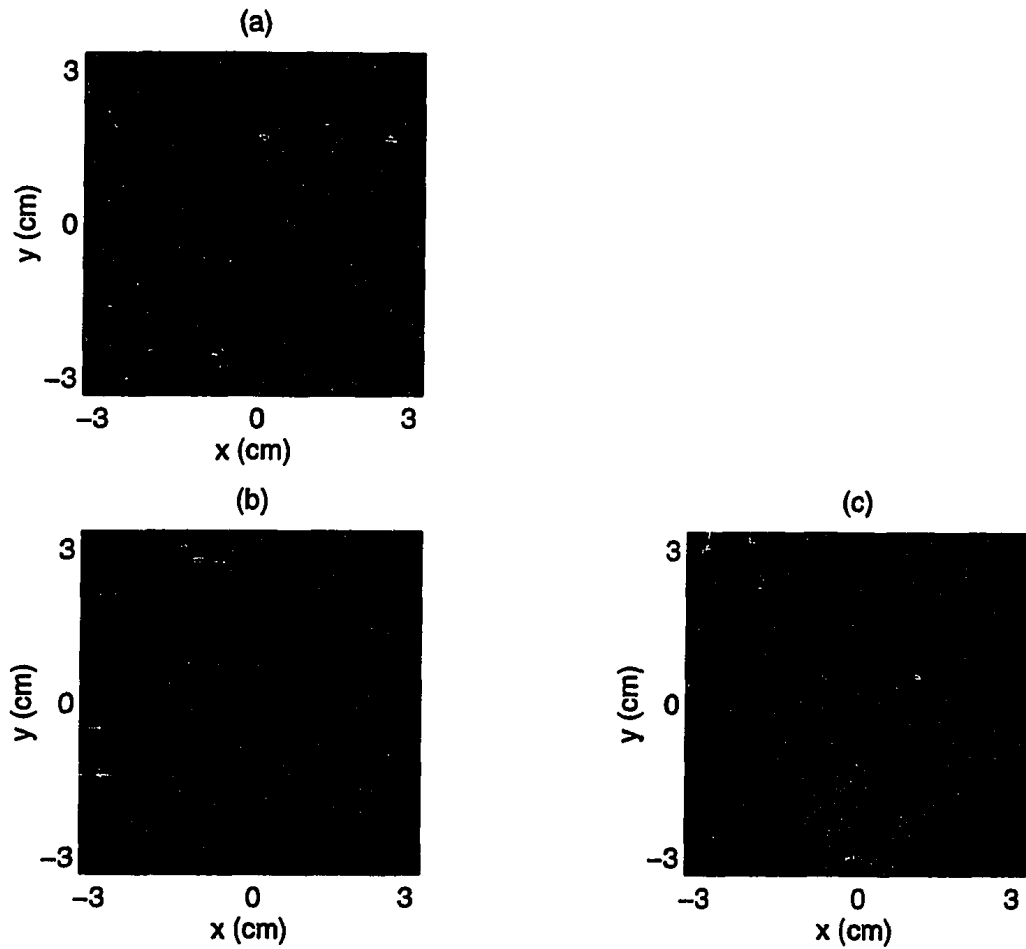


**Figure 6.12.** The dual-balloon images for iteration 1: (a) density (b) real part of the modulus (c) imaginary part of the modulus. The frequency is 312.5 kHz and  $\lambda_0 = 4.8$  mm. The reconstruction area is  $14\lambda_0 \times 14\lambda_0$  and divided into  $127 \times 127$  cells.  $128 \times 102$  transmitter/receiver paired data are used.

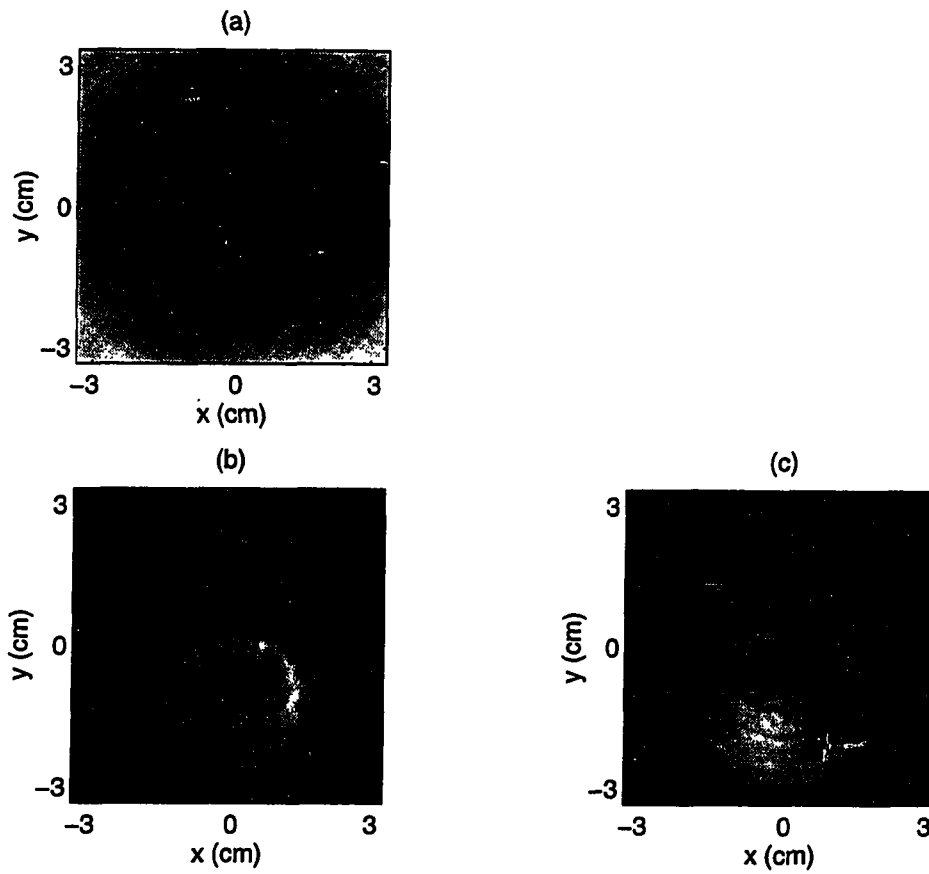
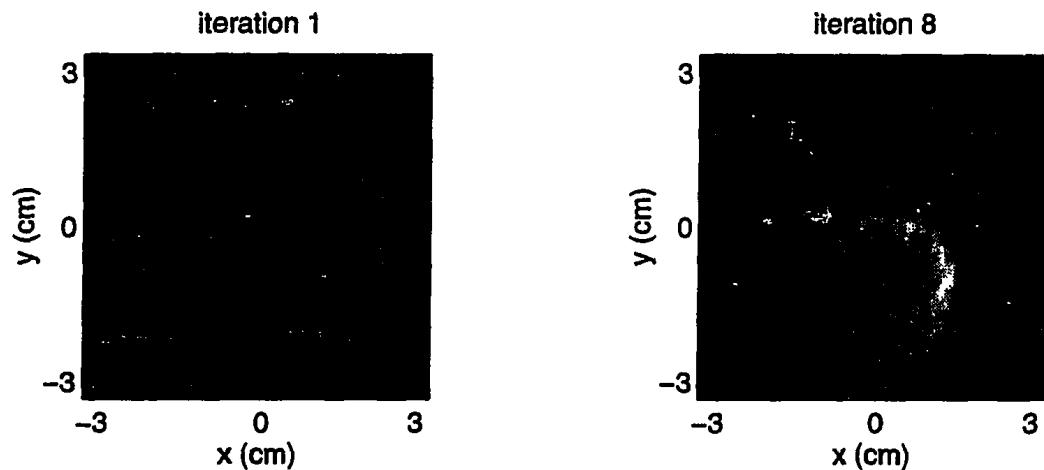
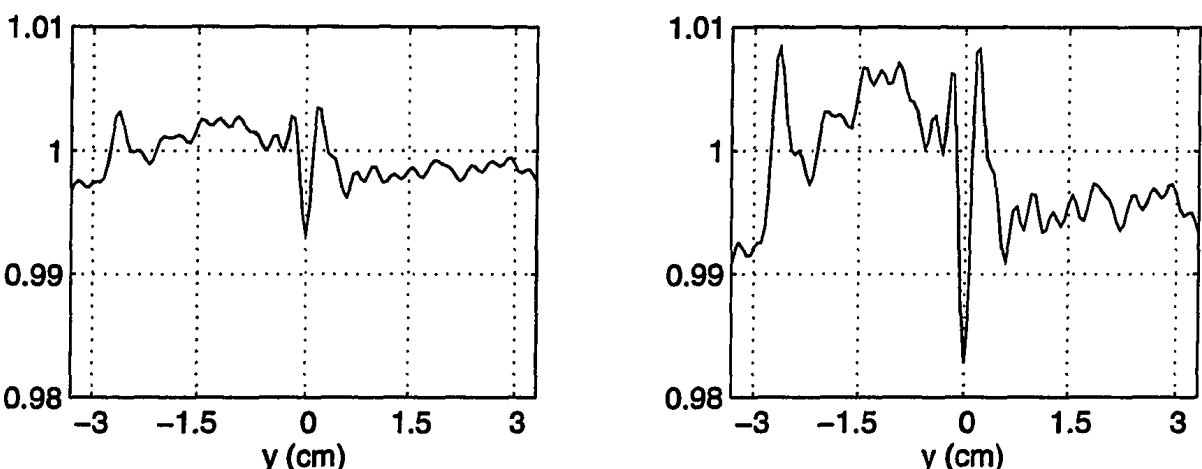


**Figure 6.13.** The dual-balloon images for iteration 8: (a) density (b) real part of the modulus (c) imaginary part of the modulus. The frequency is 312.5 kHz and  $\lambda_0 = 4.8$  mm. The reconstruction area is  $14\lambda_0 \times 14\lambda_0$  and divided into  $127 \times 127$  cells.  $128 \times 102$  transmitter/receiver paired data are used.



(a) images of the real part of the modulus



(b) *y*-axis cross sections of the modulus

**Figure 6.14.** Comparison of the dual-balloon reconstructions for iteration 1 and iteration 8. The frequency is 312.5 kHz and  $\lambda_0 = 4.8$  mm. The reconstruction area is  $14\lambda_0 \times 14\lambda_0$  and divided into  $127 \times 127$  cells.  $128 \times 102$  transmitter/receiver paired data are used.

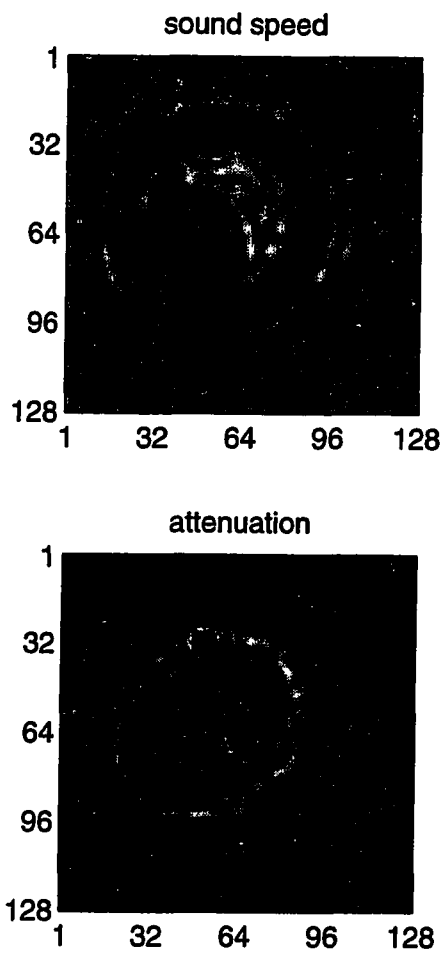


**Figure 6.15.** The dual-balloon images for the sound speed and attenuation. Images are reconstructed at 312.5 kHz by the diffraction tomography method and provided by ThermoTrex Corp.

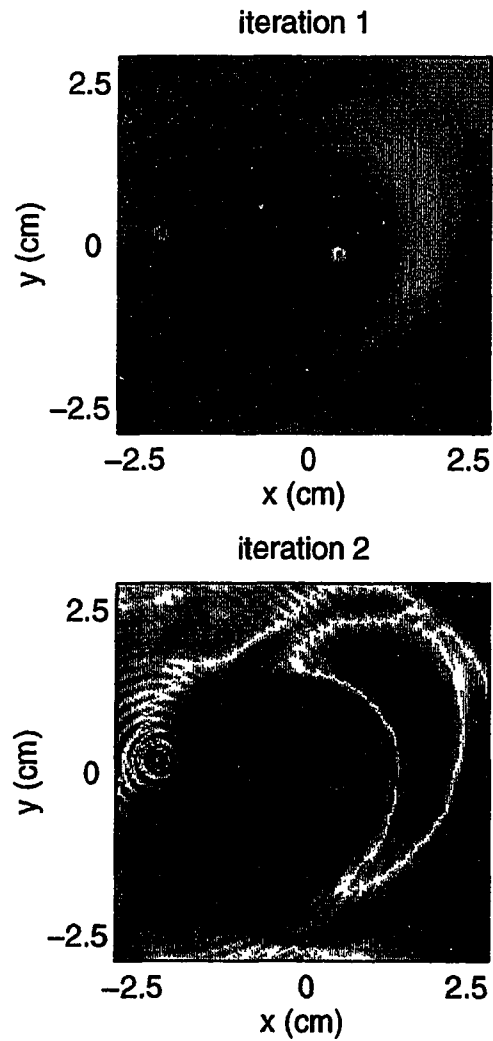


**Figure 6.16.** Density images of a boiled egg for iteration 1 and 2. The frequency is 468.75 kHz and  $\lambda_0 = 3.2$  mm. The reconstruction area is  $18.14\lambda_0 \times 18.14\lambda_0$  and divided into  $181 \times 181$  cells.  $256 \times 205$  transmitter/receiver paired data are used.

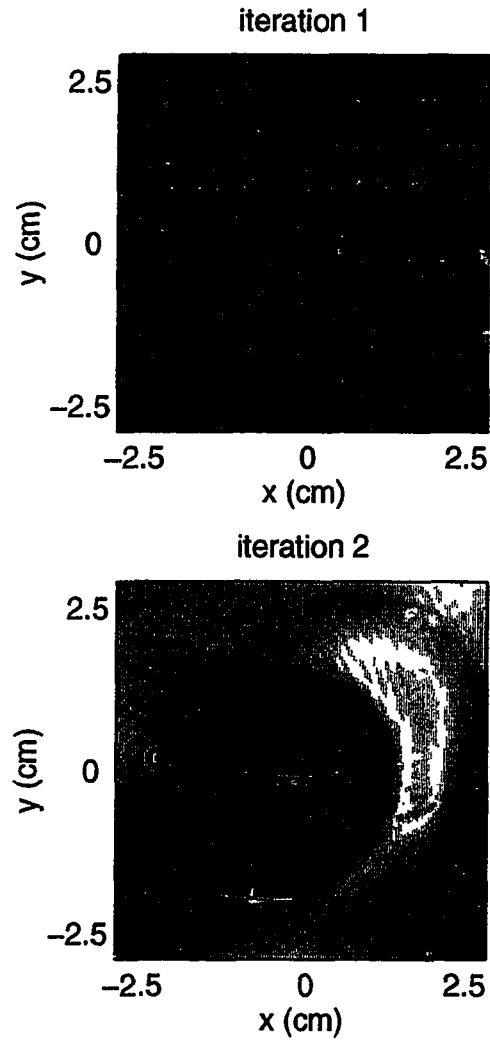


**Figure 6.17.** The real part of the modulus images of a boiled egg for iteration 1 and 2. The frequency is 468.75 kHz and  $\lambda_0 = 3.2$  mm. The reconstruction area is  $18.14\lambda_0 \times 18.14\lambda_0$  and divided into  $181 \times 181$  cells.  $256 \times 205$  transmitter/receiver paired data are used.

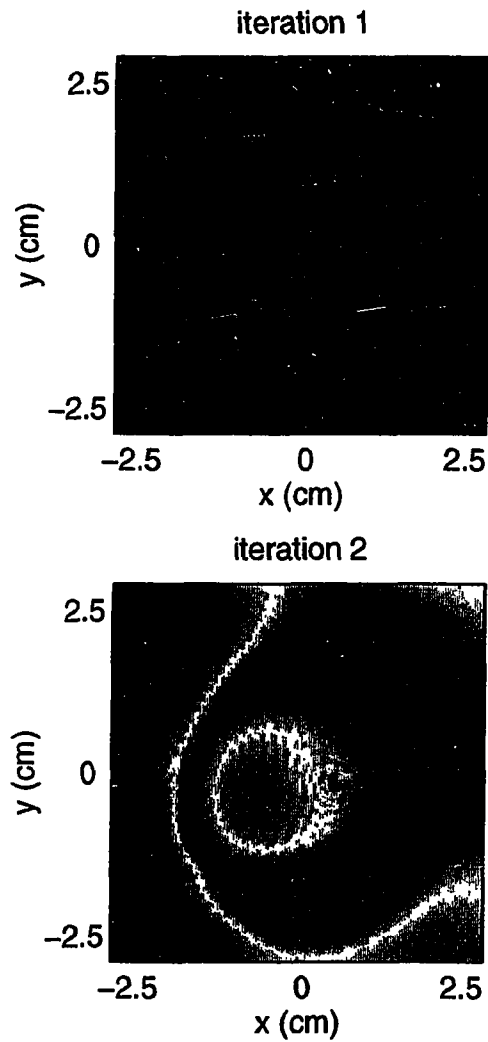


**Figure 6.18.** The imaginary part of the modulus images of a boiled egg for iteration 1 and 2. The frequency is 468.75 kHz and  $\lambda_0 = 3.2$  mm. The reconstruction area is  $18.14\lambda_0 \times 18.14\lambda_0$  and divided into  $181 \times 181$  cells.  $256 \times 205$  transmitter/receiver paired data are used.

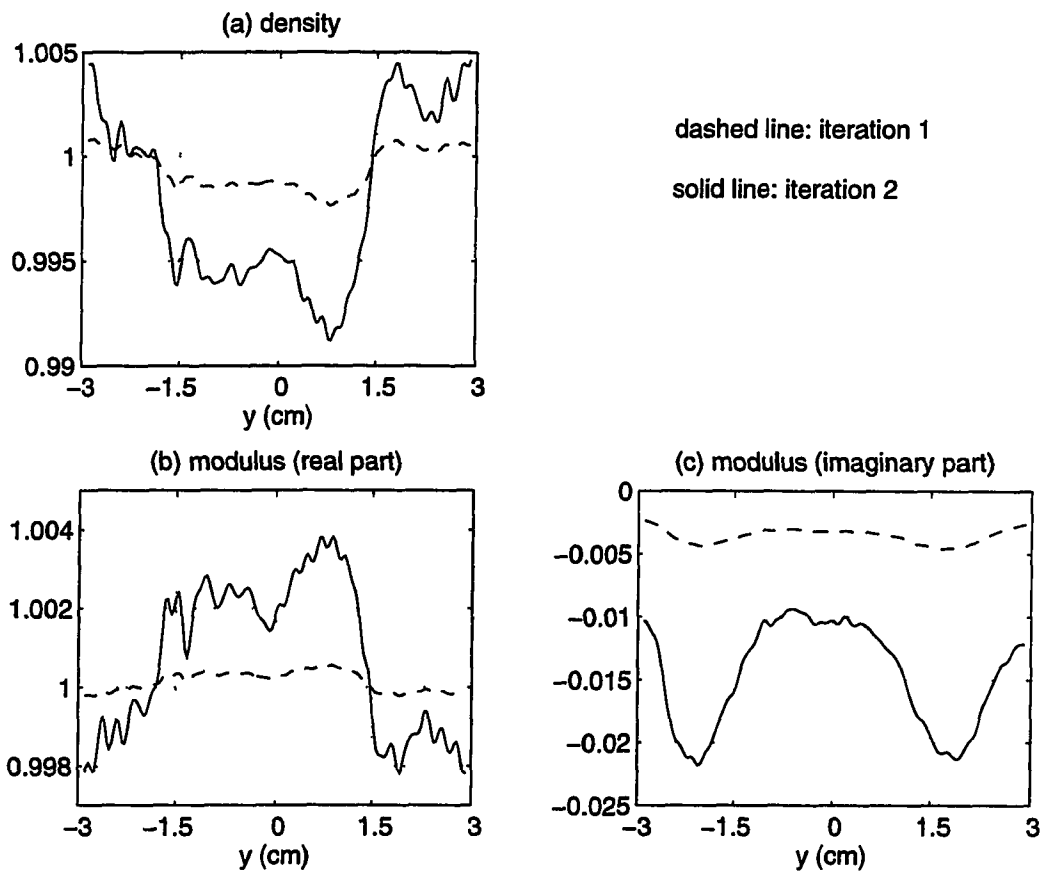


**Figure 6.19.** Plots of the  $x$ -axis cross section through the center for iteration 1 and 2. The frequency is 468.75 kHz and  $\lambda_0 = 3.2$  mm. The reconstruction area is  $18.14\lambda_0 \times 18.14\lambda_0$  and divided into  $181 \times 181$  cells.  $256 \times 205$  transmitter/receiver paired data are used.

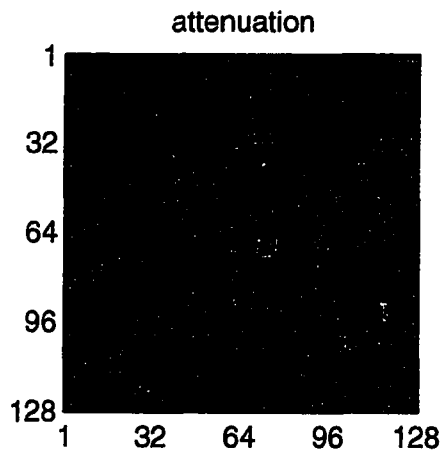
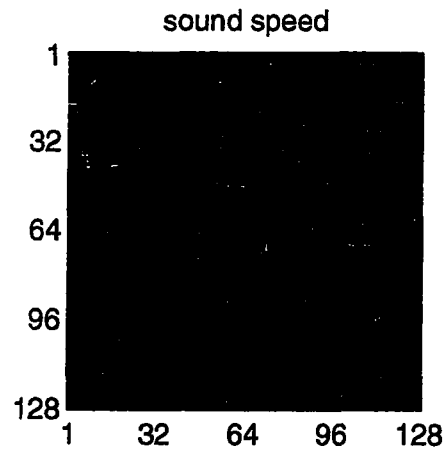


**Figure 6.20.** The egg images for the sound speed and attenuation provided by ThermoTrex Corp. Images are reconstructed by the diffraction tomography method at 343.75 kHz.

## 6.6 Conclusions

We have developed LSF with CGFFT algorithm to efficiently reconstruct the density and compressibility of soft tissues. The capability of the algorithm has been demonstrated by real experiment data and synthetic data. The algorithm cost for each iteration can be  $O(N^{1.5} \log N)$ . A very large object can be reconstructed by this algorithm.

It is difficult to reconstruct parameters of different scattering mechanisms by the single-frequency method in a nonlinear problem, although the object features can still be identified. The multiple-frequency scheme can reconstruct both body density and compressibility with higher fidelity than the single-frequency scheme. One of the multiple-frequency schemes, the frequency-hopping method, is used to obtain better reconstructions in several discrete operating frequencies.

## 6.7 References

- [1] J. J. Wild and J. M. Reid, "Further pilot echographic studies on the histologic structure of tumors of the living intact human breast," *Am. J. Pathol.*, vol. 28, pp. 893, 1952.
- [2] R. C. Waag, "A review of tissue characterization from ultrasonic scattering," *IEEE Trans. Biomed. Eng.*, vol. 31, pp. 884-893, 1984.
- [3] K. J. W. Taylor, "Tissue characterization," *Ultras. Med. Biol.*, vol. 15, pp. 421-428, 1989.
- [4] R. K. Mueller, M. Kaveh, and G. Wade, "Reconstructive tomography and applications to ultrasonics," *Proc. IEEE*, vol. 67, pp. 567-587, 1979.
- [5] J. S. Ball, S. A. Johnson, and F. Stenger, "Perturbation methods for reconstructing 3-d complex acoustic velocity and impedance in circular geometries with spherical waves," *Acoustical Imaging*, vol. 9, pp. 451-461, 1980.
- [6] M. Kaveh, M. Soumekh, and R. K. Mueller, "A comparison of Born and Rytov approximations in acoustic tomography," *Acoustical Imaging*, vol. 11, pp. 325-335, 1981.
- [7] A. J. Devaney, "Inverse-scattering theory within the Rytov approximation," *Optics Letters*, vol. 6, no. 8, pp. 374-376, 1981.

- [8] A. J. Devaney, "Inversion formula for inverse scattering within the Born approximation," *Optics Letters*, vol. 7, no. 3, pp. 111-112, 1982.
- [9] A. J. Devaney, "A filtered backpropagation algorithm for diffraction tomography," *Ultrasonic Imaging*, vol. 4, pp. 336-360, 1982.
- [10] A. J. Devaney, "Variable density acoustic tomography," *J. Acoust. Soc. Am.*, vol. 78, no. 1, pp. 120-130, 1985.
- [11] A. Özbek and C. L. Benard, "Simultaneous linearized inversion of velocity and density profiles for multidimensional acoustic data," *J. Acoust. Soc. Am.*, vol. 89, no. 4, pt. 1, pp. 1737-1748, 1991.
- [12] M. Moghaddam and W. C. Chew, "Variable density linear acoustic inverse problem," *Ultrasonic Imaging*, vol. 15, pp. 255-266, 1993.
- [13] M. F. Insana and D. G. Brown, "Acoustic scattering theory applied to soft biological tissues," *Ultrasonic Scattering in Biological Tissues*, Eds. K. K. Shung and G. A. Thieme, Boca Raton, FL: CRC Press, 1993, Chapter 4, pp. 75-124.
- [14] S. A. Johnson, F. Stenger, C. Wilcox, J. Ball, and M. J. Berggren, "Wave equations and inverse solutions for soft tissue," *Acoustical Imaging*, vol. 11, pp. 409-424, 1982.
- [15] S. A. Johnson and M. L. Tracy, "Inverse scattering solutions by a sinc basis, multiple source, moment method - part i: theory," *Ultrasonic Imaging*, vol. 5, pp. 361-375, 1983.
- [16] M. L. Tracy and S. A. Johnson, "Inverse scattering solutions by a sinc basis, multiple source, moment method - part ii: numerical evaluation," *Ultrasonic Imaging*, vol. 5, pp. 376-392, 1983.
- [17] S. A. Johnson, Y. Zhou, M. L. Tracy, M. J. Berggren, and F. Stenger, "Inverse scattering solutions by a sinc basis, multiple source, moment method - part iii: fast algorithms," *Ultrasonic Imaging*, vol. 6, pp. 103-116, 1984.
- [18] D. T. Borup, S. A. Johnson, W. W. Kim, and M. J. Berggren, "Nonperturbative diffraction tomography via Gauss-Newton iteration applied to the scattering integral equation," *Ultrasonic Imaging*, vol. 14, pp. 69-85, 1992.
- [19] S.-Y. Kim, H.-C. Choi, J.-M. Lee, and J.-W. Ra, "Inverse scattering scheme based on the moment method in the spectral domain, part i: theory," *Ultrasonic Imaging*, vol. 14, pp. 16-28, 1992.
- [20] H.-C. Choi, S.-Y. Kim, and J.-W. Ra, "Inverse scattering scheme based on the moment method in the spectral domain, part ii: numerical simulation," *Ultrasonic Imaging*, vol. 14, pp. 29-39, 1992.

- [21] M. Moghaddam and W. C. Chew, "Simultaneous inversion of compressibility and density in the acoustic inverse problem," *Inverse Problems*, vol. 9, pp. 715-730, 1993.
- [22] G. P. Otto and W. C. Chew, "Inverse scattering of  $H_z$  waves using local shape function imaging: a T-matrix formulation," *Int. J. Imaging Sys. Tech.*, vol. 5, pp. 22-27, 1994.
- [23] P. M. Morse and K. U. Ingard, *Theoretical Acoustics*. New York: McGraw-Hill, 1968.
- [24] J. H. Richmond, "Scattering by a dielectric cylinder of arbitrary cross section shape," *IEEE Trans. Antennas Propag.*, vol. 13, no. 5, pp. 334-341, May 1965.
- [25] W. C. Chew, *Waves and Fields in Inhomogeneous Media*. New York: Van Nostrand Reinhold, 1990.
- [26] R. F. Harrington, *Time-Harmonic Electromagnetic Fields*. New York: McGraw-Hill, 1961.

## CHAPTER 7

### CONCLUSIONS AND FUTURE DIRECTIONS

In this dissertation, iterative methods are employed as the main solvers in forward scattering and inverse scattering problems for large penetrable bodies. FFT is used to expedite the matrix-vector multiply, which is the most computationally intensive part in iterative methods. An alternative to FFT is to use NEPAL, which can be an  $O(N)$  algorithm combined with FMM. Inverse electromagnetic scattering problems in two dimensions for TM polarization are investigated by DBIM; two-dimensional ultrasonic imaging is studied by the LSF method. Three-dimensional vector scattering problems formulated by T-matrix are solved with BiCGFFT.

CGFFT and BiCGFFT are  $O(N_i N \log_2 N)$  algorithms with  $O(N)$  required memory storage, where  $N_i$  is the number of iterations to converge. We observed that  $N_i$  is proportional to  $N$  for lossless media and to  $\sqrt{N}$  for lossy media (even better than  $\sqrt{N}$  for BiCGFFT). Both algorithms have to be restarted whenever the right-hand side changes. But the  $O(N^2)$  algorithm RATMA can be reused for different incident fields. Therefore, when solutions for many incident angles are required, RATMA is the better choice. If only a few incident fields are considered, CGFFT or BiCGFFT is more efficient when the convergence rate is better than  $O(N)$ . Also, when a good initial guess is available, CGFFT or BiCGFFT is more attractive.

DBIM combined with CGFFT has provided an efficient and more rigorous method for solving inverse scattering problems in 2D. Although DBIM extends the applicable range of the conventional diffraction tomography, it is not sufficient for the large body reconstruction when using only monochromatic data. Multiple-frequency or frequency-hopping schemes alleviate the difficulty. Using the frequency-hopping scheme, a  $10\lambda \times 10\lambda$  inhomogeneous area is reconstructed with high fidelity

in the real part of permittivity. Hybrid schemes should be adopted to retrieve different parameters accounting for different physical mechanisms. For example, microwave imaging can be incorporated with the electrical impedance tomography to reconstruct both permittivity and conductivity.

Large-size problems plague the iterative methods in a way that the condition number of the resultant matrix grows with the problem size and so does the number of iterations for convergence. The residual error would decrease very slowly and even stagnate due to finite numeric accuracy. Preconditioners are crucial for iterative methods and are yet to be investigated for general dense matrices. More physical insight to existing problems can help developing specific preconditioners by choosing suitable weighting or testing functions.

NEPAL is an algorithm to implement the matrix-vector multiply for dense matrices in  $O(N \log N)$  operations and can be adapted to the case of nonuniform grids. By incorporating with FMM, an  $O(N)$  algorithm can be achieved in the matrix-vector multiply when  $N$  is very large. NEPAL can also be extended to deal with three-dimensional problems.

Three-dimensional vector wave scattering problems are formulated by the T-matrix method, and the resultant matrix equation is solved efficiently by BiCG method coupled with FFT. The T-matrix formulation avoids the singularity problem incurred in the dyadic Green's function. The linear growth with  $N$  in memory requirement by BiCGFFT makes it possible to solve large 3D scattering problems. A 90,000-unknown volume scattering problem is solved on a 10 MFLOPS workstation within 2.5 hours. The internal field, as well as the scattered field, can be calculated by this algorithm. This algorithm can be applied directly to magnetic medium problems without any modification. The scattering by a cluster of randomly located discrete scatterers can also be solved efficiently by this method with an intermediate aggregation step.

The ultrasonic imaging of both density and compressibility (or modulus) for soft tissues is realized by the LSF method with CGFFT. This algorithm belongs to the nonlinear iterative methods, which account for the multiple scattering effect. Based on the T-matrix formulation, the LSF method reconstructs transition coefficients for each subscatterer, from which the density and compressibility can be derived. Simulation examples suggest that multiple-frequency data be used to obtain good reconstructions. To this end, the frequency-hopping scheme is employed. More improvement in images will be achieved if hybrid schemes are considered. Real data have been processed to yield images of a boiled egg, which show different compositions within. In practice, biological tissues are three-dimensionally structured and measurement systems are of finite sizes; therefore, extra assumptions about biological bodies and calibration process are required to utilize two-dimensional inverse scattering algorithms. Hence, 3D inverse scattering algorithms are necessary to produce better images in a more realistic sense. LSF with CGFFT can be extended to three-dimensional imaging in a straightforward manner. Another extension of the current algorithm is to consider the inverse elastic wave scattering for the characterization of flaws in structural materials.

## APPENDIX A

### SUMMARY OF COMPUTER CODES USED

The numerical results presented in this thesis were computed using custom software on a variety of computer platforms. A Sun Microsystems' SPARCclassic UNIX workstation running X-window was used as the host platform. The workstation was used for a variety of numerical calculations and all of the data visualization. Hewlett-Packard's HP 700-series workstations were also used in the production phase of algorithms. Mathworks' Matlab software and Island Graphics' IslandDraw were used extensively for data visualization and postprocessing.

The processing power of Cray Research's Y-MP and C90 supercomputers and the SGI Power Challenge Array parallel supercomputer were used for the CPU-intensive forward and inverse scattering computations.

#### A.1 2D TM CGFFT Forward Solver

The programs `cgfft.tm.f` and `bicgfft.tm.f` are the forward solvers for the 2D TM-polarization scalar wave equation. Note that `bicgfft.tm.f` is using the Bi-CG algorithm for the symmetric matrix.

Directory:	Programs/2DTM
Target Machine:	Sun workstations

Program Modules:

<code>cgfft.tm.f</code>	:	CGFFT program
<code>bicgfft.tm.f</code>	:	BiCGFFT program
<code>bess.f</code>	:	Subroutines of Bessel and Hankel functions

**Input Files:**

**para.dat** : ASCII data file for some parameters such as the frequency  
**object.dat** : ASCII data file for the permittivity and location of each cell  
**infl.d.dat** : ASCII data file for the incident field at each cell  
**rxl.dat** : ASCII data file for receiver locations

**Output Files:**

**scatt.dat** : ASCII data file for the scattered fields at the receivers

## **A.2 2D TM DBIM Inverse Scattering Algorithm**

The program **dist\_born\_ri.f** is a DBIM inverse scattering algorithm for the 2D TM-polarization scalar wave equation. Either the synthetic or measurement data may be used.

**Directory:** Programs/Inverse\_TM

**Target Machine:** Sun workstations

**Program Modules:**

**dist\_born\_ri.f** : DBIM program  
**bess.f** : Subroutines of Bessel and Hankel functions

**Input Files:**

**para\_inv.dat** : ASCII data file for some parameters such as the frequency  
**measure.dat** : Synthetic data or real measurement data  
**covmx.dat** : ASCII data file for the regularization parameter  
**trlx.dat** : ASCII data file for the transmitter and receiver locations  
**mrt.dat** : ASCII data file for flagging which transmitter-receiver pair is active  
**ini\_gues.dat** : ASCII data file for the initial guess of permittivity

**Output Files:**

**discrepancy.dat** : Relative residual error (RRE) at each iteration  
**nxt\_gues.dat** : Reconstructed permittivity profile that can be used as the initial guess of the next higher frequency in the frequency-hopping scheme  
**obip.dat** : Reconstructed permittivity profile

The following programs are suitable for Cray supercomputers, from which special 2D FFT routines are used. The other subroutines, and input and output files used by **c\_dist\_born\_ri.f** remain the same as those for Sun workstations. **c\_multi\_cgfft\_tm.f** is the forward solver for multiple views.

**Directory:** Programs/Inverse-TM/Cray

**Target Machine:** Cray Y-MP or C90

**Program Modules:**

**c\_dist\_born\_ri.f** : DBIM program  
**c\_multi\_cgfft\_tm.f** : CGFFT program for multiple views  
**obj.dim.f** : File to be included in **c\_multi\_cgfft\_tm.f** to declare the dimension of object arrays  
**fft.dim.f** : File to be included in **c\_multi\_cgfft\_tm.f** to declare the dimension of FFT arrays

**Input Files:**

**para.dat** : ASCII data file for some parameters such as the frequency  
**object.dat** : ASCII data file for the permittivity and location of each cell  
**rxl.dat** : ASCII data file for receiver locations  
**txl.dat** : ASCII data file for transmitter locations

**Output Files:**

**measure.dat** : ASCII data file for scattered fields calculated by **c\_multi\_cgfft\_tm.f**

### A.3 NEPAL

The program `drive.f` serves as a driving program for the NEPAL subroutines, which are included in `nep.f`. Given sources in `source.dat` in some region, the fields over the same area will be calculated and stored in `field.dat`.

Directory:            **Programs/NEPAL**  
Target Machine:      **Sun workstations**

**Program Modules:**

`drive.f`            :   Driving program  
`nep.f`             :   Contains NEPAL subroutines  
`bess.f`            :   Subroutines of Bessel and Hankel functions

**Input Files:**

`para.dat`         :   ASCII data file for some parameters such as the  
                          frequency  
`source.dat`       :   ASCII data file for source amplitudes

**Output Files:**

`field.dat`        :   ASCII data file for fields due to the sources in the  
                          same region

### A.4 3D BiCGFFT T-Matrix Algorithm

The program `bicgfft_3d_dp.f` is the forward solver for the 3D electromagnetic wave equation and is suitable for calculating the bi-static RCS and the internal field within the dielectric object. The incident field amplitudes at each cell must be first calculated by `plane_dp.f`. Note that the programs are in double precision.

Directory:            **Programs/3DEM**  
Target Machine:      **Sun workstations**

**Program Modules:**

**bicgfft\_3d\_dp.f** : BiCGFFT program with the T-matrix formulation  
**sphere\_lib\_dp.f** : Subroutine set for calculating spherical functions  
**obj.dim.f** : File to be included in **bicgfft\_3d\_dp.f** to declare the dimension of object arrays  
**fft.dim.f** : File to be included in **bicgfft\_3d\_dp.f** to declare the dimension of FFT arrays  
**plane\_dp.f** : Program to calculate the incident field amplitudes

**Input Files:**

**para.dat** : ASCII data file for some parameters such as the frequency  
**object.dat** : ASCII data file for the permittivity and location of each cell  
**indx\_inf.dat** : ASCII data file for the cell serial number as required in calculating the internal field  
**rxl.dat** : ASCII data file for the receiver locations  
**plane\_dp.inp** : ASCII data file used by **plane\_dp.f** for parameters such as the incident angle and polarization, and the number of harmonics to expand the plane wave  
**infld.dat** : ASCII data file for the incident field amplitudes generated by **plane\_dp.f**

**Output Files:**

**scatt.dat** : Scattered fields at the receivers  
**inter fld.dat** : Internal fields at cells specified in **indx\_inf.dat**

The following programs for the Cray supercomputer are suitable for calculating monostatic RCS and the internal field. All the input and output files used by **bicgfft\_3d.f** remain the same as those for Sun workstations except that **plane\_dp.inp** and **infld.dat** are no longer needed.

**Directory:** Programs/3DEM/Cray  
**Target Machine:** Cray Y-MP or C90

**Program Modules:**

**bicgfft\_3d.f** : BiCGFFT program with the T-matrix formulation  
**sphere\_lib.f** : Subroutine set for calculating spherical functions

### **A.5 Local Shape Function with CGFFT Algorithm**

The program **inv.f** is the inverse scattering algorithm for the ultrasonic wave equation using the Local Shape Function method with CGFFT. Both density and compressibility of soft tissues are parameters to reconstruct from measurement data. The program **multi\_cgfft\_sv.f** is a forward solver for multiple views.

**Directory:** Programs/Acoustics  
**Target Machine:** Sun workstations

**Program Modules:**

**inv.f** : Program of LSF with CGFFT  
**bess.f** : Subroutines of Bessel and Hankel functions  
**obj.dim.f** : File to be included in **inv.f** to declare the dimension of object arrays  
**obj2.dim.f** : Same as above  
**fft.dim.f** : File to be included in **inv.f** to declare the dimension of FFT arrays  
**trx.dim.f** : File to be included in **inv.f** to declare the dimension of transmitter and receiver arrays  
**trx2.dim.f** : Same as above  
**jmod.dim.f** : File to be included in **inv.f** to declare the dimension of expansion harmonics array  
**multi\_cgfft\_sv.f** : CGFFT program for multiple views using the T-matrix formulation in the ultrasonic wave scattering. The output binary data file is **whole.dat**  
**gen\_meas\_mrt.f** : Program to postprocess the scattered field data in **whole.dat** to yield **measure.dat**, **trlx.dat**, and **mrt.dat**

**Input Files:**

**para\_inv.dat** : ASCII data file for some parameters such as the frequency  
**measure.dat** : Binary data file for scattered fields generated by **gen\_meas\_mrt.f**  
**covmx.dat** : ASCII data file for the regularization parameter  
**trlx.dat** : ASCII data file for the transmitter and receiver locations  
**mrt.dat** : ASCII data file for flagging which transmitter-receiver pair is active  
**ini\_gues1.dat** : Binary data file for the initial guess of the object density  
**ini\_gues2.dat** : Binary data file for the initial guess of the object compressibility

\*\*\*\*\* The following input files are used by **multi\_cgfft\_sv.f** \*\*\*\*\*

**para.dat** : ASCII data file for some parameters such as the frequency  
**object1.dat** : ASCII data file for the density and location of each cell  
**object2.dat** : ASCII data file for the compressibility and location of each cell  
**rxl.dat** : ASCII data file for receiver locations  
**txl.dat** : ASCII data file for transmitter locations

**Output Files:**

**discrepancy.dat** : Relative residual error (RRE) at each iteration  
**nxt\_gues1.dat** : Reconstructed density profile that can be used as the initial guess of the next higher frequency in the frequency-hopping scheme  
**nxt\_gues2.dat** : Reconstructed compressibility profile that can be used as the initial guess of the next higher frequency in the frequency-hopping scheme  
**obip1.dat** : Reconstructed density profile  
**obip2.dat** : Reconstructed density profile

The following programs are for the Power Challenge supercomputer, where special 2D FFT routines are used. To date, the full capability of parallel processing in the Power Challenge supercomputer has not yet been exploited. The other subroutines, and input and output files used by `pc_inv.f` and `pc_mul_cgfft_sv.f` remain the same as those for Sun workstations.

Directory:            `Programs/Acoustics/Power`  
Target Machine:      `Power Challenge`

Program Modules:

`pc_inv.f`            : Program of LSF with CGFFT  
`pc_mul_cgfft_sv.f` : CGFFT program for multiple views using the T-matrix formulation in the ultrasonic wave scattering. The output binary data file is `whole.dat`

## VITA

Jiun-Hwa Lin was born in Taipei, Taiwan, Republic of China, on March 16, 1962. From September 1981 to June 1985, he attended National Taiwan University (NTU) and received the Bachelor of Science degree in Electrical Engineering.

From July 1985 to May 1987, he served in the Combined Service Force in Tainan, Taiwan, R.O.C., and assisted in designing the power line layout for factories and buildings.

In September 1987, Mr. Lin began his graduate studies at NTU. During his studies, he participated in processing and analyzing the echoed data of VHF MST (mesosphere, stratosphere and troposphere) radar and, under the guidance of Professor Yean-Woei Kiang, he obtained the Master of Science in Electrical Engineering with a thesis entitled "A Simulation Study Of Ionospheric Spread F Phenomenon."

In September 1989, Mr. Lin enrolled at the University of Michigan in Ann Arbor and worked for Professor Yasuo Kuga (now with the Electrical Engineering Department of University of Washington). However, Mr. Lin later decided to pursue his Ph.D. degree at another university because of his interest in computational electromagnetics.

Since June 1990, Mr. Lin has been working for Professor Weng Cho Chew as a research assistant in the Department of Electrical and Computer Engineering, University of Illinois at Urbana-Champaign (UIUC). While at UIUC, he participated in several research projects, including numerical algorithms for scattering problems. From January 1993 to May 1995, Mr. Lin was also a teaching assistant responsible for tutoring students and grading homework for undergraduate electromagnetics courses.

His current research interests are in wave propagation, forward and inverse scattering, preconditioning, antenna design and high-speed circuit modeling.

A list of Mr. Lin's technical publications is given below.

### Journal Papers

1. J.-H. Lin and W. C. Chew, "Scattering solution of oblong, dielectric-coated, metallic scatterers by the recursive algorithm," *Electronics Letters*, vol. 28, no. 2, pp. 185-186, January 1992.
2. W. H. Weedon, W. C. Chew, J.-H. Lin, A. Sezginer and V. L. Druskin, "A 2.5-D scalar Helmholtz wave solution employing the spectral Lanczos decomposition method (SLDM)," *Microwave and Optical Technology Letters*, vol. 6, no. 10, pp. 587-592, August, 1993.
3. J.-H. Lin and W. C. Chew, "BiCG-FFT T-matrix for solving for the scattering solution from inhomogeneous bodies," submitted to *IEEE Trans. Microw. Theory Tech.* for publication.
4. W. C. Chew and J.-H. Lin, "Frequency hopping scheme in inverse scattering," submitted to *IEEE Microw. Guided Wave Lett.* for publication.
5. W. C. Chew, J.-H. Lin and X. G. Yang, "An FFT T-matrix method for 3D electromagnetic scattering solutions from random discrete scatterers," *Microwave and Optical Technology Letters*, vol. 9, no. 4, pp. 194-196, July 1995.
6. W. C. Chew, G. P. Otto, W. H. Weedon, J.-H. Lin, C. C. Lu, Y. M. Wang and M. Moghaddam, "Nonlinear diffraction tomography—the use of inverse scattering for imaging," *Int. J. Imaging Sys. Technol.*, submitted for publication.

### Conference Papers

1. W. C. Chew, Y. M. Wang, L. Gurel and J.-H. Lin, "Recursive algorithms to reduce the computational complexity of scattering problems," *Conference Proceedings, 7th Annual Review of Progress in Applied Computational Electromagnetics*, Naval Postgraduate School, Monterey, CA, pp. 278-291, March 18-22, 1991.
2. W. C. Chew, Y. M. Wang, L. Gurel, J.-H. Lin and Q. H. Liu, "Fast algorithms for calculating scattering by inhomogeneous and impenetrable objects," *PIERS 1991 Proceedings*, Cambridge, MA, pp. 699, July 1-5, 1991

3. J.-H. Lin and W. C. Chew, "Solving large scattering problem on a PC using the recursive aggregate T-matrix algorithm," *IEEE Antennas and Propagation Society International Symposium Digest*, Chicago, IL, pp. 1513-1516, July 18-25, 1992.
4. J.-H. Lin and W. C. Chew, "A comparison of the CG-FFT method and the recursive aggregate T-matrix algorithm," *IEEE Antennas and Propagation Society International Symposium Digest*, Chicago, IL, pp. 1591-1594, July 18-25, 1992.
5. W. C. Chew, J.-H. Lin, C. C. Lu, Y. M. Wang, J. J. Mallorqui, A. Broquetas, Ch. Pichot, and J.-Ch. Bolomey, "Processing microwave experiment data with the distorted Born iterative method of nonlinear inverse scattering," *IEEE Antennas and Propagation Society International Symposium Digest*, University of Michigan, Ann Arbor, MI, pp. 500-503, June 28 - July 2, 1993.
6. J.-H. Lin and W. C. Chew, "An application of nested equivalence principle algorithm (NEPAL) in matrix-vector multiplication of iterative algorithms," *URSI Radio Science Meeting Program and Abstracts*, University of Michigan, Ann Arbor, MI, pp. 317, June 28 - July 2, 1993.
7. W. C. Chew, C. C. Lu and J.-H. Lin, "NEPAL—A fast algorithm for solving volume integral equation," *PIERS 1993 Proceedings*, pp. 518, Jet Propulsion Laboratory, California Institute of Technology, Pasadena, CA, July 1993.
8. W. C. Chew, J.-H. Lin and X. G. Yang, "An FFT T-matrix method for scattering solutions from inhomogeneous bodies and random discrete scatterers," *IEEE Antennas and Propagation Society International Symposium Digest*, Newport Beach, CA, pp. 386-389, June 18-23, 1995.
9. W. C. Chew and J.-H. Lin, "A frequency-hopping approach for microwave imaging of large inhomogeneous bodies," *IEEE Antennas and Propagation Society International Symposium Digest*, Newport Beach, CA, pp. 1610-1613, June 18-23, 1995.
10. J.-H. Lin and W. C. Chew, "Using electromagnetic inverse algorithms for ultrasonic imaging," *PIERS 1995 Proceedings*, pp. 618, Seattle, WA, July 24-28, 1995.